Majorana Fermions in Superconducting Quantum Wires

Kevin Jägering

Master's Thesis
Theoretical and Mathematical Physics

Chair of Theoretical Solid State Physics
Faculty of Physics
Ludwig-Maximilians-University Munich

Supervisor: Prof. Jan von Delft

November 2014

Majorana Fermions in Superconducting Quantum Wires

Kevin Jägering

Master's Thesis
Theoretical and Mathematical Physics

Chair of Theoretical Solid State Physics
Faculty of Physics
Ludwig-Maximilians-University Munich

Supervisor: Prof. Jan von Delft

November 19, 2014

Contents

Chapter 0

Abstract

The appearance of Majorana fermions in one dimensional p-wave superconductors was first predicted by A. Kitaev in his well known paper [Kitaev, 2000]. One expected signature of such zero-energy states is a zero-bias peak (ZBP) in the differential conductance. Recent experiments ([Mourik et al., 2012] and [Das et al., 2012]) claim to have found this ZBP, but they had to add a quantum point contact (QPC) to the system and use a fine tuned method of emulating the p-wave behavior in their experimental wires with strong spin-orbit interactions, external magnetic field and proximity induced s-wave superconductivity. This raises the question whether the ZBP from the experiments, which had to include explicit geometry in form of the QPC, corresponds to the prediction from the Kitaev model, which does not include any geometry. The ansatz of this work is to explicitly include the non-trivial geometry of the quantum point contact into the Kitaev model. To this end the Keldysh formalism in a one dimensional tight binding model is employed. We are then able to qualitatively reproduce a ZBP as seen in the experiments, but observe a strong dependence on the geometrical details of the QPC which we do not understand. We need to fine tune the shape of the QPC with the width and height of the superconducting gap to achieve the ZBP in our model.

Chapter 1

Introduction

This thesis is divided into two major parts. In the first part, a basic spinless model for a quantum wire and then a quantum point contact in second quantization formulation will be introduced and then expanded to include spins and magnetic field effects.

To this end we start in chapter 2 with a basic definition of a quantum wire. Since we are interested in the low energy physics, we start with the approximation of a continuous one-dimensional electron gas useful for analytical descriptions and then discretize to a lattice/chain formulation of second quantized electrons hopping on effective lattice sites consisting of many ions, which is necessary for computer calculations. We will see how we can write the Hamiltonian that describes the system as a matrix to calculate the Green's function and local density of state and then add a potential barrier that shifts the chemical potential to also include quantum point contacts into our model. Finally, we have to get from a finite piece of quantum wire to an infinite system to be able to describe conductance through the system. This can be achieved by adding infinite leads and then replacing them with a self-energy term.

So far we have considered a spinless wire. When adding the spin degree of freedom in chapter 3, the two important new effects coupled to the spin are the spin-orbit-interaction and Zeeman splitting from external magnetic fields. Although we will not directly include these effects in most of our calculations, their qualitative effect will turn out to be very important to understand the physics that appears in later chapters. Hence we will observe the change in LDoS and conductance to get an intuition for their effects. Spin-orbit terms are generally only taken into account in their lowest order, which we will confirm to be a good approximation in the last section, where higher order terms are added to the Hamiltonian and found to be insignificant for reasonable effect strength.

Then follows the second part of this thesis, in which the concept of Majorana Fermions is introduced. They were first predicted in 1937 by Ettore Majorana ([Majorana, 1937]) as fermions which are their own antiparticle. In a short historic introduction in chapter 4, we will see that after many decades they still survive as a concept for fundamental particles, even though no experimental verification of their existence has been found yet. Instead, we will see that they can be realized as quasi-particles in solid state physics, in particular in one-dimensional semiconductor wires ("Kitaev model"), making a connection to the first part of the thesis.

One of the major components of the Kitaev model is a p-wave superconducting term in the Hamiltonian. In chapter 5 we will expand our model from the first chapter to include this new term and make use of the Keldysh formalism of quantum field theory to deduce a formula for the Green's function and conductance of a Kitaev model.

We then apply our new formulas in chapter 6 to observe how we can manipulate the Majorana fermions in the Kitaev model. The Majorana bound states are located at domain walls between wire regions with a topological and normal superconducting phase - and this phase can be tuned surprisingly simply by applying external potentials to shift the chemical potential. It turns out that this easy way of manipulating and thereby exchanging Majorana fermions, together with their very uncommon property of being non-Abelian anyons, allows one to build a quantum computer based on the exchange of Majorana modes, called topological quantum computer. This makes Majorana fermions and their various realizations in solid state physics a currently very active research topic.

In the final chapter 7 we have a look at the experimental verification of these theoretically predicted quasi-particles. Although the existence of Majorana fermions is generally seen as not yet definitely proven, recent experimental results ([Mourik et al., 2012] and [Das et al., 2012]) claim to have found clear signatures of Majorana fermions in form of zero-bias peaks in differential conductance measurements. We can use our formulas to describe a similar setup of the Kitaev model and get a qualitatively agreeing zero-bias peak in the calculated differential conductance. But this comparisons has to be taken with caution, because the experiments can not directly implement a Kitaev model since there are no p-wave superconducting materials yet. Instead, a clever setup of a normal semi-conducting wire with high spin-orbit interaction, external magnetic field and proximity induced s-wave superconductivity can be tuned to behave similar to a p-wave superconductor and hence emulate the Kitaev model. We end with a final conclusion and outlook. While our calculations seem to confirm the experimental results being signatures of Majorana fermions, the logical next step is to include spin-orbit effects and external magnetic fields into the formulas we developed. Then one could try to directly describe the experimental setups instead of just the Kitaev model that the experiments are tuned to hopefully behave like.

Chapter 2

A Model for Quantum Wires and Quantum Point Contacts

A quantum wire is a system of electrons that are constricted to move in only one dimension. It is an approximation to a real wire that gets so thin, that the electron-wavefunctions in the other two space dimensions get quantized. The quantization is then assumed to be big enough, or the energy chosen carefully enough, that only the lowest of these energy levels gets excited, leaving the position and momentum in wire direction as the only free parameters of the electrons.

The aim of this chapter is to work out a simple model Hamiltonian to describe such a one dimensional wire. A physical wire will usually be made out of metal, i.e. crystalline solids which are described by lattices. In the language of solid state physics this can be formalized by using a tight-binding model approach in which we assume that the wave functions of the electrons in the metal are superpositions of strongly localized wave-functions of electrons at the atomic sites. But to describe every atom in a wire of an experimentally relevant size by its own site would make the calculations of relevant quantities introduced in section 2.2 impossible to perform since the required matrix sizes would be beyond technical limitations.

Since we are ultimately interested in the low energy physics of the wire, which is dominated by the shape of the lower band edge, we can use the approximation of a free one-dimensional electron gas. This works well, since after choosing the correct effective mass, the relevant lower edge of the quadratic dispersion relation can be brought into the same shape as the lower edge of the periodic dispersion relation of the lattice. In section 2.1 we begin at this point and see how to discretize the electron gas again, but this time with effective lattice sites that are much bigger than the corresponding physical atoms in the wire to end up with a model suitable for computer calculations. We can then introduce 2nd quantization operators c_i and $c_i^\dagger$ describing the creation or annihilation of electrons at one such effective site labeled i and from that point on use this 2nd quantized tight binding approach as the language for all the Hamiltonians that will appear in this thesis. For simplicity, the lattice size will in the following be normalized to $a = 1$.

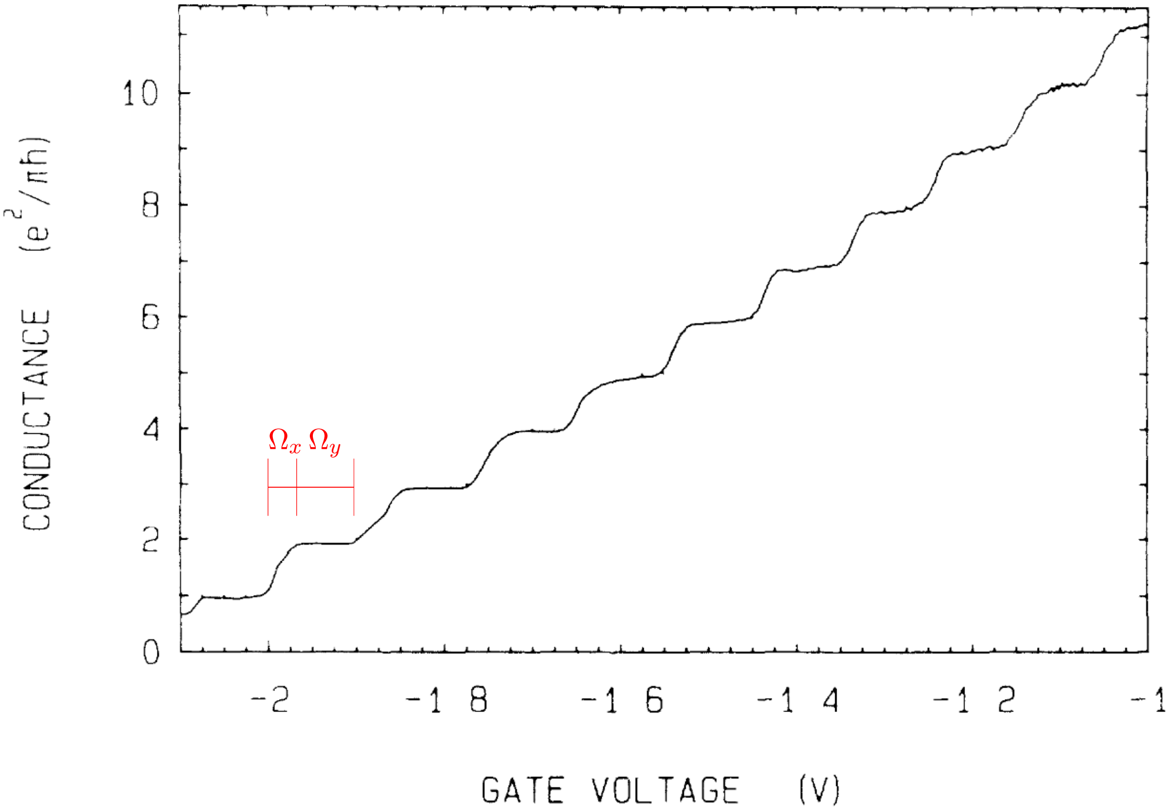

Figure 2.1: The measured conductance curve ([van Wees et al., 1988]) of a QPC in a two dimensional electron gas. The red marks Ω_x and Ω_y are added to show how information about the shape of the constricting potential barrier of the QPC can be extracted from the diagram as explained in the text.

At this point it is easy to get from a quantum wire to a quantum point contact. In general, a quantum point contact is a metallic contact that is small enough to again have quantization of electron-wavefunctions in two of the three space dimensions and a potential barrier that the electrons have to cross in the remaining one. It can be realized either with a gate in a two dimensional electron gas or by taking a real thin wire and adding a potential barrier to it.

Often one is interested in the conductance behavior of such contacts, as this both gives a lot of information about the structure and behavior of the system and is also one of the easiest to measure quantities experimentally. As the chemical potential is increased or equivalently the constriction is decreased, additional energy levels called modes become available for transport through the constriction. The major feature of quantum point contacts is the fact that each such conductance mode contributes a quantized amount of conductance of the size of the so called conductance quantum $\frac{2e^2}{h}$. This gives the conductance curve a characteristic and well known staircase shape (figure 2.1), with each step increasing the conductance by one quanta as a new mode becomes available. Let us see from the example of the conductance ladder how much information conductance contains. The width of the step, called Ω_x in figure 2.1, corresponds to the curvature of the potential barrier in conductance direction, as we will also see in figure 2.7 in section 2.5. The distance of the steps (Ω_y) corresponds to the energy distance of the different modes that result from the quantization in the direction that is orthogonal to the conductance direction, but still lies inside the 2D electron gas for the non-wire case. Measuring Ω_y for the different steps therefore also gives information about the shape of the constricting potential in this direction, together showing us the potential shape inside the device just from the conductance measurement alone.

Nevertheless, we will limit ourselves to wires and quantum point contacts consisting of only a single conductance band in this thesis, so only a single step of the ladder can be realized.

Adjusting our model to allow for a quantum point contact simple means allowing for an additional potential barrier in the wire, which in turn can just be seen as a modulation of the chemical potential. So we just need to add a site dependent term to the so far constant chemical potential and choose a shape for the potential (section 2.3).

Up to this point our description of discrete wires will be limited to finite wires. To get back to an infinite model, which is in particular necessary to make sense of conductance through the wire (section 2.5), we can add two semi-infinite leads to the system to make the wire infinite - and then integrate them out again (section 2.4) to get back to an (now effective) finite model so that we have finite matrices to calculate with.

2.1 Getting to a Discrete Model of a Quantum Wire

We begin by considering a one dimensional homogeneous electron gas in a quantum field theory (see for example [Negele and Orland, 1988], [Altland and Simons, 2010]). In the scope of this thesis the considered systems will always remain non-interacting with independent electrons, which is a major but necessary limitation, since dealing with interactions requires additional methods (like functional renormalization group, [Bauer et al., 2013]) that would add their own significant challenges.

Note that contrary to the cited books, we will explicitly not work in momentum space, which is preferable for homogeneous systems, but instead stay in a real space formulation which allows us to include explicit spatial structure into our wires. This is necessary since we will be interested in wires with potential barriers (section 2.3) and later superconducting regions (chapter 5), both of which break translational symmetry.

The Hamiltonian of such a system is then finally given by

$$\mathbf{H} = \int_{-\infty}^{\infty} \mathrm{d}x \, \Psi^\dagger(x) \left[\frac{p^2}{2m} - \mu \right] \Psi(x) \tag{2.1}$$

with the first term for the kinetic energy of the electrons and the second one being the chemical potential μ of the wire. The field operators $\Psi^\dagger$ (Ψ) create (annihilate) an electron at point x in the one dimensional and for the moment infinite wire.

Our first aim is to get from the continuous back to a discrete model. We assume that a tight-binding approach is applicable in which the wave functions of the electrons are approximated as superpositions of localized wave-functions at equidistant sites along the wire. These sites do not correspond to the atomic positions along a crystalline lattice but can be seen as effective sites which are much bigger. In terms of the Hamiltonian this corresponds to the field operators $\Psi_j^\dagger$ (Ψ_j) now creating (annihilating) electrons at discrete sites j, which have a lattice distance a between them (mostly set to $a = 1$). This gives the new Hamiltonian

$$\mathbf{H} = \sum_{j=-\infty}^{\infty} \Psi_j^\dagger \left[\frac{p^2}{2m} - \mu \right] \Psi_j. \tag{2.2}$$

The quantum mechanical momentum operator p acts as $p = -i\hbar \frac{\mathrm{d}}{\mathrm{d}x}$ so p^2 corresponds to a second derivative. Now that the system is discrete, the second derivative operator also has to be discretized. There is no unique discretization, since taking further away sites into consideration makes the result more and more exact (see 'finite difference methods' in mathematics), but for our purposes it suffices to take the simplest symmetric form:

$$\sum_j \frac{\mathrm{d}^2}{\mathrm{d}x^2} \Psi_j = \sum_j \frac{\mathrm{d}}{\mathrm{d}x} \left[\frac{\Psi_{j+1} - \Psi_j}{a} \right] = \sum_j \frac{\Psi_{j+2} - 2\Psi_{j+1} + \Psi_j}{a^2} = \sum_j \frac{\Psi_{j+1} - 2\Psi_j + \Psi_{j-1}}{a^2}. \tag{2.3}$$

So equation (2.2) becomes

$$\begin{aligned} \mathbf{H} &= \sum_{j=-\infty}^{\infty} \left[\Psi_j^\dagger \frac{p^2}{2m} \Psi_j - \mu \Psi_j^\dagger \Psi_j \right] = \sum_{j=-\infty}^{\infty} \left[-\Psi_j^\dagger \underbrace{\frac{\hbar^2}{2ma^2}}_{=:t} \frac{\Psi_{j+1} - 2\Psi_j + \Psi_{j-1}}{1} - \mu \Psi_j^\dagger \Psi_j \right] \\ &= \sum_{j=-\infty}^{\infty} \left[(2t - \mu) \Psi_j^\dagger \Psi_j - t (\Psi_j^\dagger \Psi_{j+1} + \Psi_{j+1}^\dagger \Psi_j) \right] \end{aligned} \tag{2.4}$$

and we have the desired discrete model of a wire. The last terms annihilate an electron and create a new one at a neighboring site, so they effectively allow movement (or 'hopping') of electrons along the wire. Hence these terms are called the hopping terms with a corresponding hopping amplitude t. Since t gives a natural energy scale for the wire, we will normalize it to $t = 1$ for most of the rest of this thesis and express other energies in terms of multiples of t. The $2t$ summand in the first term is often neglected as it is just a constant shift of the chemical potential.

For ease of notation the field operators $\Psi^\dagger$, Ψ can in the following be replaced by 2nd quantization creation and annihilation operators $c^\dagger$, c and hence the Hamiltonian to remember for future chapters is given by

$$\mathbf{H} = -t \sum_{j=-\infty}^{\infty} (c_j^\dagger c_{j+1} + \text{h.c.}) - \mu \sum_{j=-\infty}^{\infty} c_j^\dagger c_j \tag{2.5}$$

where the $2t$ has been absorbed into the μ.

Before we continue, let us quickly review how the discretization changes the dispersion relation of the system. This will be relevant in the following chapter 3 about spin-orbit-interaction and is a good exercise to get used to this model. Beginning with the time dependent Schrödinger equation $E_k\Phi_n = H\Phi_n = (p^2/2m - \mu)\Phi_n$ and with an ansatz of $\Phi_n = e^{ik(na)}$ for the wave function at a site n (and hence at position na) we get

$$E_k\Phi_n = -t(\Phi_{n+1} - 2\Phi_n + \Phi_{n-1}) - \mu\Phi_n = -t\left(-2\Phi_n + e^{ika}\Phi_n + e^{-ika}\Phi_n\right) - \mu\Phi_n. \tag{2.6}$$

Dividing by Φ_n we get the expected result

$$E_k = (2t - \mu) - t(e^{ika} + e^{-ika}) = (2t - \mu) - 2t\cos(ka). \tag{2.7}$$

Instead of the $\propto k^2$ dispersion relation of the free electron gas, we have a band of allowed energies of width $2t$ and periodic in k as it is typical for crystalline solids. But of course we have an effective lattice with sites consisting of many ions. To make the relevant lower band edge agree, a fitting effective mass for the electrons has to be chosen. Of course the constant term in the energy just corresponds to a shift of the zero-point, so it does not matter.

At the moment the wire we are considering is infinite. In the next chapter we will temporarily work with a finite wire to naturally introduce a matrix form of the Hamiltonian. That is just a detour allowing us to separately introduce the lead-eigenenergy in the end which leads us back to a description of an infinite wire in the matrix form. It would of course also be possible to do this in one step and directly integrate out all the lead degrees of freedom.

2.2 Deriving the Green's Function and Local Density of State

Now that we have a Hamiltonian for a simple wire from the last chapter, in this section we will look at how properties of the system can be extracted from it. The first step is to write the Hamiltonian as a matrix, as we expect the systems to get too complex for easy analytical results soon and are dependent on a numerical way of calculation. From there, the Green's function of the system becomes accessible by essentially inverting our Hamiltonian matrix. There is then a simple formula for the local density of states of the system and in section 2.5 we will see how transport properties in form of the conductance are also accessible through the Green's function. In later chapters we will then reuse and refine these methods to deal with more complicated cases where potential barriers, spin-orbit-interaction, magnetic fields and superconductivity are included.

We want to write the Hamiltonian (2.5) as a matrix in which each row or column correspond to one lattice site. Until now we have considered an infinite wire, which makes that clearly not possible. So at first it seems as if there is no choice but to confine ourselves to finite systems from now on. Luckily, the systems we are interested in have their important features (QPC or regions that become superconducting) in a relatively small area that we will term central region from now on, while we expect nothing exciting to happen in the two infinite remaining parts of the wire that will be named leads. As it turns out, it is enough to only describe the interesting central region explicitly in the Hamiltonian matrix and deal with the infinite but boring leads with a method discussed in section 2.4. Basically, we can add the leads to the system but then 'integrate' them out again, gaining a self-energy term which catches the full effect of the leads on the system without increasing the dimension of the matrix. As a result, we are able to fully describe an infinite wire with a finite matrix.

We reduce the sum in (2.5) to the central region by only allowing sites between $j = 1$ and $j = N$ and can then write

$$\mathbf{H} = -t \sum_{j=1}^{N-1} (c_j^\dagger c_{j+1} + \text{h.c.}) - \mu \sum_{j=1}^{N} c_j^\dagger c_j \tag{2.8}$$

into a matrix by defining a vector $\Psi^\dagger = (c_1^\dagger, c_2^\dagger, ..., c_N^\dagger)$. We can now find a matrix that, when inserted between Ψ vectors, reproduces the Hamiltonian above:

$$\mathbf{H} = \Psi^\dagger H \Psi = \Psi^\dagger \begin{pmatrix} -\mu & -t & 0 & & & & \\ -t & -\mu & -t & & & & \\ 0 & -t & -\mu & & & & \\ & & & \ddots & & & \\ & & & & -\mu & -t & 0 \\ & & & & -t & -\mu & -t \\ & & & & 0 & -t & -\mu \end{pmatrix} \Psi. \tag{2.9}$$

This H is our Hamiltonian matrix.

As a first little remark, we have access to the eigenenergies of the system by simply diagonalizing the matrix (2.9). For the simple system we consider right now this of course just produces a number of discrete energies that follow the dispersion relation (2.7) with energies varying over an interval of $4t$ and a global shift given by the chemical potential μ. By looking at the coefficients of the corresponding eigenvectors, we can see how much amplitude, or probability density after squaring it, of the wavefunctions of the states are concentrated at which sites. Later, when the leads are added and integrated out again, this has to be used with caution, since the eigenenergies and eigenvectors can not know about the leads and only show the results for an isolated central region.

To visualize the band structure and its changes under adding different features to the system and adjusting their parameters, we will next have a look at the local density of states (LDoS), which up to a 2π factor corresponds to the diagonal entries of the spectral function (see (2.12)) when the lattice distance is set to one. The general formula to get from a Hamiltonian $\bar{H}$ to the (retarded) Green's function is given by [Datta, 1995, chapter 3]

$$G^R(\omega) = \frac{1}{\omega - \bar{H} + i0} \tag{2.10}$$

with a positive infinitesimal term $i0$ making sure that the retarded Green's function is analytic in the upper complex plane as it should be.

For the operator H being the Hamiltonian matrix (2.9) this formula is still valid and can be understood as

$$G^R(\omega) = (\omega\mathbb{1} - H + i0\mathbb{1})^{-1} \tag{2.11}$$

where $\mathbb{1}$ is the unit matrix. The Green's function G^R is now itself a matrix in the same basis as H and could be returned to its full form as a sum over creation/annihilation operators at all sites by taking $\Psi^\dagger G \Psi$ with $\Psi^\dagger = (a_1^\dagger, a_2^\dagger, ..., a_N^\dagger)$. The entries of the Green's function tell us about the correlations of different parts of the system at an energy ω, hence they carry transport information that we will access later and information about the spatial structure of the energy states that can be extracted and visualized as follows.

As the name suggests, the local density of states (LDoS) $\rho_j(\omega)$ gives us the added up contribution of all the states of the system at a certain energy and site. Adding up its values for all the central sites will then naturally lead back to the normal density of states. Since the LDoS corresponds to the diagonal elements of the spectral function A, we can also get the density of states by taking the trace of the spectral function. To calculate $\rho_j(\omega)$, we have to evaluate the imaginary part of the diagonal elements of the Green's function as can be seen in the following way ([Datta, 1995, p.155], [Rickayzen, 1980, p.34])

$$\rho_j(\omega) = \frac{1}{2\pi} A_{jj}(\omega) \overset{A=i[G^R-G^A]}{=} \frac{i}{2\pi}\left[G^R_{jj}(\omega) - (G^R_{jj})^*(\omega)\right] = -\frac{1}{\pi}\mathrm{Im}\left(G^R_{jj}(\omega)\right). \tag{2.12}$$

For a finite dimensional system at zero temperature the LDoS/spectral function will be a series of δ-peaks located at the eigenenergies of the system in its dependence on ω ([Rickayzen, 1980, p.35]). When we try to access the LDoS in this case numerically with formula 2.12, we will generally miss most of its features since the spectral function is zero unless the argument ω exactly hits the energy of one of the δ-peaks. To see how to avoid this problem, note that in the case of a finite system that gets weakly coupled to the environment, the spectral function still shows peaks in its ω dependence, but those are not necessarily δ-peaks. Instead, these peaks have a finite width of 2Σ at the half-maximum-value, where Σ is the lifetime of the corresponding eigenstate of the system with the energy at which the peak is located ([Rickayzen, 1980, p.38]). In a finite system with temperature $T = 0$ the states can not decay, so their lifetime is infinite and hence the peaks must be δ-peaks.

In later sections we will attach leads to the system, making it infinite, so that the lifetime of states which have a chance to escape into the leads becomes finite. This gives the density peaks a finite width that makes them visible on plots of the LDoS using (2.12) numerically. In the formula, this corresponds to the leads adding a finite imaginary term to (2.11) besides the infinitesimal $+i0$, which can only produce the δ-peaks in the imaginary part of the Green's function.

Even after we add leads, this problem will only be solved for peaks that correspond to states which are allowed to escape from the central region into the leads. Not only might we be interested in the LDoS even in the case when no leads are attached to the system, but in 6.2 we will also encounter interesting localized states in the central region that do not get a finite lifetime even with leads attached and want to be able to see those in the LDoS as well. The solution is to replace the infinitesimal $+i0\mathbb{1}$ with a small but finite $+i\epsilon\mathbb{1}$ when calculating the Green's function with (2.11).

This gives all the states in the system an artificial finite lifetime, which corresponds to a finite peak width, making them visible in LDoS plots. This is demonstrated in figure 2.2, which shows the LDoS of our simple wire as colors, plotted over the effective site in the wire on the x-axis and the energy on the y-axis with different ϵ values between $\epsilon = \frac{2}{N}$ (left plot) and $\epsilon = \frac{20}{N}$ (right plot) where N is the total number of sites in the central region. It can be seen that a good middle ground for the choice of ϵ must be found. For small $\epsilon = \frac{2}{N}$ there are still artifacts visible in x-direction (the horizontal bright/dark lines in the left plot of figure 2.2) coming from the finite size of the central region, while choosing a bigger ϵ makes these artifacts disappear at the cost of washing out any peaks in y-direction that might be relevant. For $\epsilon = \frac{4}{N}$ there are no artifacts visible and a structure appears with a clear maximum of the density of states at the border of the band, called van-Hove singularity. The presence of such peaks at the border of the band becomes obvious from the dispersion relation $E_k = -2t\cos(ka)$ we calculated in (2.7). The cosine has a slope $\partial E_k/\partial k$ of 0 at k values that belong to the highest and lowest energies, i.e. the band borders. So if we inversely ask for the number of k-vectors that correspond to a certain energy this is $\propto (\partial E_k/\partial k)^{-1}$ and hence diverges at the borders. With $\epsilon = \frac{20}{N}$ this important structure at the band edges washes out and details are lost. An LDoS plot with $\epsilon = 0$ is not shown, since it just shows constant 0 everywhere as no δ-peaks are hit in a computer calculation of the Green's function. We see an additional curved structure at the left and right end of the wire. The electrons are reflected at these points and standing waves emerge. The allowed momenta are limited by the dispersion relation in a lattice, resulting in the Friedel-oscillations visible in the LDoS plots.

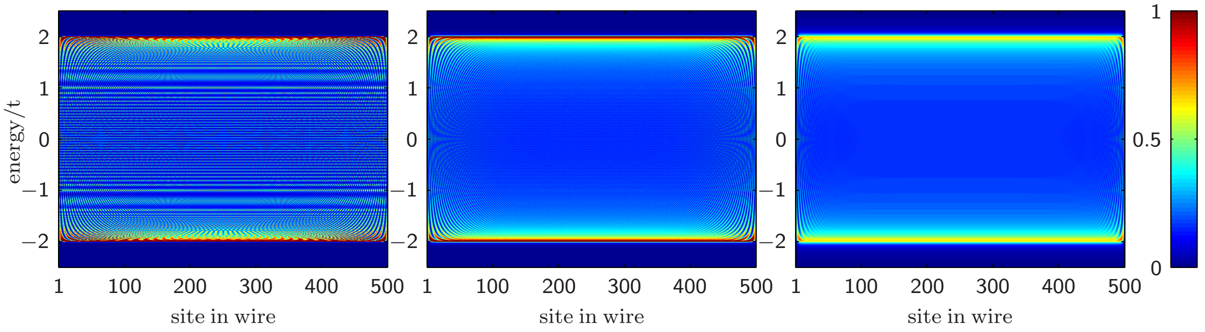

Figure 2.2: LDoS for a wire with chemical potential, shown as color according to the scale on the right over the site in the wire on the x-axis an the energy on the y-axis. A system is considered with $\mu = 0$ and hopping term $t = 1$ for $\epsilon = 2/500$ (left side), $\epsilon = 4/500$ (middle) and $\epsilon = 20/500$ (right side).

2.3 Model of a Quantum Point Contact

To make the Quantum Wire into a Quantum Point Contact a constriction has to be added in the central region, which requires the electrons to have a certain energy to pass through. We can equivalently see this as either making the chemical potential site dependent and letting it follow an additional bump compared to the bulk value or leaving the chemical potential constant and explicitly adding an additional potential term that is 0 everywhere except for the bump region. We choose the second way and gain a new term

$$H_{pot} = \sum_{j=1}^{N} V(j) c_j^\dagger c_j \tag{2.13}$$

in the Hamiltonian. The choice of the Potential $V(j)$ and in particular the curvature at the apex of the bump turn out to be more important than one might naively expect. It has a considerable effect on the LDoS and hence the conductance curves (see for example [Bauer et al., 2013]). But that is not the main topic of this work, so we will choose one reasonable potential of the form

$$V(x) = f \cdot e^{\frac{-x^2}{1-x^2}} \tag{2.14}$$

where x takes values between -1 and 1. The prefactor f determines the height of the potential barrier, corresponding to the width of the constriction that makes up the quantum point contact. To use this Potential to create a barrier with a width of d sites, we have to scale it correctly by using d equidistant variables x_j distributed in such a way that the first site corresponds to $x_1 = -1$ and the last site to $x_d = 1$.

The new term (2.13) only changes the diagonal of our Hamiltonian matrix (2.9) and the LDoS of the wire with quantum point contact can be plotted as figure 2.3 by using (2.12) and introducing a small ϵ as discussed in the previous section.

In the plot it can be seen that the additional potential shifts the whole band upwards, following the potential shape. The van Hove singularity at the border of the band gets shifted upwards along with it, but shows a broadening at the apex of the potential barrier. This shape, called van Hove ridge in [Bauer et al., 2013], gets even more emphasized when interactions are considered and is important for the detailed shape of the conductance step in this system. Nevertheless, we will remain in the non-interacting electron case in this thesis and be content with using the stronger simplification to be able to look at systems with more complicated features instead. Near the slopes of the barrier there are again Friedel-oscillations visible as discussed in the previous section.

The main effect of such a barrier is restricting the electrons that can pass through the wire to those with a high enough energy. That is exactly what is caught by a measurement of the conductance of such a system. As was already mentioned in the beginning of this chapter, the conductance is expected to have a step shape (just a single step for this single band model) which carries a lot of information about the system. So naturally, our next aim is to work towards gaining a formula for the conductance. For that, it is necessary to deal with the lead regions to get back to a description of an infinite wire, so that it even makes sense to talk about conductance.

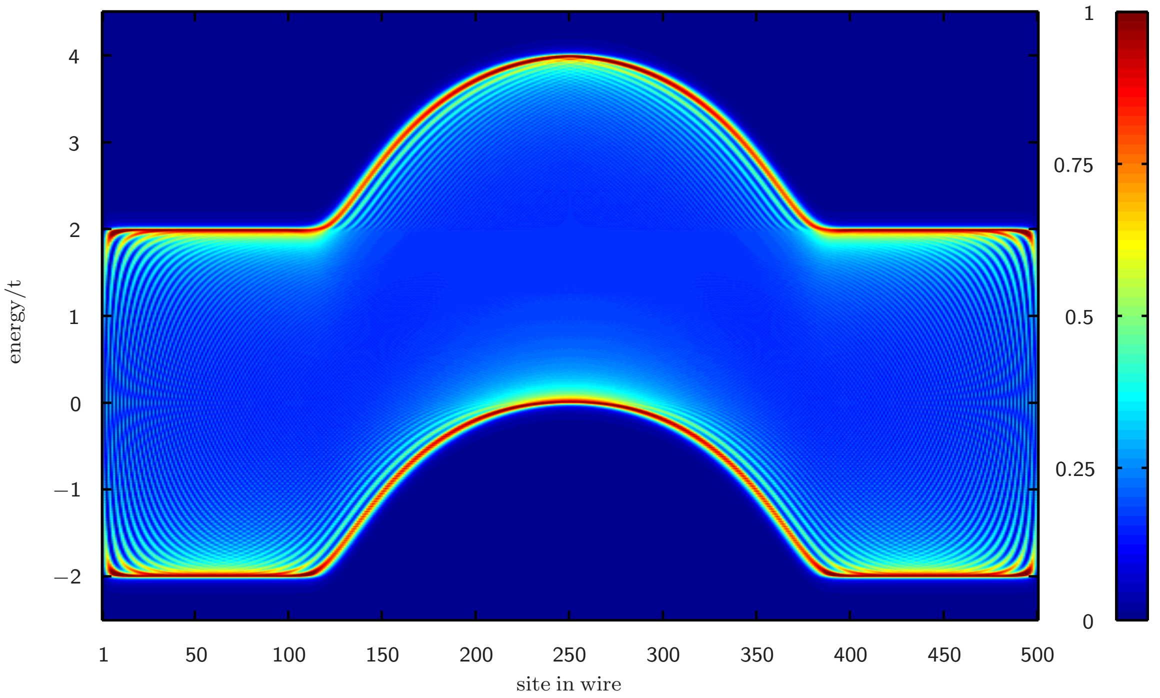

Figure 2.3: LDoS for a wire with a potential barrier of the shape (2.14) modeling a QPC. Parameters $N = 500$ sites, $f = 2.0$ (barrier height) and $\epsilon = 4/N$.

2.4 Adding Semi-Infinite Leads

So far an isolated system without any connection to the environment has been considered. In a later chapter, we will have one case where such a description of an isolated wire is interesting (in chapter 6), but for all other considered systems infinite leads coupled to the central region will be needed.

Instead of a real, thin wire with a gate to induce a potential barrier, quantum point contacts in experiments are often realized as a two-dimensional electron gas being constricted by a gate such that there is only a very small connection between the left and right bulk system left. The small connection is effectively one dimensional, as long as the gate voltage is high enough to strongly constrict the electrons and can then be described with our wire Hamiltonian.

From there, we can think of continuing the wires on both sides to infinity and identify these semi-infinite wires we call leads as the bulk systems. Since the relevant physics happens at the constriction where the system is one dimensional, this is an acceptable model [Bauer et al., 2013].

No matter which physical realization we describe with our model, we are left with the Hamil-

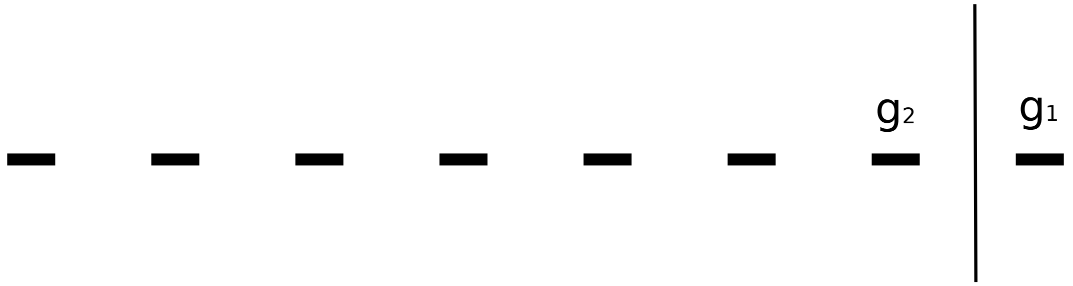

Figure 2.4: A semi infinite lead to the left with a Green's function g_1/g_2 at the right border if a site is added/not added. This means it is implied that the electron sites (black bars) continue infinitely to the left side, but stop at the right site, first at g_2 and then at g_1 after one more site is added. The main idea is that g_1 and g_2 in absense of g_1 must be identical.

tonian of an infinite chain of hopping electrons that can clearly not be written as a matrix in the way described above.

The trick around this is to "project out" the semi-infinite leads which just behave like a wire with no special features. This means to replace them with an additional self-energy term in the calculation of the Green's function. This term has to effectively catch the effect of allowing electrons at the border of the potential region to hop outside into one of the leads, propagate with a Green's function (which has to be determined) at the end of the semi-infinite lead and then hop back in. As the result, we can invert the finite Hamiltonian of the central region plus the extra self-energy term for the lead contributions and end up with the full Green's function for the infinite system.

The basic idea [Karrasch, 2006] to determine the needed semi-infinite lead Green's function is to come up with a consistency relation that this Green's function has to fulfill and then choose the physically sensible solutions to this equation. Since the leads are supposed to be infinitely long, the Green's function at the border must be independent of making them one site shorter or longer (see figure 2.4). Setting those two possible Green's functions equal will give the consistency relation, as will be shown in the following. Note that the potential barrier for the QPC is chosen such that it drops to 0 where the leads begin, so only the constant chemical potential and hopping has to be considered for the leads, while all interesting behavior remains in the central region. The retarded Green's functions we have used so far are also the propagators of the systems, describing the movement (propagation) of the electrons. For the following consideration it is useful to think of them as propagators.

The Hamiltonian matrix of one single isolated site is simply given by $H_0 = -\mu$. So we can calculate the Green's function of this isolated site to be $G^0(\omega) = \frac{1}{\omega - H_0}$. We now connect this single site, indexed as site 1, with a semi-infinite lead (going from site 2 to ∞) that has the still unknown propagator g^L and call the full propagator of the resulting system g^F. It then makes sense to write down the following Dyson equation for the entry of the full propagator g^F that begins at the newly added site 1 and ends at the same site 1:

$$g^F_{11} = G^0_{11} + G^0_{11} t g^L_{22} t g^F_{11}. \tag{2.15}$$

This equation can be understood in the following simple way. An electron of the full system that begins and ends in the site 1 either has stayed there (left term G^0_{11}) or after some time (right term G^0_{11}) it has hopped (t) to site 2 at some point and propagated with the lead Green's function g^L_{22}, returning to site 2 since it must hop (t) back to site 1. After that it could have hopped into the lead and back arbitrarily often which is included in the full propagator g^F_{11} at the end.

The equation can be solved for g^F_{11} and gives us

$$g^F_{11}(\omega) = \frac{1}{(G^0_{11}(\omega))^{-1} - t g^L_{22}(\omega) t} = \frac{1}{\omega - H_0 - t^2 g^L_{22}} \tag{2.16}$$

But seeing this another way, adding the additional site has just made the lead one site longer. This new site is identical to all the infinite sites already contained in it, so the new full system is actually identical to the lead we had before adding a site. This means that g^F_{11} and g^L_{22} are both the Green's function at the border of a semi-infinite lead, hence they must be identical. So we can set $g^F_{11} = g^L_{22} =: g_L$ and get the consistency relation we are looking for:

$$\begin{aligned} g_L &= \frac{1}{\omega + \mu - t^2 g_L} \\ \Rightarrow g_L^{-1} &= \omega + \mu - t^2 g_L \\ \Rightarrow 1 &= (\omega + \mu) g_L - t^2 g_L^2 \\ \Rightarrow g_L &= \frac{1}{2t^2}\left(\omega + \mu \pm \sqrt{(\omega+\mu)^2 - 4t^2}\right). \end{aligned} \tag{2.17}$$

There are two choices for the sign in front of the square root and for each value of ω and μ the correct one must be chosen. To do this, use the physical constraints that firstly the Green's function should be continuous under a small change of μ or ω, secondly that the imaginary part always has to be negative and finally use that $\lim_{\omega \to \infty} g_L(\omega) = 0$. All this together leaves a unique solution given by

$$g_L = \begin{cases} \frac{1}{2t^2}(\omega + \mu + i\sqrt{4t^2 - (\omega+\mu)^2}) & \text{if } \omega + \mu > 2t \\ \frac{1}{2t^2}(\omega + \mu - i\sqrt{4t^2 - (\omega+\mu)^2}) & \text{else.} \end{cases} \tag{2.18}$$

The real and imaginary part of the resulting Green's function are plotted in figure 2.5. In particular, we can see a finite negative imaginary part for energies that lie in the energy band of the lead between $-2t$ and $+2t$. This corresponds to the earlier discussion of the leads giving a finite lifetime to states in the central region by allowing them to escape into the leads. It makes sense that this is limited to states which have an energy that fits into the lead band, hence the imaginary part only for energies in an interval of $4t$.

With finding this entry g_L of the lead Green's function at the border of the lead, the main work to find the full retarded Green's function G for the central region with both leads attached is

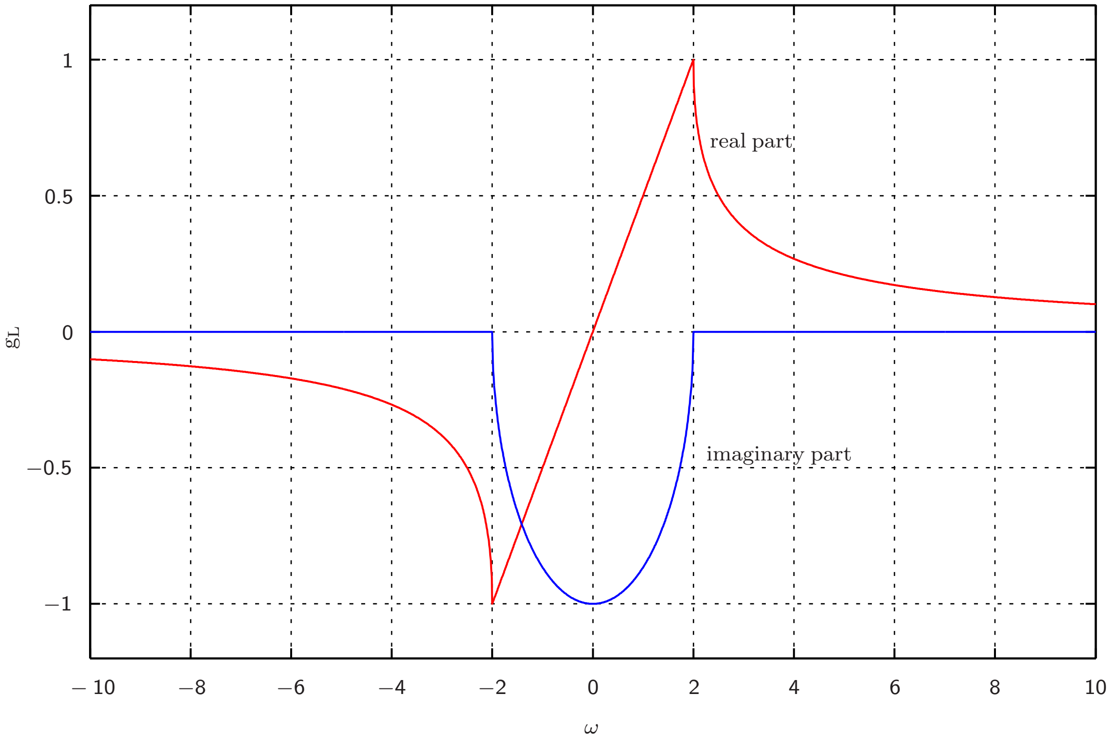

Figure 2.5: Real and imaginary part of the leads Green's function g_L determined in (2.18) by the consistency relation and physical constraints. Parameters set to $t = 1$ and $\mu = 0$.

already done. Labeling the propagator of the isolated central region as G^{central} we can again write a Dyson equation, this time for the G we are ultimately interested in. With the site indices explicitly written and a sum over double indices implied, it reads

$$G_{ij} = G_{ij}^{\text{central}} + G_{ik}^{\text{central}} \Sigma_{kl} G_{lj}, \tag{2.19}$$

where we have introduced a self-energy matrix Σ that allows electrons to hop from the central region into a lead, propagate with g_L and hop back into the central region. Since only the two border sites of the central regions are connected to leads, it is

$$\Sigma_{11}(\omega) = \Sigma_{NN}(\omega) = t g_L(\omega) t \tag{2.20}$$

and $\Sigma_{ij} = 0$ for all other entries. The last step to get our final formula for the total Green's function matrix G is to solve the Dyson equation, giving us

$$G(\omega) = \frac{1}{(G^{\text{central}}(\omega))^{-1} - \Sigma(\omega)} = \frac{1}{\omega - H - \Sigma(\omega) + i0}. \tag{2.21}$$

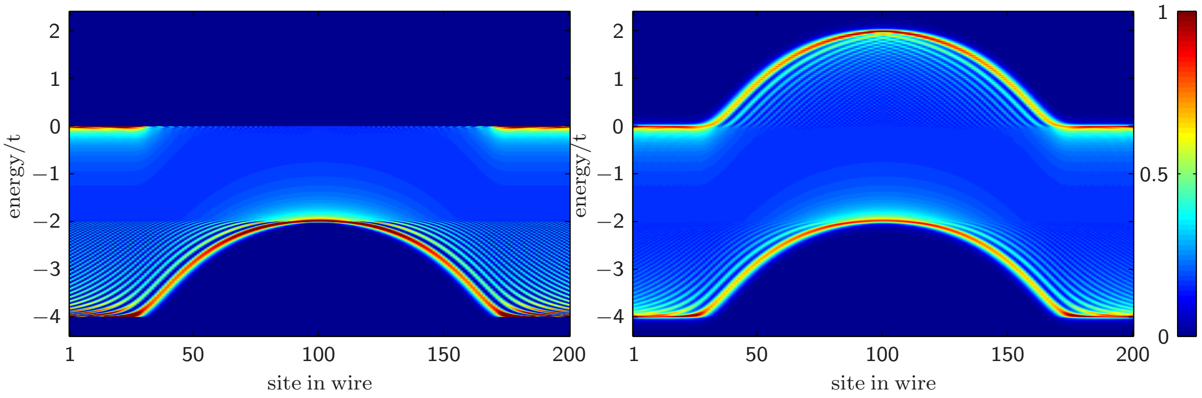

Figure 2.6: The Local Density of States of a wire with a potential barrier of height $f = 2.0$ with $N = 200$ sites connected to two semi-infinite leads with $\epsilon = 0$ (left side) and $\epsilon = 4/N$ (right side).

The whole effect of adding two infinitely long leads is a self-energy correction of just two diagonal entries in the matrix we have to invert to get the Green's function. Even when one adds interactions between the electrons to this system, the Green's function is still given by equation (2.21), but with a more complicated self-energy Σ that includes not only the leads but also the effect of the interactions and has to be determined with methods such as functional renormalization group (see for example [Bauer, 2008]).

We can now use our result (2.21) to calculate the LDoS with formula (2.12). In the resulting figure 2.6, we can see on the left side how the states that are lifted above the band edge of the leads are not visible. As discussed earlier, these are bound state that do not get a finite lifetime from being able to escape into the leads, so they remain δ-peaks that are not hit by the sampled energies for the plot. For the right side the finite ϵ correction has been employed to broaden the δ-peaks, making them visible in the figure. To make sure not to miss interesting structure in the LDoS, we will use the correction as shown on the right from now on.

2.5 Linear Conductance

With the leads taken care of, we now have everything in place to finally calculate the linear conductance through the quantum wire or quantum point contact. Linear conductance in this case means the conductance through our system when an infinitesimal voltage difference is applied. In the regime of such a small perturbation, the system is assumed to give a linear response to it, i.e. a current proportional to the infinitesimal voltage. This is different from the differential conductance considered later in chapter 5, which also expresses the answer of the system to a voltage perturbation on top of a finite voltage difference.

There are different formalisms one can use to express conductance. A rather elementary one is the Landauer formula [Datta, 1995, p.57-59]

$$G^c = \frac{2e^2}{h} T \tag{2.22}$$

which expresses the conductance in terms of the conductance quantum $\frac{e^2}{h}$ and a transmission function T taking values between 0 and 1 that describes how easily electrons can pass through the central region for a given system. The factor 2 comes from the spin degeneracy we have assumed so far - in the next chapter spin-orbit interactions will be considered and the spin will become relevant. This formula is directly related to the conductance staircase mentioned earlier as the $\frac{2e^2}{h}$ is the conductance carried by one mode and the transmission T tells us how fully this mode contributes to conductance. For a multi-mode wire, the conductance would be the sum over many such terms, each with their own T for the modes that become conducting one after the other.

The assumptions used to derive the Landauer formula are reflectionless contacts between the leads and the central region and a system at zero temperature, both of which are given for our case so far. The conductance is called G^c to differentiate it from the Green's function G. The Transmission function T can be expressed in terms of the Scattering matrix which in term can be written in terms of the Green's function $G =: G^R$ (that we know from the previous chapter) by [Datta, 1995, p.148]

$$T = \mathrm{Tr}\left[\Gamma^L G^R \Gamma^R G^A\right] \tag{2.23}$$

where $G^A := (G^R)^\dagger$ is the advanced Green's function. The lead coupling matrices Γ are defined as $\Gamma^k = i[\Sigma_k^R - (\Sigma_k^R)^\dagger]$ with $k \in \{R, L\}$ for left and right lead.

Since the self-energy matrices for just one lead and hence also the coupling matrices have only one nonzero entry each, the trace is easily evaluated to be

$$T = \Gamma_{11}^L G_{1N}^R \Gamma_{NN}^R (G_{N1}^R)^\dagger. \tag{2.24}$$

This is further simplified by $\Gamma_{11}^L = \Gamma_{NN}^R = -2\mathrm{Im}\Sigma^R = -2t^2 g_L$ which gives a final result for the transmission function of

$$T(\omega) = \left|2\ \mathrm{im}(g_L(\omega)) t^2 G_{1N}(\omega)\right|^2. \tag{2.25}$$

The linear conductance at zero temperature considers all the conductance electrons to live exactly at the chemical potential of the system. Since our energy ω is measured relative to the chemical potential μ, we need to take the transmission at $\omega = 0$. With $\mathrm{Im}(g_L(0)) = -1$ for $t = 1$ we end up with a conductance of

$$G^c = \frac{2e^2}{h} T(0) = \frac{2e^2}{h} \left|2t^2 G_{1N}(0)\right|^2. \tag{2.26}$$

The important result here is that the linear conductance is proportional to the square of the absolute value of just the top right corner entry of the Green's function matrix. This entry is readily available from the preceding calculation. It should be noted that the conductance of course only depends on states in the central region which can connect to the leads and have a finite lifetime, so we should not include the small but finite ϵ summand when calculating the Green's function to use it in 2.26 - it could only make the results worse.

At this point, we have just cited the main results (2.22) and (2.23) without a derivation. This is done due to chapter 5 containing a very explicit derivation of differential conductance in a more general formulation that contains (2.26) as a special case, so there would be not much benefit in giving a simplified version of the same calculation here.

The usual parameter that is tuned to look at conductance of such 1D wires is to shift the height of the potential barrier, lowering it from just above the chemical potential to below or vice versa. In similarity to experiments, we call this height parameter V_g for gate voltage - but note that contrary to experiments, our V_g will have the unit of energy instead of voltage, since it describes a shift of the potential barrier height.

We expect the conductance to change from 0 to 1 (conductance quanta) as the chemical potential is crossed, so the interesting feature will be the conductance step between these values. It was mentioned earlier how the width and shape of the potential actually makes a considerable difference in the conductance, so the step is plotted in figure 2.7 for different values of barrier width to show this effect and to show a typical conductance plot in general.

The influence of the width of the barrier, which changes the curvature of the potential, can clearly be seen: The wider the potential barrier and hence the smaller the curvature of the potential at its apex, the steeper the conductance curve will be. In fact, one can use the curvature at the top of a potential of width d to define an energy scale $\Omega_x = 4\sqrt{2}/d$, and when the gate-voltages V_g are expressed in these units all the curves from figure 2.7 now collapse into a single one in figure 2.8 ([Büttiker, 1990]).

As a side remark, with our one band wire we of course can only get access to the very first step of the conductance ladder mentioned in the introduction. But the first one happens to be the particularly interesting one as it contains the 0.7 anomaly that has enjoyed some controversy ([Reilly et al., 2002]) about whether its origin is of Kondo nature ([Meir et al., 2002]) and is likely explained in [Bauer et al., 2013].

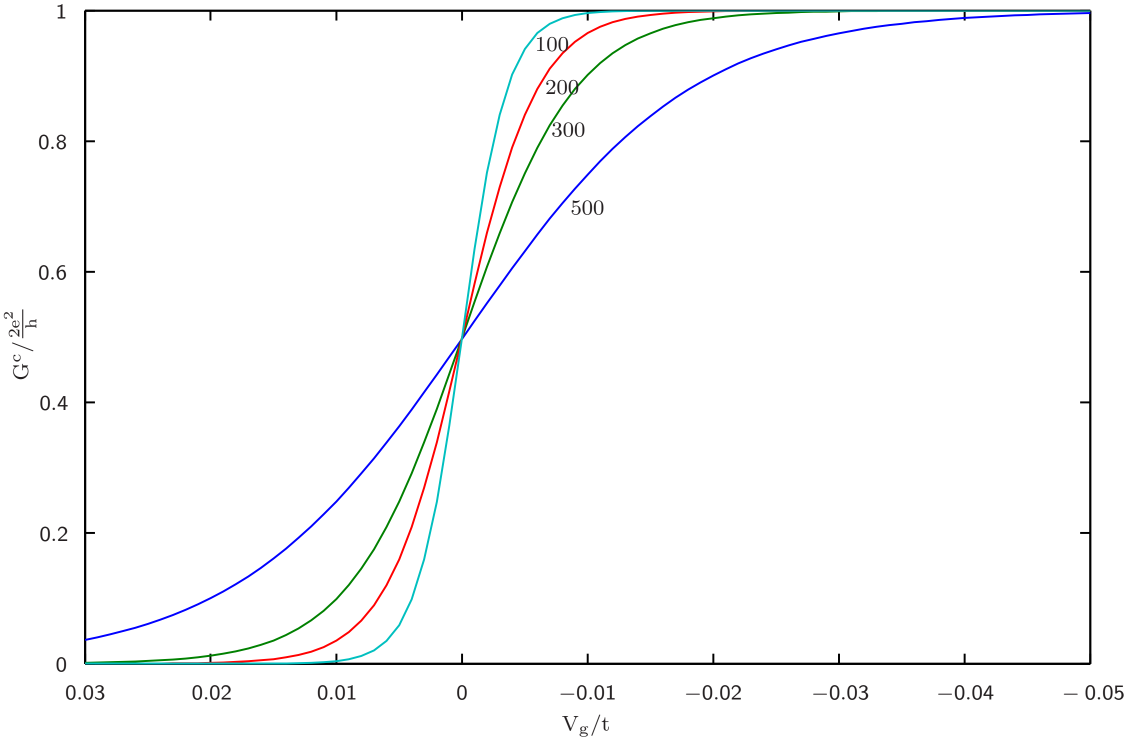

Figure 2.7: The conductance G^c through a quantum point contact (y-axis) as the apex of a potential barrier is shifted over the chemical potential $\mu = 0$ (x-axis) by a height V_g for different potential barrier width from $d = 100$ to $d = 500$.

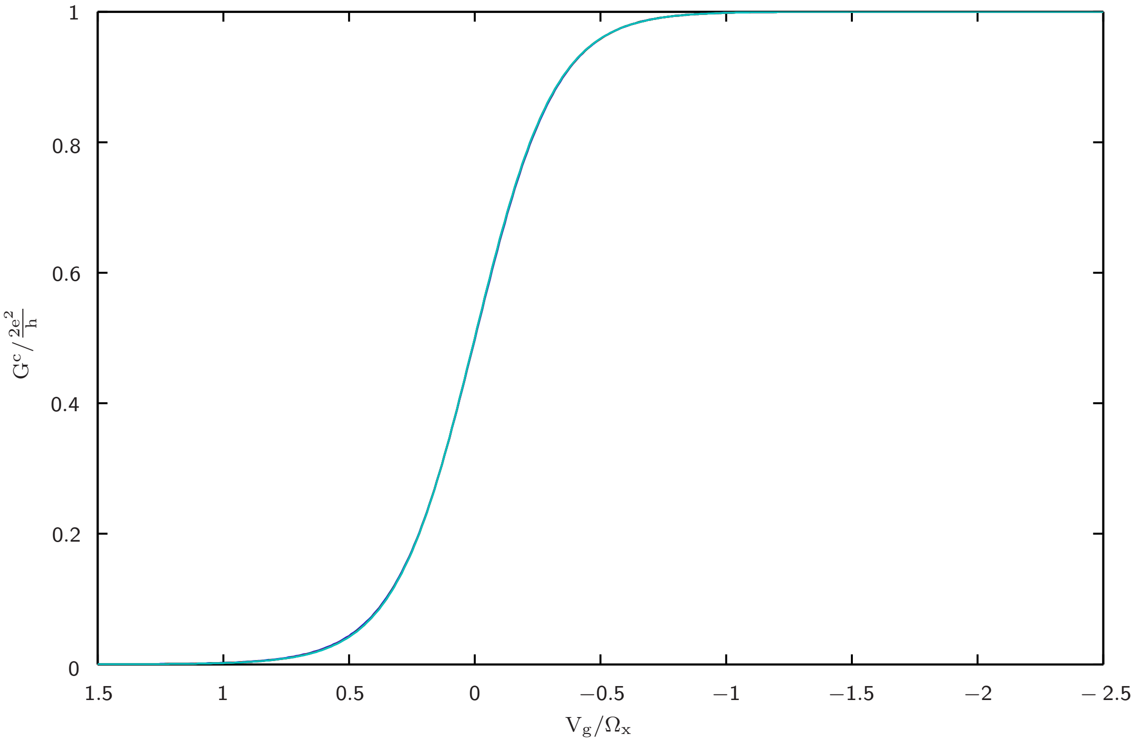

Figure 2.8: The conductance through a quantum point contact when the apex of the potential barrier is shifted over the chemical potential $\mu = 0$ by a height V_g expressed in units of the energy scale Ω_x describing the curvature of the potential at its apex. All the conductance curves for different barrier width collapse into one graph now.

Chapter 3

Spin Orbit Interaction and Magnetic Field

So far we have made the approximation not to explicitly include a spin degree of freedom and just assumed that, measuring in any direction, both spin species will be degenerate. The only resulting effect was a factor 2 from the implied sum over both spin directions in the conductance formula (2.22). In the following chapters about Majorana fermions, we will mostly consider a model (4.2) that does not see the spins as degenerate, but explicitly requires only one of the spin species to be present. For that case, a spinless description as we have used so far is sufficient and introducing spins would not be necessary.

Nevertheless, there are two good reasons for us to concern ourselves with the spin degrees of freedom in this chapter. Firstly, both external magnetic fields and internal magnetic fields from so called spin-orbit-interaction (section 3.1) act on and differentiate between the spins and as we will see have a noticeable impact on the behavior of quantum wires and QPC, so including them is a sensible extension to the model introduced in the first chapter, allowing for a more accurate description in many situations. Secondly, even though we consider a single spin model in the following chapters, the wires in experimental realizations will in the beginning contain electrons of both spins. As will be explained in more detail in the next chapter, one has to go to great length to fully polarize the electrons in an experimental setup in a way that makes the system effectively behave like the theoretical single spin model ([Alicea, 2012]) and the main ingredients to achieve this are exactly the two effects we introduce in this chapter: spin-orbit-interaction and Zeeman effect. Hence looking at those effects and their influence on the behavior of the system (section 3.4) will be important to understand the connection between theory and experiment in the following chapters.

After considering these results, the chapter closes with two short sections about technical details. First we have a look at a more efficient approach to calculate the relevant entries of the Green's function for the LDoS (section 3.5) since the matrices we have to invert get twice as big by introducing spin and fully inverting them could take unnecessarily long. The same approach is applicable in the case of a superconducting wire, which doubles the matrix dimensions as well. Finally, we justify the implicit approximation to only take spin-orbit terms up to lowest order into account. The effect of higher order terms are briefly considered (section 3.6) and it becomes clear that they are very small and hence rightfully neglected.

3.1 Spin Orbit Term and Zeeman Term

We begin by introducing an external magnetic field to our model. The electrons carry a spin, giving them a spin-magnetic-moment which feels this magnetic field. So from now on we can no longer assume the electron states for both possible spin directions to be degenerate and instead have to account for the spins of the electrons as an additional degree of freedom. The interaction of the magnetic field $\mathbf{B}$ with the spin of the electrons can be described by a Zeeman term

$$\mathrm{H}_Z = \gamma\,\mathbf{B}\cdot\sigma \tag{3.1}$$

where γ gives the interaction strength and σ is a vector consisting of the three Pauli-matrices

$$\sigma_x = \begin{pmatrix} 0 & 1 \\ 1 & 0 \end{pmatrix} \qquad \sigma_y = \begin{pmatrix} 0 & -i \\ i & 0 \end{pmatrix} \qquad \sigma_z = \begin{pmatrix} 1 & 0 \\ 0 & -1 \end{pmatrix} \tag{3.2}$$

which act on spin-space. For convenience we can set $\gamma = -1$ and only vary the strength of $\mathbf{B}$.

Now that the electrons carry a spin, another effect can also be taken into account: the interaction of the spin-magnetic-moment with a magnetic field that is induced by the motion of the electrons in their surrounding electrical field, called spin-orbit-interaction (SOI). Depending on the origin of the electrical field we distinguish between Rashba SOI ([Bychkov and Rashba, 1984]) when it comes from the potential that confines our system to effectively one dimension and Dresselhaus SOI ([Dresselhaus, 1955]) when asymmetries in the lattice are the origin ([Goulko et al., 2014], [Winkler, 2003]).

The relevant effect for us will be the Rashba SOI. Its form can be determined ([Birkholz, 2008, chapter 2]) to be

$$\mathrm{H}_{SOI} = -\alpha_0\ \sigma\cdot(\mathbf{E}\times\mathbf{p}) \tag{3.3}$$

where $\alpha_0 = \frac{e\hbar}{4m^2c^2}$ contains the physical constants, $\mathbf{E}$ is the electric field given by the gradient of the potential that confines our system to a wire and σ is again the vector of Pauli-matrices.

To simplify this term we can w.l.o.g. assume the wire or QPC in our model to lie along the x-direction. Then the momentum is limited to having a contribution in this direction, $p = (p_x, 0, 0)$, so (3.3) simplifies to

$$\mathrm{H}_{SOI} = -\alpha_0\sigma\cdot\begin{pmatrix} 0 \\ E_z p_x \\ -E_y p_x \end{pmatrix} = -\underbrace{\alpha_0 E_z}_{\alpha_z}\sigma_y p_x + \underbrace{\alpha_0 E_y}_{\alpha_y}\sigma_z p_x. \tag{3.4}$$

To include these new terms into the numerical approach from the previous chapter, we need to express them as a matrix Hamiltonian similar to what we did in section 2.1. The difference this time is the spin as an explicit index for the creation and annihilation operators, so we will need a matrix with twice the rows/columns to take this additional degree of freedom into account. To attain this matrix, first define a vector $\Psi_j^\dagger = \left(c^\dagger_{j\uparrow}, c^\dagger_{j\downarrow}\right)$ for each of the sites j. We can then begin to rewrite the Hamiltonian in terms of creation and annihilation operators as used at the beginning of the second chapter and get

$$\begin{aligned}
\mathbf{H}_{SOI} = \sum_j \Psi_j^\dagger \mathrm{H}_{SOI} \Psi_j = \sum_j \left(c^\dagger_{j\uparrow}, c^\dagger_{j\downarrow}\right) &\left[(\alpha_y\sigma_z - \alpha_z\sigma_y)\underbrace{(-i\hbar)\frac{\mathrm{d}}{\mathrm{d}x}}_{p_x}\right]\begin{pmatrix} c_{j\uparrow} \\ c_{j\downarrow} \end{pmatrix} \\
= -i\hbar \sum_j \left(c^\dagger_{j\uparrow}, c^\dagger_{j\downarrow}\right)&(\alpha_y\sigma_z - \alpha_z\sigma_y)\frac{1}{2a}\begin{pmatrix} c_{j+1\uparrow} - c_{j-1\uparrow} \\ c_{j+1\downarrow} - c_{j-1\downarrow} \end{pmatrix} \\
= -\frac{\hbar}{2a}\sum_j \Bigg[\alpha_y \left(c^\dagger_{j\uparrow}, c^\dagger_{j\downarrow}\right)&\begin{pmatrix} ic_{j+1\uparrow} - ic_{j-1\uparrow} \\ -ic_{j+1\downarrow} + ic_{j-1\downarrow} \end{pmatrix} - \alpha_z \left(c^\dagger_{j\uparrow}, c^\dagger_{j\downarrow}\right)\begin{pmatrix} c_{j+1\downarrow} - c_{j-1\downarrow} \\ -c_{j+1\uparrow} + c_{j-1\uparrow} \end{pmatrix}\Bigg] \\
= -\frac{\hbar}{2a}\alpha_y \sum_j &\left[ic^\dagger_{j\uparrow}c_{j+1\uparrow} - ic^\dagger_{j\uparrow}c_{j-1\uparrow} - ic^\dagger_{j\downarrow}c_{j+1\downarrow} + ic^\dagger_{j\downarrow}c_{j-1\downarrow}\right] \\
+ \frac{\hbar}{2a}\alpha_z \sum_j &\left[c^\dagger_{j\uparrow}c_{j+1\downarrow} - c^\dagger_{j\uparrow}c_{j-1\downarrow} - c^\dagger_{j\downarrow}c_{j+1\downarrow} + c^\dagger_{j\uparrow}c_{j-1\uparrow}\right]
\end{aligned} \tag{3.5}$$

where we have discretized the derivative in the momentum operator in the second line. Absorbing the prefactors into the α_y and α_z and shifting some summation indices, the SOI Rashba term is finally given by

$$\mathbf{H}_{SOI} = \alpha_y \sum_{j=1}^{N-1}(ic^\dagger_{j+1\uparrow}c_{j\uparrow} - ic^\dagger_{j+1\downarrow}c_{j\downarrow} + h.c.) - \alpha_z \sum_{j=1}^{N-1}(c^\dagger_{j+1\uparrow}c_{j\downarrow} - c^\dagger_{j+1\downarrow}c_{j\uparrow} + h.c.), \tag{3.6}$$

so we have additional spin-keeping and spin-flipping hopping terms with different prefactors.

In a similar way we can bring the Zeeman term (3.1) into this form. We express the external magnetic field $\mathbf{B}$ in spherical coordinates $(\theta, \phi, B = |\mathbf{B}|)$ and rewrite (3.1) with the same approach as

$$\begin{aligned}
\mathbf{H}_Z = \gamma \sum_{j=1}^{N}(c^\dagger_{j\uparrow}c^\dagger_{j\downarrow})&\left[\begin{pmatrix} B\sin(\theta)\cos(\phi) \\ B\sin(\theta)\sin(\phi) \\ B\cos(\theta) \end{pmatrix}\cdot\sigma\right]\begin{pmatrix} c_{j\uparrow} \\ c_{j\downarrow} \end{pmatrix} \\
= B\gamma \sum_{j=1}^{N}\Bigg[\sin(\theta)\cos(\phi)&(c^\dagger_{j\uparrow}c^\dagger_{j\downarrow})\begin{pmatrix} c_{j\downarrow} \\ c_{j\uparrow} \end{pmatrix} + \sin(\theta)\sin(\phi)(c^\dagger_{j\uparrow}c^\dagger_{j\downarrow})\begin{pmatrix} -ic_{j\downarrow} \\ ic_{j\uparrow} \end{pmatrix}
\end{aligned}$$

$$+\cos(\theta)(c^\dagger_{j\uparrow}c^\dagger_{j\downarrow})\begin{pmatrix} c_{j\uparrow} \\ -c_{j\downarrow}\end{pmatrix}\Bigg]$$

$$\begin{aligned}= B\gamma\sum_{j=1}^{N}\Big(&\sin(\theta)\cos(\phi)c^\dagger_{j\uparrow}c_{j\downarrow} - i\sin(\theta)\sin(\phi)c^\dagger_{j\uparrow}c_{j\downarrow} \\ &+\cos(\theta)(c^\dagger_{j\uparrow}c_{j\uparrow} - c^\dagger_{j\downarrow}c_{j\downarrow}) + \text{h.c.}\Big)\,.\end{aligned} \tag{3.7}$$

This term is valid for a completely arbitrary direction of the external magnetic field, given by the angles θ and ϕ, which is more general than we will actually need.

As we know from section 2.4, a QPC structure is often a constriction introduced into a two dimensional electron gas due to a gate structure ([Bauer et al., 2013]), but there are also experiments dealing with actual very thin wires that have gates below them to induce an external potential barrier ([Das et al., 2012], [Mourik et al., 2012]). Either way, we assume the effective or real wire to lie along the x-axis. We want to be able to realize an arbitrary angle between the external and SOI magnetic fields and choose to put both magnetic fields into the xy-plane. Therefore the Rashba SOI field is considered in y-direction, since a SOI in x-direction would only be present in Dresselhaus SOI from asymmetries in the lattice which we do not consider here.

The external field in the xy-plane will mostly be taken orthogonal to the SOI field, so we have $\mathbf{B} = (B, 0, 0)$, which corresponds to $\theta = \frac{\pi}{2}$ and $\phi = 0$. This simplifies the Zeeman term considerably to

$$\mathbf{H}_Z = B\gamma\sum_{j=1}^{N}\left(c^\dagger_{j\uparrow}c_{j\downarrow} + c^\dagger_{j\downarrow}c_{j\uparrow}\right)\,. \tag{3.8}$$

These conventions mostly follow [Goulko et al., 2014] where the same kind of system is considered without and even with interactions included.

So in summary, the external magnetic field gives us a term (3.8) that allows for on-site spin-flips while the spin-orbit-interaction (3.6) modifies the hopping amplitudes (α_y term) and creates a new spin-flip hopping term (α_z term).

3.2 Dispersion Relation

Before we include these new terms in our approach from the previous chapter, we can investigate their effects on a bare wire by examining how they change the dispersion relation of the system. We go back to the continuous one dimensional electron gas, which has the same band shape as our effective lattice model in the important low energy regime. Since a bare wire is considered for the moment, we can stay in momentum space this time and easily extract the dispersion relation. The Hamiltonian we want is given by

$$H = \frac{p^2}{2m} - \mu + \alpha p\sigma_z + B_{\|}\sigma_z + B_{\perp}\sigma_x. \tag{3.9}$$

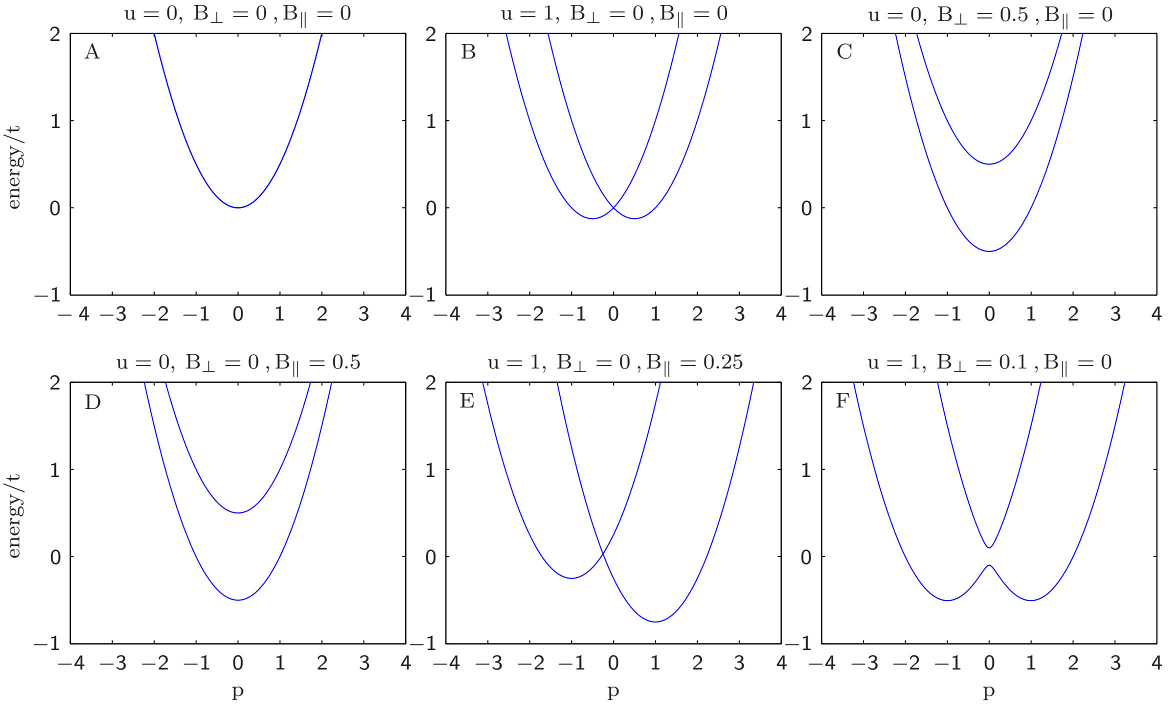

Figure 3.1: Dispersion relation of the wire for various SOI strength and external magnetic fields. (A) Dispersion relation with no spin effects. (B) Rashba SOI term splits the bands in momentum. (C,D) B-field in any direction splits the spin bands in energy. (E) Parallel magnetic field adds both effects and splits bands both in momentum in energy. (F) Orthogonal B-field allow spin flipping and hence lead to avoided crossing as both spin bands are allowed to mix.

The direction of $(\mathbf{E} \times \mathbf{p})$ is called the z-direction and taken as the quantization direction for the spins in this short section. Then the Rashba SOI term (3.3) is proportional to our one dimensional p with some factor α which we use to set the strength of the spin-orbit-interaction and the Pauli-matrix σ_z. Up to the momentum dependence the term resembles a Zeeman term with a magnetic field in this z-direction. For that reason the SOI is sometimes described by an effective magnetic field in said direction. For the external magnetic field it is enough to consider a term parallel and one perpendicular to the z-direction since rotating the field around the z-axis changes nothing.

Writing (3.9) as a 2x2 matrix in spin-space and diagonalizing it gives us the dispersion relation plotted in figure 3.1. Without any terms that couple to spin the bands are degenerate and lie on top of each other (diagram A). The SOI term with its p-dependence splits the bands in momentum direction (diagram B) while an external magnetic field splits the bands in energy direction by distinguishing between spins parallel and antiparallel to the field (diagram C and D). Both effects together, with an external magnetic field chosen parallel to the z-direction, just give a shift of both bands in momentum and energy (diagram E). The interesting case is shown in diagram F with a field perpendicular to the z-direction. The magnetic field allows the spins to be flipped between both bands, leading to an avoided crossing at the intersection point and creating a gap of a width $\sim 2B_\perp$ at $p = 0$. From now on we will mostly consider this case of an external field perpendicular to the effective SOI magnetic field.

3.3 Hamiltonian Matrix with Spin

In the following we want to use our approach from the previous chapter to observe the changes in the system when we take the new terms into consideration. The full Hamiltonian is given by

$$\mathbf{H} = \sum_{\sigma=\{\uparrow,\downarrow\}} \sum_{j=1}^{N} \epsilon_j c^\dagger_{j\sigma} c_{j\sigma} - t \sum_{\sigma=\{\uparrow,\downarrow\}} \sum_{j=1}^{N-1} \left(c^\dagger_{j+1\sigma} c_{j\sigma} + \text{h.c.} \right) + \mathbf{H}_Z + \mathbf{H}_{SOI} \tag{3.10}$$

with $\epsilon_j = -\mu + V(j)$. It is straight forward to write this into a Hamiltonian matrix H by introducing a doubled basis $\Psi = (a_{1\uparrow}, a_{1\downarrow}, a_{2\uparrow}, a_{2\downarrow}, ..., a_{N\uparrow}, a_{N\downarrow})^T$ for spin-up and spin-down electrons. The resulting matrix is given by

$$\mathbf{H} = \Psi^\dagger \begin{pmatrix} -\mu + V_1 & B\gamma & -i\alpha_y - t & \alpha_z & 0 & 0 & 0 \\ B\gamma & -\mu + V_1 & -\alpha_z & +i\alpha_y - t & 0 & 0 & 0 \\ i\alpha_y - t & -\alpha_z & -\mu + V_2 & B\gamma & -i\alpha_y - t & \alpha_z & 0 \\ \alpha_z & -i\alpha_y - t & B\gamma & -\mu + V_2 & -\alpha_z & +i\alpha_y - t & 0 \\ 0 & 0 & i\alpha_y - t & -\alpha_z & -\mu + V_3 & B\gamma & \cdots \\ 0 & 0 & \alpha_z & -i\alpha_y - t & B\gamma & -\mu + V_3 & \cdots \\ 0 & 0 & 0 & 0 & \vdots & \vdots & \ddots \end{pmatrix} \Psi. \tag{3.11}$$

The next step is to calculate the Green's function by formula (2.21), which mainly involves taking the inverse of this matrix modified by the self-energy from the leads. To get this self-energy, we now have to decide what leads we want to connect to this central region.

In the previous chapter we had leads with neither external magnetic field nor spin-orbit effects. Since adding these effects to the leads mainly changes the band-edges and has very little impact on the middle of the band where the chemical potential lies, we can expect even the bare self-energy (2.20) from the previous chapter to be a good, although lazy approximation.

Adding the spin-orbit-effect to the leads is possible, but it requires a numerical solution of the consistency relation that was necessary to get the leads Green's function (see section 2.4) instead of an analytic solution. This is included in [Goulko et al., 2014], but the resulting conductance curves are indistinguishable from the results we will get (figure 3.4) with the much simpler analytic term, so we conclude that it is negligible. Instead we will include SOI only in the central region, but let its strength smoothly drop towards the leads.

Giving the leads an external magnetic field on the other hand can easily be done. For the central region, we have chosen a spin-quantization in z-direction; call a vector in this spin basis $\Psi_{\uparrow\downarrow}$. But our leads are assumed to only feel the external magnetic field, so it is convenient to choose this direction for spin-quantization with vectors $\Psi_{\nearrow\!\!\swarrow} = (\Psi_{\nearrow}, \Psi_{\swarrow})^T$. The self-energy from such a lead is very simple in this basis and just given by

$$\tilde{\boldsymbol{\Sigma}} = \Psi^\dagger_{\nearrow\!\!\swarrow} \tilde{\Sigma} \Psi_{\nearrow\!\!\swarrow} = (\Psi^\dagger_{\nearrow} \Psi^\dagger_{\swarrow}) \begin{pmatrix} t^2 g_L(\omega - \frac{\gamma B}{2}) & 0 \\ 0 & t^2 g_L(\omega + \frac{\gamma B}{2}) \end{pmatrix} \begin{pmatrix} \Psi_{\nearrow} \\ \Psi_{\swarrow} \end{pmatrix} \tag{3.12}$$

where the site index is left out for now but can easily be added back later - these 4 entries are of course the ones corresponding to either the first or last site of the central region. Such vectors in spin-basis can be rotated around a direction $\hat{n}$ by an angle β by a rotation operator $R(\hat{n}, \beta) = e^{-\frac{i}{2}\beta \hat{n}\cdot\sigma}$, so we know that

$$\Psi_{\uparrow\downarrow} = R(\hat{e}_y, \theta) R(\hat{e}_z, -\phi) \Psi_{\nearrow\!\!\swarrow} =: \mathbf{R} \Psi_{\nearrow\!\!\swarrow} \tag{3.13}$$

where θ and ϕ describe the external magnetic field direction as defined earlier. Now we can transform the self-energy matrix into the spin-basis of our central region

$$\tilde{\boldsymbol{\Sigma}} = \Psi^\dagger_{\nearrow\!\!\swarrow} \underbrace{\mathbf{R}^\dagger \mathbf{R}}_{\mathbb{1}} \tilde{\Sigma} \underbrace{\mathbf{R}^\dagger \mathbf{R}}_{\mathbb{1}} \Psi_{\nearrow\!\!\swarrow} = \Psi^\dagger_{\uparrow\downarrow} \underbrace{\mathbf{R} \tilde{\Sigma} \mathbf{R}^\dagger}_{\Sigma} \Psi_{\uparrow\downarrow} \tag{3.14}$$

and get

$$\Sigma = \mathbf{R}\tilde{\Sigma}\mathbf{R}^\dagger = \begin{pmatrix} t^2 g_L^- \cos^2(\theta/2) + t^2 g_L^+ \sin^2(\theta/2) & t^2 (g_L^- - g_L^+) \sin(\theta/2)\cos(\theta/2) \\ t^2 (g_L^- - g_L^+) \sin(\theta/2)\cos(\theta/2) & t^2 g_L^- \sin^2(\theta/2) + t^2 g_L^+ \cos^2(\theta/2) \end{pmatrix} \tag{3.15}$$

with $g_L^- = g_L(\omega - \frac{\gamma B}{2})$ and $g_L^+ = g_L(\omega + \frac{\gamma B}{2})$. As one would expect, the result is independent of ϕ, since only the relative angle between external magnetic field and z-direction matters, which is given by θ. The full self-energy matrix we need adds this 2x2 matrix to the top left and bottom right block of 3.11.

The diagonal elements of the Green's function then give us the LDoS (2.12) where we now have a separate density for spin-up and spin-down electrons. Of course, inverting this (with dimensions $2N$x$2N$ possibly quite big) matrix when we only need the diagonal of the inverse is very inefficient, especially since we have to redo it for many energies for an LDoS plot. There is a way to get only the diagonal entries of the Green's function much more efficiently, which will be briefly explained in section 3.5.

Before we look at some numerical results, first a little note about the hopping amplitude t. The new SOI terms that we have introduced also give an additional hopping term, thus changing the amplitude of the hopping, depending on the direction in which we consider spin orbit interaction. But the hopping amplitude influences the dispersion relation, and the curvature at the minimum of the dispersion relation in term determines the effective mass. So depending on the SOI term we might actually consider a physically slightly different systems, which makes them harder to compare. In the presence of spins the hopping between two sites is given by a 2x2 matrix to include the spin-flip hopping. Without the SOI terms, we had a hopping of $t = 1$ which corresponds to this matrix having a determinant of one. Now it is given by

$$\det\begin{pmatrix} -i\alpha_y - t & \alpha_z \\ -\alpha_z & i\alpha_y - t \end{pmatrix} = t^2 + \alpha_y^2 + \alpha_z^2, \tag{3.16}$$

which equals 1 when we adjust the value of t to be

$$t = \sqrt{1 - \alpha_y^2 - \alpha_z^2}. \tag{3.17}$$

3.4 Effects on LDoS and Conductance

So let us now investigate the effect of the different new terms in the Hamiltonian on the LDoS and conductance. We start with an external magnetic field in different directions. Since our Hamiltonian is set up with creation and annihilation operators for electrons with spin in z-direction up or down, a magnetic field in z-direction directly increases/lowers the band relative to the chemical potential, and hence change the effective barrier that the two kinds of electrons can see. This is shown in the middle diagram in figure 3.2 where the LDoS of the spin-up/down electrons can be seen on the left/right half of each of the diagrams. The spin-up electrons see a lower barrier since their magnetic moment tries to align itself anti-parallel to the magnetic field. When the external magnetic field is chosen perpendicular to the spin-quantization, both spin species get split up equally into two partly overlapping bands, since the electrons now have no preference for their spin in the magnetic field direction. This case is shown in the right diagram in figure 3.2 for the example of a magnetic field in x-direction.

Now let us explore the spin-orbit-interaction terms. We want a SOI magnetic field in y-direction, which is the $\alpha_z \neq 0$ and $\alpha_y = 0$ case in (3.6), since the z direction of α_z corresponds to the electric field that constrains the electrons in the wire, while the resulting effective magnetic field is in y-direction (as can be seen from this term containing the σ_y Pauli-matrix). The result is a sideways shift in the dispersion relation (figure 3.1) which is not visible in the LDoS and a small widening of the band from the increased hopping amplitude (see middle diagram of figure 3.3) and hence an energy shift which gets corrected by our adjustment (3.17) of the hopping amplitude as can be seen in the right diagram of figure 3.3. The same behavior can be found for SOI magnetic field in z-direction ($\alpha_y \neq 0$).

For the conductance through the system, we first return to the convenient energy unit Ω_x introduced in section 2.5, which makes the conductance curves independent of the width of the potential barrier. The interesting parameters to vary are the strength of the magnetic field (in x-direction) and the strength of the SOI (taken in y direction, $\alpha_z \neq 0$ case). Just changing one of them at a time has the effect one would expect. The magnetic field creates an additional shoulder in the middle of the conductance step (figure 3.4 top left) from splitting the electrons into two bands that cross the barrier energy separately. The SOI alone on the other hand does not change the conductance, as it already did not change the LDoS (figure 3.3), as long as we employ the hopping adjustment (3.17) to keep the width of the band constant. The much more interesting and complex

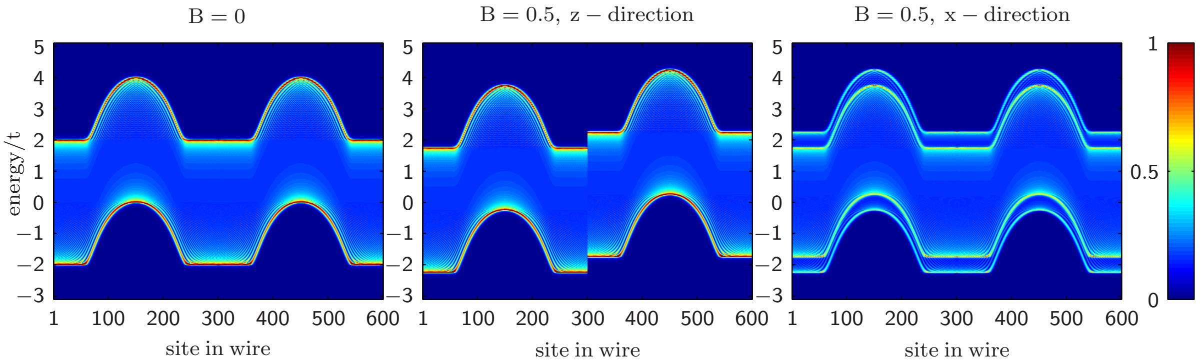

Figure 3.2: Local density of state of the system described by 3.10 with $\alpha_y = \alpha_z = 0$ and B-field in various directions. The x-axis shows the sites in the wire: 1-300 correspond to the LDoS of the spin-up electrons in the wire; 301-600 are again the same 300 sites but show the spin-down LDoS instead. $N = 300$, $\epsilon = 4/200$, potential height $f = 2.0$, barrier width $d = 200$.
(Left plot) No magnetic field. Both spins show equal LDoS.
(Middle plot) Magnetic field B=0.25 in z-direction ($\theta = 0$, $\phi = 0$).
(Right plot) Magnetic field B=0.25 in x-direction ($\theta = \pi/2$, $\phi = 0$).

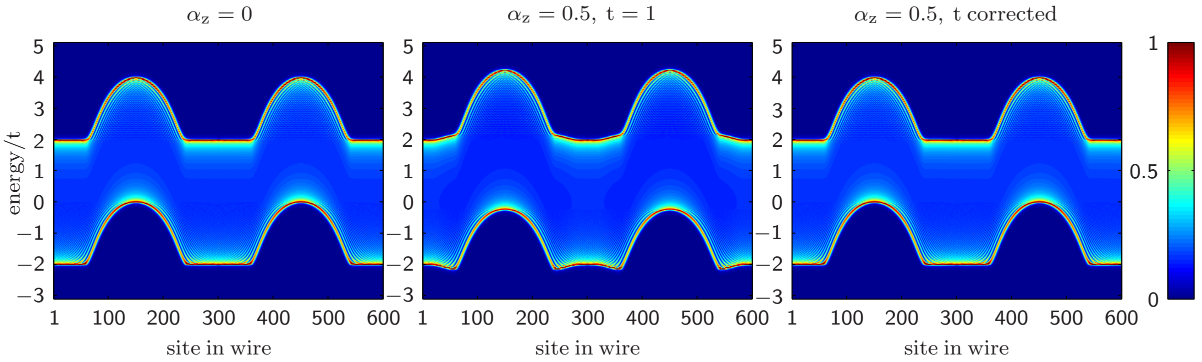

Figure 3.3: LDoS with SOI but no external magnetic field. $N = 300$, $\epsilon = 4/200$, $f = 2.0$, barrier width $d = 200$. Again, the first 300 sites correspond to the spin-up electrons, the sites 301-600 give the density on the same 300 sites but for the spin-down electrons.
(Left plot) No SOI.
(Middle plot) $\alpha_z = 0.5$ with $t = 1$ constant hopping. It can be seen how the band widens from the leads towards the center, resulting in an effectively lower potential barrier for the electrons at the chemical potential.
(Right plot) $\alpha_z = 0.5$ and t adjusted by (3.17). The adjustment of t counteracts the widening from the SOI term, giving the same LDoS as for no SOI present.

behavior comes up when one looks at the interplay of both effects, as can be seen in the remaining plots in figure 3.4. A detailed analysis of these structures can be found in [Goulko et al., 2014], an important feature is that the symmetry of the shape of the step is very much destroyed.

So far we have only considered the total conductance of any electrons through the system, which is now actually a sum of four contributions. It can be split up into the spin-up to spin-up, spin-up to spin-down, spin-down to spin-down and spin-down to spin-up conductance. To calculate each of these values, we have to put the correct entry of the Green's functions into the conductance formula (2.26), in particular we can think of the matrix Hamiltonian and hence the Green's function as consisting of many 2x2 matrices each representing one site or the hopping/interaction between two particular sites. The top right 2x2 matrix gives the 'hopping' from the first to the last site with one entry for each of the 4 cases.

First, take an external magnetic field only in z-direction and no SOI. There are no terms connecting the spin sectors, so spin-changing conductance is impossible in this case. As was seen in the LDoS in the middle plot in figure 3.2, the two spin sectors see different height potentials which now correspond to a conductance step at different gate voltages in figure 3.5. Eventually as the magnetic field gets strong enough to fully separate both steps, an additional shoulder of the total conductance appears.

When we change the external magnetic field into the x-direction, the occurring magnetic term in the Hamiltonian makes spin-changing conductance possible (top row in figure 3.6). The oscillation between a dominating spin-change and a spin-keeping conductance for an increasing magnetic field is due to Larmor precession of the spins in the external magnetic field and is independent of having a barrier potential. The spin direction oscillates in the y-z-plane with the Larmor-frequency $\omega = -\tilde{\gamma}B$, so after the length of the barrier region has been crossed, the spin will more likely have the original direction or the opposite one, depending on B.

As was noted in section 3.2, the SOI term can be seen as an effective magnetic field, and in case of $\alpha_z \neq 0, \alpha_y = 0$ this effective field points in the y-direction and is also perpendicular to the spin-quantization direction z. Hence it also causes a Larmor precession, as can be seen in the bottom row of figure 3.6 in the left plot where the spin-changing conductance rises and finally the middle picture where the effective SOI magnetic field nearly only allows spin-changing conductance through the central region. The final plot in 3.6 shows how one of the conductance curves from figure 3.4 (bottom right plot) with both external magnetic field and SOI is resolved into its spin components. At the conductance step the lower band edge crosses the chemical potential, and as we have seen in figure 3.2 (F) the combination of perpendicular external magnetic field and SOI effect has a major influence on the shape of the lower band edge, explaining why a complicated structure appears in our spin resolved conductance plot.

These matters are further inspected in [Goulko et al., 2014] where additionally the interactions of electrons are taken into account with the functional renormalization group method that ultimately gives an additional self-energy matrix to include in the Green's function calculation.

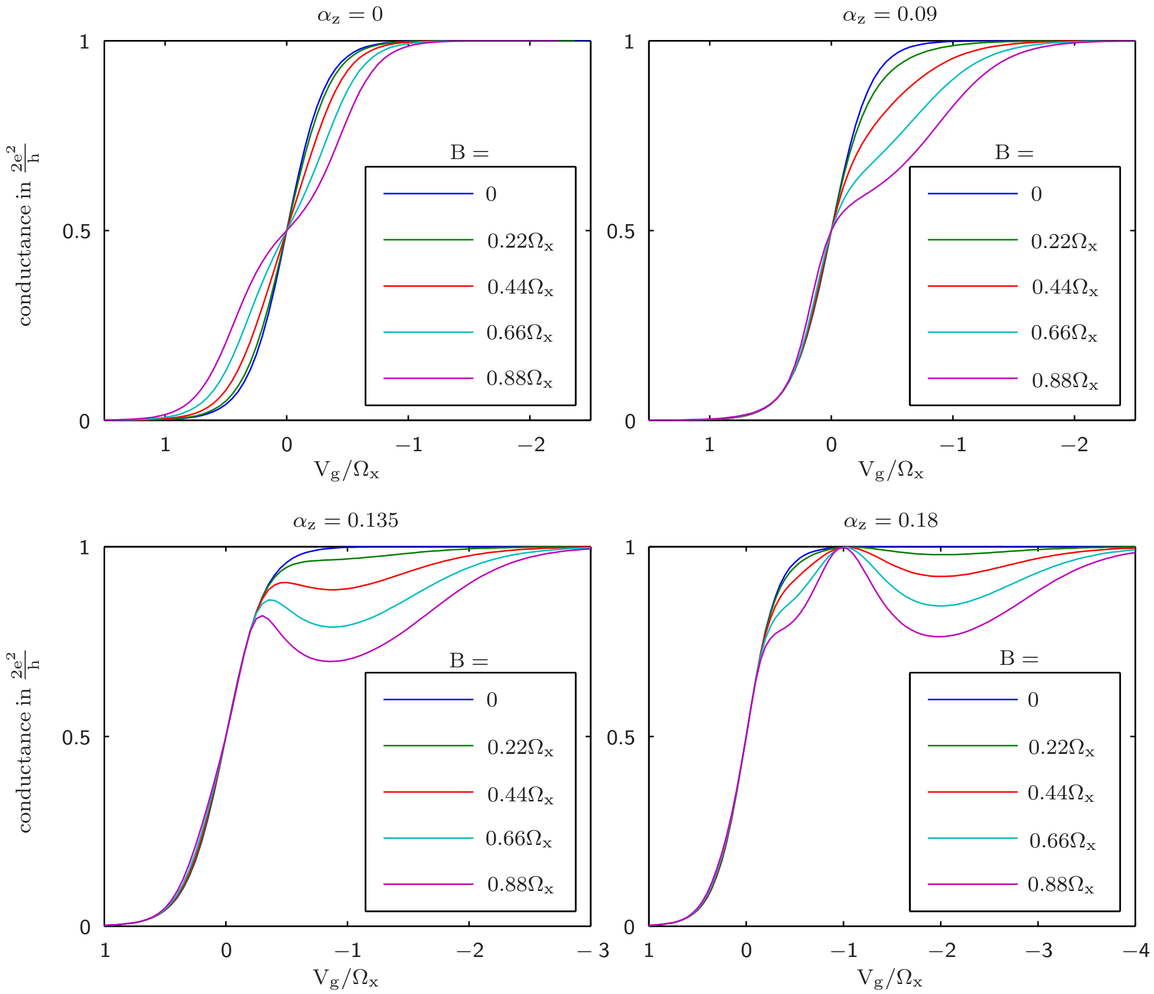

Figure 3.4: The conductance step as the potential barrier (width $d = 500$ sites, unperturbed height $f = 2.0$) gets shifted below the chemical potential. Each of the 4 diagrams has a different but fixed SOI strength α_z, the colored graphs represent the varying magnetic field values. $\Omega_x = 0.0113$.

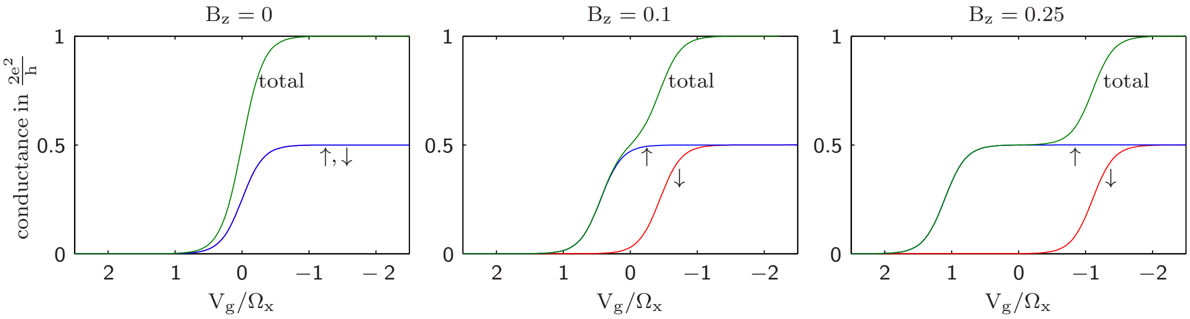

Figure 3.5: Spin resolved conductance (barrier width $d = 500$, $f = 2.0$) with magnetic field in z-direction for varying strength of magnetic field show the onset of the additional conductance step at $0.5\frac{2e^2}{h}$. Here ↑ (↓) stands for the spin-up to spin-up (spin-down to spin-down) conductance, while both spin-changing conductance contributions are constant 0 and not shown. $\Omega_x = 0.0113$.

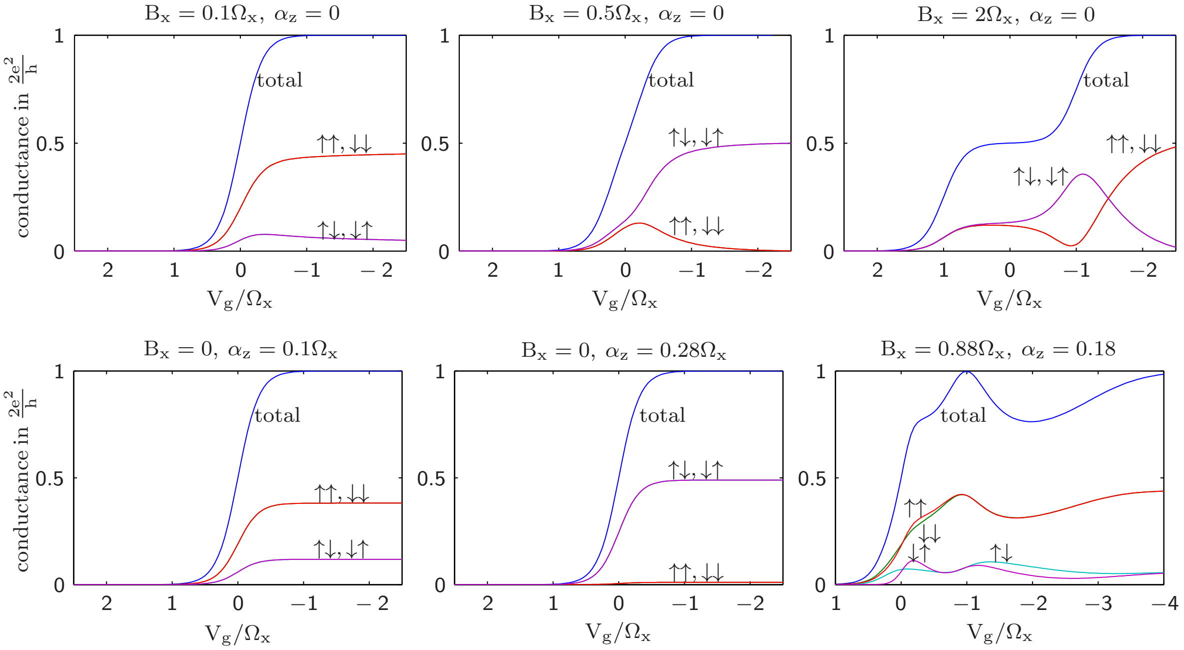

Figure 3.6: Spin resolved conductance through a QPC (barrier width $d = 500$, $f = 2.0$) with an increasing external magnetic field in x-direction (top row), with growing SOI (second row, first and second diagram) and with both effects active (bottom right). The conductance is plotted over the barrier height variation V_g with the blue graph for the total conductance as was seen it figure 3.4 and the four spin resolved conductance curves labeled with ↑↑ for spin-up to spin-up conductance etc.. $\Omega_x = 0.0113$.

3.5 Efficient Calculation of the Diagonal Entries of the Green's Function

The systems we consider in this thesis consist of a central region of N sites connected to two infinite leads, which can be conveniently traced out to just give a self-energy correction as described in section 2.4. So calculating the Green's function by formula 2.21

$$G(\omega) = \frac{1}{\omega - H - \Sigma + i\epsilon} = ((\omega + i\epsilon)\mathbb{1} - H - \Sigma)^{-1} \tag{3.18}$$

comes down to inverting a slightly modified Hamiltonian matrix H. For the most simple wire (2.9) H is a NxN matrix. Adding either superconductivity (chapter 5) or Spins (section 3.1) to the system required a doubling of the Hamiltonian matrix to account for either the superconducting term (see later chapter) or the different spin species, making H a $2N$x$2N$ matrix up to $4N$x$4N$ if both is considered at once. This matrix has to be inverted once for every energy parameter for which the Green's function is needed, for example for the local density of state diagrams like figure 2.6. On a modern computer this is still doable reasonably fast, even up to a few hundred or a thousand sites. But this step still takes by far the longest of the calculations presented here, so the considerably faster optimization presented in the following is useful.

We began with an infinitely big system that has been made finite by tracing out the two infinite leads, leaving only the central region of N sites which determines the size of the matrix that has to be inverted. The idea is to systematically interpret more and more sites as belonging to the leads and to repeatedly calculate new leads Green's functions of these growing leads until in the end there is only one single site left in the central region. Depending on spin or superconductivity in the system, a single site can be described by a matrix Hamiltonian of dimension 1x1 to at most 4x4 while all the information of the rest of the system is contained in the self-energy term coming from the new leads. Getting the Green's function now only needs the inversion of this one small matrix and the diagonal entries of the resulting 1x1 to 4x4 dimensional local Green's function matrix contains diagonal entries of the total Green's function of the central region that we are looking for. To get all the diagonal entries this has to be repeated for every site in the central region, but for a central region consisting of more than about 60 sites that is already faster than inverting the big Hamiltonian matrix just once. For about 300 sites it is faster by a factor of 10.

We write the Hamiltonian matrix in a basis which puts all entries belonging to one site together. Since there are no long range interactions considered, the resulting matrix will be a band matrix with the exact number of occupied bands depending on how often the Hamiltonian was doubled to account for superconductivity and spin.

$$H = \begin{pmatrix} H_{11} & H_{12} & 0 & 0 & \cdots \\ H_{21} & H_{22} & H_{23} & 0 & \cdots \\ 0 & H_{32} & H_{33} & H_{34} & \cdots \\ 0 & 0 & H_{43} & H_{44} & \cdots \\ \vdots & \vdots & \vdots & \vdots & \ddots \end{pmatrix} \tag{3.19}$$

Now we consider only the first site alone, described by H_{11}, and connect it only to the lead on the left. We can get the Green's function of this system from 3.18 to be

$$g_1^L(\omega) = \frac{1}{\omega - H_{11} - H_{10} g_L(\omega) H_{01}} \tag{3.20}$$

where g_L is the lead Green's function calculated in 2.18, H_{10} and H_{01} give the connection of site 1 to the leads and can be taken as $H_{10} = H_{21}$,$H_{01} = H_{12}$ since the first site of the central region is still the same as a lead site for a big enough central region. The self-energy term can be visualized as hopping to the lead, propagating by the Green's function at the border of the lead and hopping back to site 1. Now g_1^L can be interpreted as the Green's function at the border of a new lead that contains the site 1 as the last site.

This process can be iterated for all other sites in the central region to get

$$g_i^L(\omega) = \frac{1}{\omega - H_{ii} - H_{ii-1} g_{i-1}^L(\omega) H_{i-1i}} \tag{3.21}$$

and then repeated starting from the right side of the central region for the right lead by taking

$$g_i^R(\omega) = \frac{1}{\omega - H_{ii} - H_{ii+1} g_{i+1}^R(\omega) H_{i+1i}}. \tag{3.22}$$

With this intermediate result in our hands, the total Green's function at any of the sites is finally given by

$$G_{ii}(\omega) = \frac{1}{\omega - H_{ii} - H_{ii-1} g_{i-1}^L(\omega) H_{i-1i} - H_{ii+1} g_{i+1}^R(\omega) H_{i+1i}}. \tag{3.23}$$

and all the diagonal elements which are needed for the LDoS have been calculated only through inverting small matrices.

This procedure can be used even when next-nearest neighbor hopping is considered (which will come up in the following section 3.6). To avoid having H_{13} terms, we can put all the sites into groups of two and consider H_{11} as a matrix of double the dimensions, describing the first and second site. Then even the next nearest neighbor interactions are caught in the H_{12} matrices and the same ansatz as above can be used. Being limited to even numbers of sites in the central region is a small price to pay for the speed advantage.

3.6 Higher Order SOI

So far we have only considered SOI of the form

$$H_{SOI} = -\frac{e\hbar}{4m^2c^2} \sigma \cdot (E \times p) \tag{3.24}$$

which is just the first order of SOI, proportional to p. Higher order terms also exist but are usually neglected, for example in [Goulko et al., 2014] which was mostly followed in this chapter. To check that this is justified, let us have a brief look at the next highest order terms, which are $\propto p^3$, and see how strong they would have to be to make a considerable difference. The possible next highest order terms of the Spin-Orbit-Interaction are then given by

$$H_{SOI_3} = (\gamma_x \sigma_x p^3 + \gamma_y \sigma_y p^3 + \gamma_z \sigma_z p^3) \tag{3.25}$$

with three unknown coefficients $\gamma_{x/y/z}$. After discretizing the third derivative from the momentum operators, this can be expressed in the creation annihilation operator formulation and corresponds to

$$\begin{aligned} H_{SOI_3} =& \gamma_x \sum_{j=1}^{N} (ic^\dagger_{j\uparrow} c_{j+2\downarrow} - ic^\dagger_{j+2\uparrow} c_{j\downarrow} - 2ic^\dagger_{j\uparrow} c_{j+1\downarrow} + 2ic^\dagger_{j+1\uparrow} c_{j\downarrow} + \text{h.c.}) \\ &+ \gamma_y \sum_{j=1}^{N} (c^\dagger_{j\uparrow} c_{j+2\downarrow} - c^\dagger_{j+2\uparrow} c_{j\downarrow} - 2c^\dagger_{j\uparrow} c_{j+1\downarrow} + 2c^\dagger_{j+1\uparrow} c_{j\downarrow} + \text{h.c.}) \\ &+ \gamma_z \sum_{j=1}^{N} (ic^\dagger_{j\uparrow} c_{j+2\uparrow} - ic^\dagger_{j+2\uparrow} c_{j\uparrow} - 2ic^\dagger_{j\uparrow} c_{j+1\uparrow} + 2ic^\dagger_{j+1\uparrow} c_{j\uparrow} + \text{h.c.}). \end{aligned} \tag{3.26}$$

We are interested in how high the effect strengths $\gamma_x/\gamma_y/\gamma_z$ have to become before these terms make a difference in the total conductance of the system. It turns out that these terms do not change the total conductance of the system at all up to a critical value close to $\gamma_{x/y/z} = 0.5$, which is several times larger than a reasonable strength for the normal SOI term (see figure 3.4, the SOI has already a major effect around $\alpha_z \approx 0.2$). This can be seen in figure 3.7. The γ_x term (same for γ_y term, not shown) allows spin-flip hopping and have the effect of an effective magnetic field that lets the two kinds of conductance oscillate, even for small amplitudes of the higher order SOI term - but this does not influence the total conductance (top left of figure 3.7). The onset of a change in the total conductance happens very abruptly at much higher γ_x values between $\gamma_x = 0.49$ (top middle) and $\gamma_x = 0.50$ (top right). The γ_z term does not induce spin-flip conductance, but shows an equally late onset of an effect on the total conductance between $\gamma_z = 0.49$ (bottom left) and $\gamma_z = 0.50$ (bottom middle).

As we remember from earlier in this chapter, the lowest order SOI term did also not change the total conductance until an orthogonal magnetic field was turned on as well. To check if the higher order term has similar behavior, the bottom right plot of figure 3.7 shows the total conductance of a system with lower order SOI term $\alpha_z = 0.135$, external magnetic field $B_x = 0.05$ and three different values for γ_x. Again the total conductance remains unchanged by the higher order SOI, until the same critical value is crossed and a sudden shift appears.

In summary, the higher order terms can safely be ignored. To have a major effect on the total conductance, its prefactor has to be several times bigger than the lower order SOI prefactor, when in general one expects it to be smaller. But even if these terms would become important in some situations, they cause a sudden and drastic change in the total conductance instead of a subtle one, which would make their effect easy to recognize in measurements.

It becomes clearer what causes this sudden effect for high values of $\gamma_{x/y/z}$ when we look at the dispersion relation of the system. So take the Hamiltonian

$$H = \frac{p^2}{2m} - \mu + \alpha \cdot \sigma p + \gamma \cdot \sigma p^3 - B \cdot \sigma \tag{3.27}$$

and follow the steps before equation (2.7) in section 2.1. Diagonalizing finally gives the dispersion relation of the two spin-bands plotted in figure 3.8 for the example of $\alpha = 0$, $B = 0$, $\gamma_y = \gamma_z = 0$ and $\gamma_x \neq 0$ in the top and for a situation with external magnetic field ($B \neq 0$) and lower order SOI ($\alpha \neq 0$) present in the bottom. The shape of the dispersion near the minimum, which is the important point for the low energy excitations, does not change much through the third order term. But once γ_x reaches the amplitude for which the conductance abruptly changes ($\gamma_x \approx 0.5$), we see a new local minimum emerge in the dispersion relation, explaining a large change in the behavior of the system.

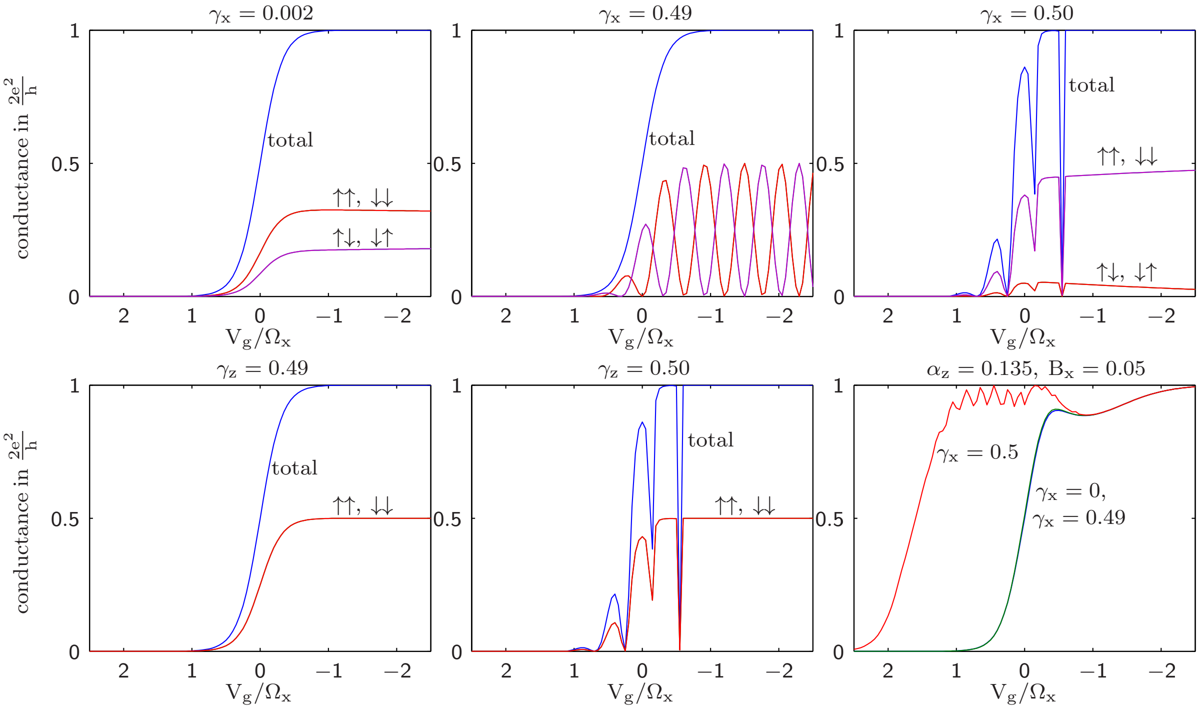

Figure 3.7: Effect of higher order SOI on conductance through a 500 site wide barrier, $f = 2.0$. Both for increasing γ_x (first row) and γ_z (bottom row, first and second diagram) with no first order SOI or external magnetic field present, the total conductance remains the same until a critical value close to 0.50 is reached. This even happens when both those effects are present and γ_x is increased above the critical value (bottom right). All three plots in the bottom right show the total conductance.

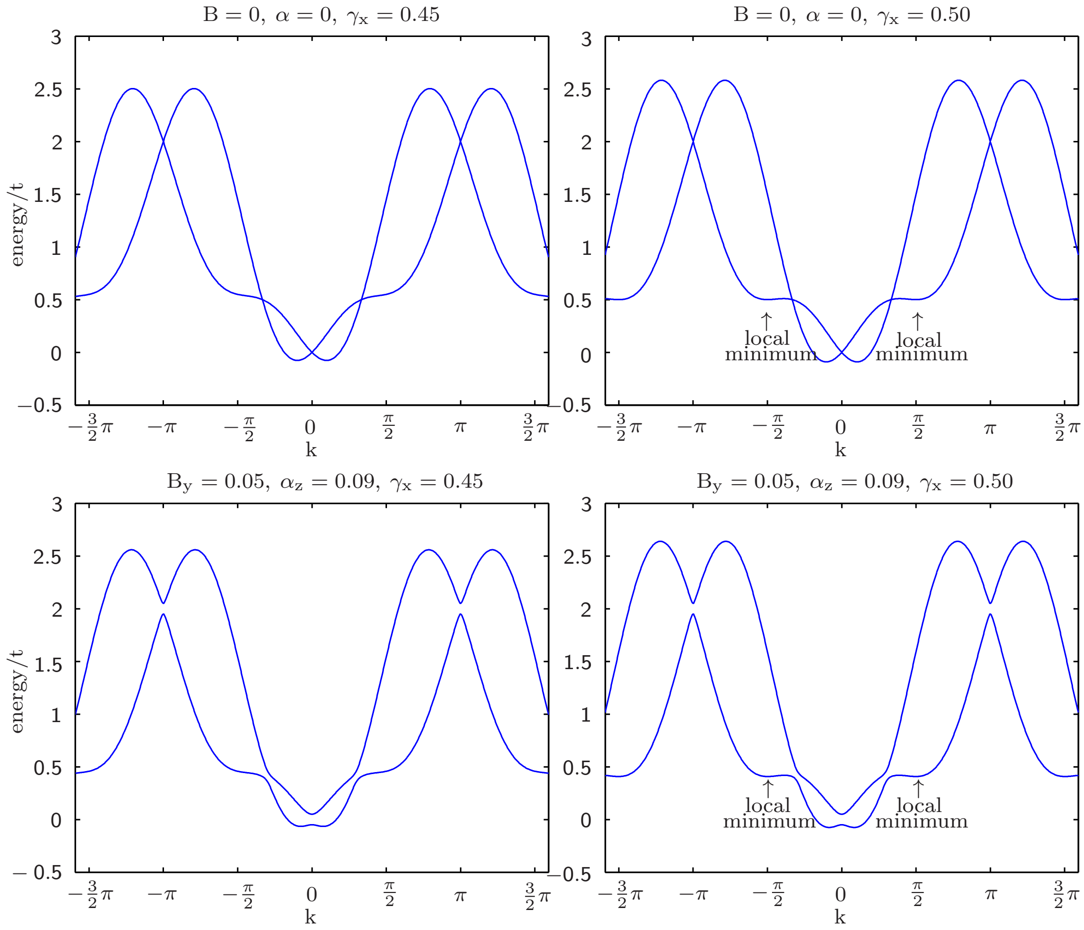

Figure 3.8: Dispersion relation of the wire with higher order spin-orbit-terms. Near $\gamma = 0.5$ a new local minimum appears.

Chapter 4

Majorana Fermions

So far we have introduced a rather basic model to describe wires and quantum point contact systems in general. Now that we have the theory, we are ready to approach the interesting (as will become clear in this chapter) appearance of the so called Majorana fermions (MFs). We will begin by giving the definition and having a brief look at their history as an introduction in section 4.1.

Despite their origin as an idea for fundamental particles, much later a possible realization in the form of quasi-particles in solid state systems was found. In section 4.2 we will look at the simplest model realizing these quasi-particles in one dimension, the so called Kitaev model named after Alexei Kitaev who first proposed the idea ([Kitaev, 2000]). As this is a one-dimensional lattice model it strongly resembles the model we have developed in the preceding chapters. The new ingredient is an unusual (since p-wave) superconducting term in the Hamiltonian. Including those into a Hamiltonian matrix formalism and deducing the Green's function will be the focus of chapter 5. Kitaev immediately points out the possible usage of such MFs as qubits in quantum computation, in particular because of their non-Abelian exchange statistics that we will briefly consider in chapter 6.3.

We will further see in section 4.3 that it is problematic to directly realize the Kitaev model in an experiment, as it has been conceived as a minimal example for the MFs to appear. Nevertheless, there has been some success in finding setups for more complicated systems that effectively behave like the simple wire with its unusual superconducting term that make up the Kitaev model, following an idea by [Fu and Kane, 2008] that allows using the much more common s-wave superconductors. Later in chapter 7 we will be able to qualitatively compare our results from the calculations with the Kitaev Model with the actual measurements done with devices build according to those setups.

Other realizations of Majorana fermions in solid state systems have been proposed and first experiments claim to have found signatures of those quasi-particles. There will be a brief overview over those approaches in section 4.4. For the remainder of this thesis we will stay with the Kitaev model though.

4.1 History of Majorana Fermions

The term Majorana fermion (MF) is used to denote a fermionic particle that is its own antiparticle. The idea first came up in the 1937 paper [Majorana, 1937] by Ettore Majorana, in which he proposed to describe neutral spin-1/2 fermions as a solution to a Dirac's equation modified in the following way ([Wilczek, 2009]).

The normal Dirac's equation for a four-component spinor reads

$$(i\gamma^\mu \partial_\mu - m)\Phi = 0 \tag{4.1}$$

with the γ matrices being complex 4x4 matrices fulfilling a Clifford algebra ([Dirac, 1928]) and $\mu \in \{0, 1, 2, 3\}$. Furthermore γ^0 must be Hermitian and the other three anti-Hermitian. The solutions to this equation are then also complex fields, which in quantum field theory have the meaning of creating a particle and destroying the corresponding antiparticle while the complex conjugate field does the opposite. A particle and antiparticle are identical if they are created by the same field, which clearly requires $\Phi = \Phi^*$. Majorana was able to find such real field solutions by making the equation completely real. To that end he found purely imaginary matrices $\tilde{\gamma}$ that still fulfill the Clifford algebra:

$$\tilde{\gamma}^0 = \sigma_y \otimes \sigma_x \qquad \tilde{\gamma}^1 = i\sigma_x \otimes \mathbb{1} \qquad \tilde{\gamma}^2 = i\sigma_z \otimes \mathbb{1} \qquad \tilde{\gamma}^3 = i\sigma_y \otimes \sigma_y. \tag{4.2}$$

We then have the Majorana equation

$$(i\tilde{\gamma}^\mu \partial_\mu - m)\Phi = 0 \tag{4.3}$$

having only real field solutions and hence describing particles that are their own antiparticles. Of course just from this equation it is not clear whether there actually exist any particles described by the Majorana equation.

Since antiparticles have the same mass but opposite charge compared to their counterpart, it is apparent that only neutral particles can come into consideration for being their own antiparticles. For bosons like photons this property is well known, but for fermions this concept was new and even today it is not settled whether any fermions actually have it. Majorana himself had neutrons and neutrinos in mind when he got his idea, for the former of which it was quickly disproven while the later at that time where themselves still unobserved theory. When measurements finally followed, his idea was again seen as disproven by anti-neutrinos behaving differently than neutrinos ([Cowan et al., 1956]) and the idea of Majorana fermions was forgotten for decades ([Wilczek, 2009]).

His idea became relevant again when weakening the constraint of lepton-conservation and predictions of unified field theories made neutrinos a possible Majorana fermion candidate again ([Wilczek, 2009]). Furthermore, supersymmetry introduced the idea of additional, more exotic Majorana fermions that might exist ([Weinberg, 2000]).

How is any of this relevant to solid state physics, which deals with lattices made of electrons and ions? So far we have talked about MFs in the context of high energy physics and fundamental particles, but solid state physics has its own particle zoo - in form of more or less exotic quasi-particles. It turns out that it is possible, but not trivial, to find theoretical models in which quasi-particles with the Majorana property of being their own antiparticle appear. One of the first such models is the one dimensional Kitaev model ([Kitaev, 2000]) found in 2000, which we will concentrate on and discuss in the following section. The new interest and quick development of further ideas to realize MF in solids was sparked not only by theoretical interest but also by a possible application that was pointed out by Kitaev: Such states could be used as particularly decoherence resistant qubits for quantum computers and furthermore show non-Abelian exchange statistics (see chapter 6.3) which could be used for quantum computations. A quantum computer following this concept is called topological quantum computer [Alicea, 2012].

Still, in the beginning his model was purely theoretical and it took more than a decade of further research to find promising experimental realizations. We will see the difficulties involved in that search in section 4.3, after some general properties of the Kitaev model have been introduced.

4.2 Kitaev Model

The Kitaev model, which was the first model realizing MF in a one dimensional lattice, is given by a Hamiltonian that mostly consists of the finite case of the wire Hamiltonian we used in the first chapter with the addition of a term that induces a superconducting gap Δ in the wire. In [Kitaev, 2000] it is presented as

$$H = -t \sum_{j=1}^{N-1} (c_j^\dagger c_{j+1} + \text{h.c.}) - \mu \sum_{j=1}^{N} c_j^\dagger c_j + \sum_{j=1}^{N-1} \left(\Delta c_j c_{j+1} + \Delta^* c_{j+1}^\dagger c_j^\dagger \right). \tag{4.4}$$

The new term at the end allows, at an energy cost Δ, the creation or annihilation of a pair of electrons on neighboring sites. We will need a more detailed look at the origin of this term in the following chapter 5 when we try to rewrite this expression as a matrix Hamiltonian, so we can proceed to calculate the LDoS and conductance from the Green's function with the tools developed in the previous chapter. For now, we can see that such a term makes sense as a description of the formation or destruction of Cooper pairs, which are not explicitly included as degrees of freedom. Since spins are not considered in the Kitaev model, the electron pairs have to live on neighboring sites instead of the same one to not break the Pauli exclusion principle. This connection of neighboring sites corresponds to a discretized derivative of a momentum operator and shows a momentum dependency in the superconducting term. So we know that we do not have the common s-wave superconductivity, which must be isotropic and hence independent of momentum. Instead, we have much rarer p-wave superconductivity.

In his original paper [Kitaev, 2000] Kitaev himself describes this model as a toy model. It picks the basic necessary ingredients to realize Majorana fermions, knowing that the result is not an accurate description of an arbitrary real wire. Providing an experimental setup for a wire or different system that would behave similar to this toy Hamiltonian is a challenge he leaves open.

But he offers some speculation on possible approaches, and both the possible use of Josephson junctions (section 4.4) and usage of an external magnetic field to break time reversal symmetry is already mentioned, the later of which is a key to the physical realizations in the recent experiments that claim to have build a setup that effectively behaves like this Kitaev model and contains MFs (see review [Alicea, 2012], experimental papers [Mourik et al., 2012] and [Das et al., 2012]).

Of course we want to understand how exactly the Majorana quasi-particles appear in the Kitaev model. This can be seen best after rewriting the Hamiltonian (4.4) in a slightly different way. We split the electron operators c_j into two half-fermions d_i that fulfill the Majorana condition $d_i = d_i^\dagger$ and can then recombine them differently to get other full fermions $\tilde{c}_j$:

$$\begin{aligned} c_j &= \frac{1}{2}(d_{2j} + id_{2j+1}) & \tilde{c}_j &= \frac{1}{2}(d_{2j} + id_{2j-1}) \\ c_j^\dagger &= \frac{1}{2}(d_{2j} - id_{2j+1}) & \tilde{c}_j^\dagger &= \frac{1}{2}(d_{2j} - id_{2j-1}). \end{aligned} \tag{4.5}$$

This replacement will be executed in more detail in chapter 6 in a bit more general case (see in particular figure 6.7), but for now we will be content with its result and its implications. For the qualitative picture, we simplify by taking the $t = |\Delta|$ case and end up with a Hamiltonian ([Kitaev, 2000, following (7)])

$$H = 2t \sum_{j=1}^{N-1} \left(\tilde{c}_j^\dagger \tilde{c}_j - \frac{1}{2} \right) \tag{4.6}$$

which remarkably does not include the first and last Majorana operators d_1 and d_{2N}. These two together can be thought of as an additional, non local fermionic state - a quasiparticle connecting the first with the last site. This leads to the system having two orthogonal ground states, one with the two unpaired Majorana fermions at the ends and one without. As shown in [Kitaev, 2000], for the case

$$|\mu| < 2t \tag{4.7}$$

which we will want to consider in the following, the ground state with MFs is realized. For this reason, the system is also called a topological superconductor with a topological phase $|\mu| < 2t$, which shows qualitatively different behavior from the trivial phase $|\mu| > 2t$ without Majorana fermions.

We have now understood how the Majorana state comes up and what is meant by it being non-local. Since our quasi-particle fermion is made up of half-fermion operators belonging to distant sites, and perturbation operators containing only a single Majorana fermion are not expected, a perturbation is unlikely to affect the Majorana state as it would have to act on both ends of the wire at once. This means quantum information stored in this state is particularly well protected, making them an interesting prospect for quantum memory. Together with the non-Abelian statistics (chapter 6) this might make quantum computation by moving and ultimately braiding such MF feasible ([Alicea, 2012], [Beenakker, 2012], [Leijnse and Flensberg, 2012]).

The next step will be to express the system in the formalism we have used so far to deduct the Green's function of the central region and the conductance through it. Including the superconducting term turns out to be more involved than the simple doubling that was necessary for the spin in chapter 3 and will take all of the following chapter 5.

The superconductivity has a major effect on the shape of the band and the conductance through it, both of which we will be visible in the LDoS and differential conductance plots respectively. Through the superconducting gap term Δ the electron band will acquire, as the name suggests, a gap in the density of states - an energy interval centered around a fixed chemical potential of the superconductor in which no conducting electron states can live as it would be energetically favorable to create a Cooper pair instead (compare figure 6.1). Hence a linear conductance, which happens solely around the chemical potential, is expected to quickly drop as the superconducting region gets too wide for electrons to tunnel through.

When we look at the differential conductance, which allows for a finite bias voltage and hence electrons away from the chemical potential of the superconductor, for certain setups with an additional potential barrier we can see an unexpected zero-bias peak appear in the conductance, i.e. an increased conductance through a region that at first glance should not contain electron states (left side of figure 7.3).

This is caused by the zero-energy Majorana state we have just found living at the ends of the wire. We will see these Majorana states in LDoS plots of isolated wires (figure 6.1) and we can see a clear exponential localization at the edges (figure 6.3). Attaching the leads again, the Majorana fermions on the ends of the superconducting region spread into the leads, making them invisible on LDoS plots. But after localizing one of them again with a potential barrier, these mid-gap state can then explain the zero-bias conductance peak we observed - a state living on both sides of the gap region enables conductance through it without tunneling.

It should be mentioned that while for an infinitely long wire we would indeed have zero-energy (relative to the chemical potential of the SC) states, these half-fermion states have a deviation from the chemical potential of the SC since there is a hybridization between them. This effect exponentially decays with the width of the superconducting region as their overlap gets small. It decays quickly enough that this is not a big concern for our results.

We will further see in chapter 6 that a potential barrier in the superconducting region causes the appearance of many more states inside the gap, most of which are different quasi-particle localized states that are not of Majorana type and that are not contributing to conductance. But as soon as the barrier crosses the chemical potential an additional pair of Majorana fermions appear at the intersections of the two. The reason becomes more clear when we think of the potential barrier as a as a shift of the chemical potential. Lifting it above the band width will break the condition 4.7 for a topological phase in a small region, creating two new phase transitions to trivial phase along the wire which also carry a MF each. This is a basic way to create and manipulate MFs simply by turning on gates along such a superconducting wire in topological phase.

4.3 Realizing a Kitaev Model in Experiment

Of course, getting from this toy model to an experimental setup that behaves according to this unusual superconducting term and allows the measurement and manipulation of Majorana fermions is another big hurdle. Let us examine where the difficulties arise. In the context of a solid state physics lattice, the antiparticle that belongs to an electron is a hole. So the basic idea is to realise a particle that is its own antiparticle as a superposition of electrons and holes.

Such particles are not completely new - they are already known in the context of superconductivity. There we have Cooper-pairs made up of a pair of electrons, which can be broken up into two Bogoliubov quasiparticles that are a superposition of electrons and holes with different spins and in general not equal prefactors. We can write the corresponding creation operator as $b^\dagger = a_1 c_\downarrow + a_2 c_\uparrow^\dagger$. To have a Majorana quasiparticle, this operator would have to be Hermitian, so we need prefactors that are complex conjugate to each other and have equal spin in both terms: $m = a c_\downarrow + a^* c_\downarrow^\dagger$. Such quasiparticles with same spins are not typical, they correspond to a Superconductors with p-wave pairing in 1D or $p_x \pm i p_y$ in 2D ([Leijnse and Flensberg, 2012]). Unfortunately, no elementary p-wave superconductor has been found yet. A theoretical candidate is given by Sr_2RuO_4 ([Sarma et al., 2006]), but the superconductivity seems to be too sensitive to impurities and has not been measured yet. So again, we have just shifted the problem to finding a p-wave superconductor.

The situation was saved when L. Fu and C. L. Kane published their discovery [Fu and Kane, 2008] that it was possible to achieve $p_x + i p_y$ pairing on the surface of 3D topological insulator when three key ingredients were brought together. They needed an s-wave superconductor that induces superconductivity by proximity effect, a strong spin orbit interaction in the topological insulator and on top of this a Zeeman splitting from a magnetic insulator to lift Kramers degeneracy ([Leijnse and Flensberg, 2012]). This approach was then further simplified by the realization that instead of a topological insulator, 2 dimensional semiconductors quantum wells could also be used ([Sau et al., 2010]), which then make it possible to use an external magnetic field for the Zeeman effect ([Alicea, 2010]). Finally, it turned out that all these ingredients could be applied to a one-dimensional semiconducting wire as well ([Oreg et al., 2010] and [Lutchyn et al.,]), bringing us back close to the Kitaev model.

Let us try to understand in the 1D case what each of these ingredients is necessary for (see also [Leijnse and Flensberg, 2012, Figure 5], [Das et al., 2012, Figure 1]). This can be best seen when considering the band structure $E(p_x)$ of the wire. In the most simple case with no additional terms (and without discretizing the model) it is given by the basic parabolic dispersion (figure 4.1 top left). Spin orbit interaction $\propto E \times p$ splits the two spin bands horizontally into two parabolas (figure 4.1 top right). Turning on a strong enough external magnetic field orthogonal to the spin-orbit effective magnetic field allows the two spin bands to interact and leads to avoided crossing at the intersection of both parabolas at $p = 0$ (figure 4.1 bottom left). Now there is an energy interval for the chemical potential for which only the lower band is filled so only a single spin direction is left, that unfortunately still depends on momentum. Using a stronger external field, the lower band will polarize more along one direction and increasing the width of the energy interval in which spin-degeneracy is broken.

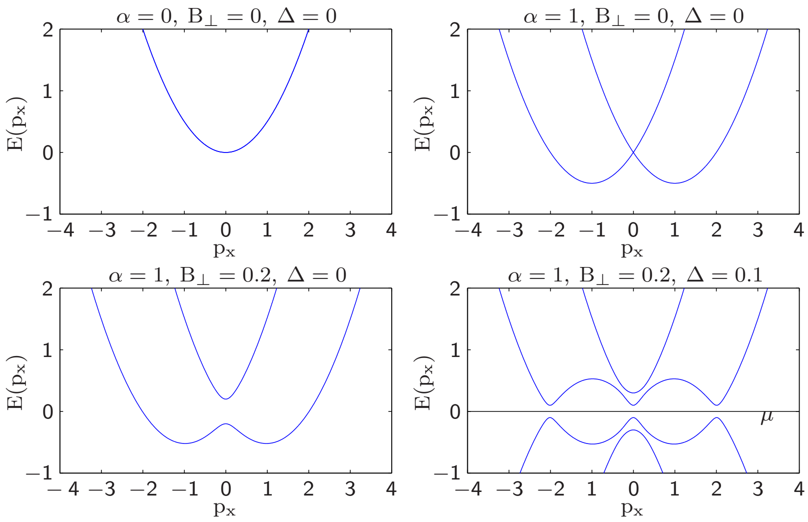

Figure 4.1: Dispersion relation of the wire with SOI strength α, external magnetic field $B_\perp$ orthogonal to the SOI direction and a superconducting gap Δ.

Now the chemical potential has to be tuned to lie exactly in this energy interval. We want to use an s-wave superconductor to proximity induce spinless superconductivity in our wire. While the stronger external magnetic field makes it easier to tune the chemical potential to a bigger spinless regime, the stronger alignment of electrons in the lower band make the proximity effect coupling weaker (see [Alicea, 2012], proximity effect of an s-wave superconductor couples to opposite spin electron pairs) and external field is further limited by the critical field strength of the s-wave superconductor - all together making delicate tuning necessary.

Due to the particle-hole symmetry, there are additional hole bands with a flipped sign of the energies, corresponding to the electron bands mirrored along the x-axis. A superconducting term allows both types to interact and again leads to avoided crossing, now creating a completely gapped system (figure 4.1 bottom right). The gaps away from $p = 0$ are governed by the Δ amplitude of the induced superconductivity, while the gap at $p = 0$ depends on both the external magnetic field B and Δ and differentiates between the two phases of the topological superconductor in the following way: For small $\Delta < \sqrt{|B|^2 - \mu^2}$ the superconductor is in the desired topological phase including the Majorana bound states at the domain walls to the trivial phase (which can be just given by the end of the wire if no other phases are present). With increasing Δ the gap at $p = 0$ shrinks again until it is fully closed at $\Delta = \sqrt{|B|^2 - \mu^2}$. With $\Delta > \sqrt{|B|^2 - \mu^2}$ the system is in a trivial superconducting phase that does not contain Majorana fermions.

These step-by-step instructions of building a 1D topological superconductor did not make their realization trivial, but at least feasible. In 2012 the first experimental papers have been published that claim to have realized and measured MFs with the approach described above in

[Mourik et al., 2012], [Das et al., 2012] and [Deng et al., 2012]. We will have a more detailed look at the first two of those in chapter 7 and compare their results with our predictions made from the Kitaev model. To detect the Majorana fermions, the prediction of an increased differential conductance around zero-bias voltage due to the Majorana mid-gap states was checked - and indeed such a zero-bias peak was found.

4.4 Other Proposed Realizations of Majorana Fermions

Although this paper solely focuses on the realization of Majorana fermions in one dimensional systems according to the Kitaev model, there have been many other theoretical proposals and even some experiments to realize MFs in solid state physics ([Leijnse and Flensberg, 2012]). The following can be seen as a brief and certainly not complete overview over some of those approaches.

The first one to mention should be [Deng et al., 2012], which does use the same one dimensional wire approach as above, but realizes a Josephson junction with two separate topological superconducting regions instead of only one region next to a quantum point contact as the two papers we will have a closer look at. Again a zero-bias peak is detected and explained by bound Majorana states. In principle our model, extended to superconducting systems in the next chapter, should be able to describe this situation as well, but we will concentrate on the situation of the former mentioned two papers.

The alternative proposition to probe Majorana fermions in Josephson junctions was already made in [Kitaev, 2000]. Some unusual characteristics compared to a conventional Josephson junction were predicted, among others the change from $2e$ to e as the unit of conductance, as now pairs of Majorana fermions could allow single electron conductance instead of just cooper pair conductance. Such a change of the conductance unit was measured in [Rokhinson et al., 2012] and further predicted transport properties have been measured in [Williams et al., 2012]. Both of these papers explain their results with the presence of Majorana modes in their devices.

Another way to get 1D systems is the idea to use edges of 2D topological insulators, which the already mentioned important papers by Fu and Kane ([Fu and Kane, 2008] and [Fu and Kane, 2009]) belongs to. Despite being called insulators, these materials have conducting edge states with the special property of being spin filtered depending on their direction. Adding an s-wave superconductor will again lead to a topological superconductor (see [Alicea, 2012]). In a similar way, the surface of 3D topological insulators can be used to get vortices with the Majorana property.

Further proposals include usage of cold atomic gases ([Tewari et al., 2007]), carbon nanotubes ([Egger and Flensberg, 2012]) and chains of quantum dots ([Sau and Sarma, 2012]) - all of which we will not further concern ourselves with. A very extensive list with further references can be found in the detailed review by Alicea [Alicea, 2012].

Chapter 5

Modeling Superconducting Systems

After the Majorana Fermions were introduced in the last chapter, we now want to find a model that allows us to calculate some basic transport properties of systems with these special quasi-particles. The simplest model that allows for this is the Kitaev Model introduced in section 4.2, but going further than his original paper [Kitaev, 2000], we want to be able to numerically visualize the local density of states and calculate the differential conductance of systems with both superconducting and normal conducting regions as well as potential barriers (quantum point contacts). To achieve this, we have to generalize our wire model from the first chapter by adding the superconducting terms from the Kitaev model of the form

$$\mathbf{H}_{SC} = \sum_{j=1}^{N-1} \left(\Delta c_j c_{j+1} + \Delta^* c_{j+1}^\dagger c_j^\dagger \right) \tag{5.1}$$

to the Hamiltonian. The general idea will be to use the so called 'doubling trick', according to which we introduce Nambu-spinors that allow us to write the Hamiltonian as a matrix with twice the dimensions. As a result, the terms with two creation or annihilation operators can be seen as an interaction of the two sectors from the doubling.

Note that we are back to a spin-free system as opposed to the third chapter where a spin-full model was introduced. While the experimental setups work with spin-full systems using strong spin-orbit-interaction, Zeeman splitting due to external magnetic fields and conventional s-wave superconductors, they tune all those ingredients in such a way that the system effectively behaves like the Kitaev model. For that reason, we will be content with following the rather simple Kitaev model, which considers a (in reality rather rare) p-wave superconductor populated by electrons of only a single spin-species.

5.1 The Generating Functional for the System

All the information we want to get about the system in the end, i.e. local density of states and linear as well as differential conductance, is contained in the Green's function of the system. The naive

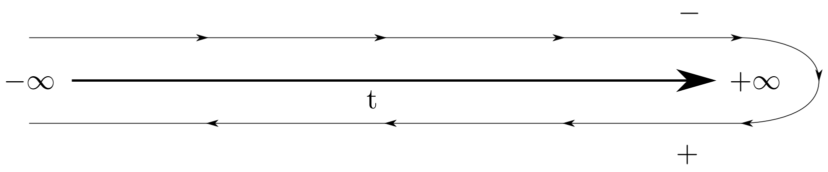

Figure 5.1: In our convention for the Keldysh contour the upper contour is denoted as − and the lower one as +.

way to proceed would be to try to double the Hamiltonian from the second chapter (2.5 and 2.13) and continue in a similar way. It turns out that there are subtle problems with this approach, in particular with how exactly to add in the self-energy from the integrated out leads in the correct way in a doubled Hamiltonian and how to deal with the chemical potentials when describing differential conductance where each lead has its own chemical potential.

Instead we will use the more general Keldysh formalism [Keldysh, 1965] of quantum field theory to be able to describe differential conductance. An introduction into the Keldysh formalism can be found in the book [Kamenev, 2001] and a detailed introduction to using it to describe 1D wires can be found in [Jakobs, 2009]. Some basic knowledge about the method will be assumed in the following.

Of the several different conventions that are used for the Keldysh formalism, this text will utilize the following ones from [Jakobs, 2009]. The Green's function will be defined in terms of the correlators as $G(t,t')^{ab}{}_{ij} = (-i)\langle T_c \; c^{a}{}_{i}(t) c^{\dagger b}{}_{j}(t')\rangle$ (the indices are explained in the following paragraph) and the Keldysh contours are indexed as seen in figure 5.1 with the upper one being the $-$ contour and the lower one $+$.

We begin by writing down the generating functional from which all desired correlators of the system, in particular the Green's functions, can be deduced.

$$\begin{aligned}
Z[J] = \int \mathcal{D}\{c\} \exp \Bigg[i \sum_{a} \int_{-\infty}^{\infty} \mathrm{d}\omega \, (-a) \Big(& c_i^{\dagger a}(\mu_s+\omega)(\mu_s+\omega+\epsilon_i)c_i^{a}(\mu_s+\omega) \\
& + t\, c_i^{\dagger a}(\mu_s+\omega)c_{i+1}^{a}(\mu_s+\omega) + t^* \, c_{i+1}^{\dagger a}(\mu_s+\omega)c_i^{a}(\mu_s+\omega) \\
& + \Delta\, c_{i+1}^{a}(\mu_s+\omega)c_i^{a}(\mu_s-\omega) + \Delta^* c_i^{\dagger a}(\mu_s-\omega)c_{i+1}^{\dagger a}(\mu_s+\omega) \\
& + J_i^{\dagger a}(\mu_s+\omega)c_i^{a}(\mu_s+\omega) + c_i^{\dagger a}(\mu_s+\omega)J_i^{a}(\mu_s+\omega) \\
& - c_i^{\dagger a}(\mu_s+\omega)\Sigma^{ab}{}_{ij}(\mu_s+\omega)c_j^{b}(\mu_s+\omega) \Big) \Bigg].
\end{aligned} \tag{5.2}$$

First a few notes about notation. The indices $a, b = \{+, -\}$ are used to denote Keldysh contours and the indices i, j are site indices along the wire, going from 1 to N since the infinite leads have been summed out and their effect on the system is now represented by a self-energy term Σ.

After the rotation to Keldysh space, the contour indices will be replaced by Keldysh components $\alpha, \beta = \{1, 2\}$ with 1 being the quantum component and 2 the classical component. A summation over all appearing double indices of these kinds is implied, even if not written explicitly. A Keldysh index $\bar{\alpha}$ takes the value that α does not have.

The c and $c^\dagger$ are again the creation and annihilation operators for single electrons at a site i. The term ϵ_i is the site dependent potential barrier to model a QPC. The one energy ω which is a summand instead of an argument in the first line comes from the action S of the system being written as $S = \int \mathrm{d}\omega(\omega - H(\omega))$ in energy representation and the $(-a)$ in the first line corresponds to the lower Keldysh contour going from $+\infty$ to $-\infty$, so the energy integral gets a sign from the integration limits being the wrong way around.

This leaves the energy constant μ_s and the gap term Δ coming from the Kitaev model superconducting term (5.1) to be explained. The first thing to note here is that the superconducting gap Δ itself is not written with an explicit Keldysh index unlike most other terms. Instead, they are assumed to have the same Keldysh structure as the hopping amplitude t, an approximation that is introduced in detail in [Larkin and Ovchinnikov, 1977]. It is assumed that the superconducting term in the Kitaev model is induced into the wire by proximity effect from a nearby bulk superconductor. The main approximation is that the thermodynamic properties (chemical potential μ_s and temperature) of this bulk superconductor are independent of the thermodynamic properties of the wire. Instead, the superconductor can only change the density of states in the wire by creating a gap inside the band around the energy μ_s, which is therefore not treated as a chemical potential in the Keldysh formalism, but as a fixed independent energy instead.

Expressing all the energies ω relative to this energy μ_s shows an important subtlety that easily leads to mistakes: Some of the operators in the superconducting terms in the third line of (5.2) need to have arguments $\mu_s - \omega$. To understand the origin of this peculiarity we again have to look back at where the superconducting term in the Kitaev model is taken from. While more detail is given in [Larkin and Ovchinnikov, 1977], as a simplified model we can say that a superconductor in the description of the BCS theory originates from an attractive force between electrons. This interaction can then be treated with a mean-field approach to get back to a Gaussian theory.

$$H_{att} = V_{\omega_1\omega_2\omega_3\omega_4} c^\dagger_{\omega_1} c^\dagger_{\omega_2} c_{\omega_3} c_{\omega_4} \approx \underbrace{0.5 V_{\omega_{1-4}} \langle c_{\omega_3} c_{\omega_4} \rangle}_{\Delta} c^\dagger_{\omega_1} c^\dagger_{\omega_2} + \underbrace{0.5 V_{\omega_{1-4}} \langle c^\dagger_{\omega_1} c^\dagger_{\omega_2} \rangle}_{\Delta^*} c_{\omega_3} c_{\omega_4} \tag{5.3}$$

Since this is an interaction of electrons in a metal at reasonably low temperatures, all the electrons can be assumed to have energies close to the chemical potential μ_s, so both the ingoing and the outgoing electrons add up to an energy of about $2\mu_s$.

$$\omega_1 + \omega_2 \approx \omega_3 + \omega_4 \approx 2\mu_s \tag{5.4}$$

Giving one of the energy arguments in the superconducting term in (5.2) an additional sign in front of the ω now assures that the energies properly add up to $2\mu_s$, even for big ω, which would otherwise not be the case.

Normally the effect of the chemical potential in the Keldysh formalism for a free theory is encoded in the Keldysh component alone. The μ_s can only appear in the way it does since we do not treat it as a normal chemical potential and it instead results from the approximation described above.

5.2 Calculating the Green's Function

Now that the origin of (5.2) has been explained, we have to proceed by performing the Keldysh rotation and changing into the doubled spinor basis, such that the exponent of the generating functional acquires a matrix structure. At that point the Gaussian integral can be calculated and we can then proceed to take the derivatives with respect to the Grassmann variables J to gain the Green's functions.

So let us now perform the Keldysh rotation. Most terms in (5.2) (all except the self-energy) live solely on either the upper or the lower contour, no mixing occurs. For the moment let T stand for any such term, then it is $T^{++} = -T^{--} =: T$, so writing this as a matrix in contour space we get

$$\begin{pmatrix} T^{++} & 0 \\ 0 & T^{--} \end{pmatrix} = \begin{pmatrix} T & 0 \\ 0 & -T \end{pmatrix}. \tag{5.5}$$

We can get from the contour space to Keldysh space with the rotation [Keldysh, 1965]

$$R = \frac{1}{\sqrt{2}} \begin{pmatrix} 1 & 1 \\ -1 & 1 \end{pmatrix} \tag{5.6}$$

so that

$$\begin{pmatrix} 0 & T^{12} \\ T^{21} & T^{22} \end{pmatrix} = R^{-1} \begin{pmatrix} T^{++} & 0 \\ 0 & T^{--} \end{pmatrix} R = \frac{1}{2} \begin{pmatrix} 0 & 2T \\ 2T & 0 \end{pmatrix} = T \underbrace{\begin{pmatrix} 0 & 1 \\ 1 & 0 \end{pmatrix}}_{A}. \tag{5.7}$$

Then we can write the generating functional in Keldysh space as

$$\begin{aligned} Z[J] = \int \mathcal{D}\{c\} \exp \Bigg[i \int_0^\infty \mathrm{d}\omega \, \Big(& c_i^{\dagger\,\alpha}(\mu_s + \omega)(\mu_s + \omega + \epsilon_i) A^{\alpha\beta} c_i^{\beta}(\mu_s + \omega) \\ & + t\, c_i^{\dagger\,\alpha}(\mu_s + \omega) A^{\alpha\beta} c_{i+1}^{\beta}(\mu_s + \omega) + t^*\, c_{i+1}^{\dagger\,\alpha}(\mu_s + \omega) A^{\alpha\beta} c_i^{\beta}(\mu_s + \omega) \\ & + \Delta\, c_{i+1}^{\alpha}(\mu_s + \omega) A^{\alpha\beta} c_i^{\beta}(\mu_s - \omega) + \Delta^* c_i^{\dagger\,\alpha}(\mu_s - \omega) A^{\alpha\beta} c_{i+1}^{\dagger\,\beta}(\mu_s + \omega) \\ & + J_i^{\dagger\,\alpha}(\mu_s + \omega) A^{\alpha\beta} c_i^{\beta}(\mu_s + \omega) + c_i^{\dagger\,\alpha}(\mu_s + \omega) A^{\alpha\beta} J_i^{\beta}(\mu_s + \omega) \\ & - c_i^{\dagger\,\alpha}(\mu_s + \omega) \Sigma^{\alpha\beta}{}_{ij}(\mu_s + \omega) c_j^{\beta}(\mu_s + \omega) + \{\omega \to -\omega\} \Big) \Bigg] \end{aligned} \tag{5.8}$$

where we have also put the lower integration limit to 0 at the cost of adding all the terms a second time with ω being replaced by $-\omega$.

It might seem that the self-energy Σ from the integrated out leads and especially its full Keldysh structure are still unknown at this point. But since the leads are Gaussian, the self-energy depends only on the leads and is independent of what happens in the central region, so at least its retarded component $\Sigma^R = \Sigma^{12}$ is given by the same formula that was determined earlier in (2.18).

$$\Sigma^{12}{}_{11} = \Sigma^{12}{}_{NN}(\omega) = t^2 g_L(\omega) = t^2 \begin{cases} \frac{1}{2t^2}(\omega + i\sqrt{4t^2-\omega^2}) & \text{if } \omega > 2t \\ \frac{1}{2t^2}(\omega - i\sqrt{4t^2-\omega^2}) & \text{else.} \end{cases} \tag{5.9}$$

Therefore also the advanced component is known to be $\Sigma^{21} = \Sigma^{\dagger\,12}$. In addition, the leads can be assumed to be in equilibrium (unlike the central region, which in the non-equilibrium Keldysh method does not need to be) so the fluctuation dissipation theorem gives the Keldysh component as $\Sigma^{11} = (1-2n_F)(\Sigma^{12} - \Sigma^{21})$. Hence the full structure of the self-energy matrix is known.

Let us now introduce Nambu-spinors depending on μ_s and defined strictly for non-negative energies ω to be

$$\Psi^{\alpha}{}_{i}(\omega) = \begin{pmatrix} c^{\alpha}{}_{i}(\mu_s+\omega) \\ c^{\dagger\alpha}{}_{i}(\mu_s-\omega) \end{pmatrix}, \Psi^{\dagger\alpha}{}_{i}(\omega) = \begin{pmatrix} c^{\dagger\alpha}{}_{i}(\mu_s+\omega), c^{\alpha}{}_{i}(\mu_s-\omega) \end{pmatrix}. \tag{5.10}$$

With this, we can exchange all the operators c in the generating functional by their corresponding Nambu-Spinor entry and then commute all the $\Psi^\dagger$ terms to the left side by using $\Psi^{\alpha}{}_{i}\Sigma^{\alpha\beta}{}_{ij}\Psi^{\dagger\beta}_{j} = -\Psi^{\dagger\beta}_{j}(\Sigma^T)^{\beta\alpha}{}_{ji}\Psi^{\alpha}{}_{i} = -\Psi^{\dagger\alpha}_{j}(\Sigma^T)^{\alpha\beta}{}_{ji}\Psi^{\beta}{}_{i}$, where the minus sign comes from the exchange of two fermionic operators and Σ^T is transposed both in Keldysh and in site space. As a result we get

$$\begin{aligned} Z[J] = \int \mathcal{D}\{\Psi\} \exp\Bigg[i\int_0^\infty \mathrm{d}\omega \Big(& \Psi^{\dagger\,1\alpha}{}_{i}(\omega)(\mu_s+\omega+\epsilon_i)A^{\alpha\beta}\Psi^{1\beta}{}_{i} - \Psi^{\dagger 2\alpha}{}_{i}(\omega)(\mu_s-\omega+\epsilon_i)A^{\alpha\beta}\Psi^{2\beta}{}_{i} \\ & + t\,\Psi^{\dagger 1\alpha}{}_{i}(\omega)A^{\alpha\beta}\Psi^{1\beta}{}_{i+1}(\omega) - t\,\Psi^{\dagger 2\alpha}{}_{i+1}(\omega)(A^T)^{\alpha\beta}\Psi^{2\beta}{}_{i}(\omega) + t^*\,\Psi^{\dagger 1\alpha}{}_{i+1}(\omega)A^{\alpha\beta}\Psi^{1\beta}{}_{i}(\omega) \\ & - t^*\,\Psi^{\dagger 2\alpha}{}_{i}(\omega)(A^T)^{\alpha\beta}\Psi^{2\beta}{}_{i+1}(\omega) - \Delta\Psi^{\dagger 2\alpha}{}_{i}(\omega)(A^T)^{\alpha\beta}\Psi^{1\beta}{}_{i+1}(\omega) + \Delta\Psi^{\dagger 2\alpha}{}_{i+1}(\omega)A^{\alpha\beta}\Psi^{1\beta}{}_{i}(\omega) \\ & - \Delta^*\Psi^{\dagger 1\alpha}{}_{i+1}(\omega)A^{\alpha\beta}\Psi^{2\beta}{}_{i+1}(\omega) + \Delta^*\Psi^{\dagger 1\alpha}{}_{i}(\omega)A^{\alpha\beta}\Psi^{2\beta}{}_{i}(\omega) \\ & - \Psi^{\dagger 1\alpha}{}_{i}(\omega)\Sigma^{\alpha\beta}{}_{ij}(\mu_s+\omega)\Psi^{1\beta}{}_{j}(\omega) + \Psi^{\dagger 2\alpha}{}_{i}(\omega)(\Sigma^T)^{\alpha\beta}{}_{ij}(\mu_s-\omega)\Psi^{2\beta}{}_{j}(\omega) \\ & + \bar{J}^{\alpha}_{i}(\mu_s+\omega)A^{\alpha\beta}\Psi^{1\beta}{}_{i}(\omega) - \Psi^{\dagger 2\alpha}{}_{i}(\omega)(A^T)^{\alpha\beta}\bar{J}^{\beta}_{i}(\mu_s-\omega) \\ & + \Psi^{\dagger 1\alpha}{}_{i}(\omega)A^{\alpha\beta}J^{\beta}_{i}(\mu_s+\omega) - J^{\alpha}_{i}(\mu_s-\omega)(A^T)^{\alpha\beta}\Psi^{2\beta}{}_{i}(\omega)\Big)\Bigg] \end{aligned} \tag{5.11}$$

with the indices 1,2 giving either the first of second entry of the Nambu-spinors. We can combine the summands into matrices in Nambu-space and get

$$
\begin{aligned}
Z[J] = \int \mathcal{D}\{\Psi\} \exp \Bigg[i \int_0^\infty \mathrm{d}\omega \, \Bigg(& \Psi^{\dagger\alpha}_{i}(\omega) \begin{pmatrix} (\omega + \mu_s + \epsilon_i) A^{\alpha\beta} & 0 \\ 0 & (\omega - \mu_s - \epsilon_i) A^{\alpha\beta} \end{pmatrix} \Psi^{\beta}{}_{i}(\omega) \\
& + \left(\Psi^{\dagger 1\alpha}{}_{i}, \Psi^{\dagger 1\alpha}{}_{i+1}, \Psi^{\dagger 2\alpha}{}_{i}, \Psi^{\dagger 2\alpha}{}_{i+1} \right)(\omega) \begin{pmatrix} 0 & tA^{\alpha\beta} & 0 & \Delta^* A^{\alpha\beta} \\ t^* A^{\alpha\beta} & 0 & -\Delta^* A^{\alpha\beta} & 0 \\ 0 & -\Delta A^{\alpha\beta} & 0 & -t^* A^{\alpha\beta} \\ \Delta A^{\alpha\beta} & 0 & -tA^{\alpha\beta} & 0 \end{pmatrix} \begin{pmatrix} \Psi^{1\beta}{}_{i} \\ \Psi^{1\beta}{}_{i+1} \\ \Psi^{2\beta}{}_{i} \\ \Psi^{2\beta}{}_{i+1} \end{pmatrix} (\omega) \\
& - \Psi^{\dagger\alpha}_{i}(\omega) \begin{pmatrix} \Sigma^{\alpha\beta}{}_{ij}(\mu_s + \omega) & 0 \\ 0 & -(\Sigma^T)^{\alpha\beta}{}_{ij}(\mu_s - \omega) \end{pmatrix} \Psi^{\beta}{}_{j}(\omega) + \{\text{terms with } J\} \Bigg) \Bigg]
\end{aligned} \tag{5.12}
$$

$$
= \int \mathcal{D}\{\Psi\} \exp \left[i \int_0^\infty \mathrm{d}\omega \left(\Psi^{\dagger\alpha} X^{\alpha\beta} \Psi^{\beta} + \{\text{terms with } J\} \right) \right] \tag{5.13}
$$

where we have used that $A = A^T$. In the last line

$$
\Psi^{\dagger\alpha} = \left(\Psi^{\dagger 1\alpha}{}_{1}, \Psi^{\dagger 1\alpha}{}_{2}, ..., \Psi^{\dagger 1\alpha}{}_{N}, \Psi^{\dagger 2\alpha}{}_{1}, \Psi^{\dagger 2\alpha}{}_{2}, ..., \Psi^{\dagger 2\alpha}{}_{N} \right)
$$

and X is the corresponding matrix with all the entries seen in (5.12). Note that X is a matrix in site space, in Keldysh space and also in Nambu space.

Since this is a Gaussian Integral it can be solved and we have already brought it into a shape where the solution can be read off using the general solution ([Kamenev, 2001, chap. 9.1])

$$
\tilde{Z}[\bar{J}, J] = \int \prod_{j=1}^{N} (\mathrm{d}\Psi^\dagger_j \mathrm{d}\Psi_j) \, \mathrm{e}^{-\Psi^\dagger_i X_{ij} \Psi_j + \Psi^\dagger_j J_j + \bar{J}_j \Psi_j} = \det X \, \mathrm{e}^{\bar{J}_i (X^{-1})_{ij} J_j}. \tag{5.14}
$$

With the $\det X$ being canceled by adjusting the integration measure $\mathcal{D}\{\Psi\}$ we therefore have

$$
\begin{aligned}
Z[J] &= \exp \left[-i \int_0^\infty \mathrm{d}\omega \left(\bar{J}_i{}^{\alpha}(\mu_s + \omega), -J_i{}^{\alpha}(\mu_s - \omega) \right) A^{\alpha\beta} (X^{-1})^{\beta\gamma}_{ij} A^{\gamma\delta} \begin{pmatrix} J^{\delta}{}_{j}(\mu_s + \omega) \\ -\bar{J}^{\delta}{}_{j}(\mu_s - \omega) \end{pmatrix} \right] \\
&= \exp \left[-i \int_0^\infty \mathrm{d}\omega \left(\bar{J}_i{}^{\alpha}(\mu_s + \omega), -J_i{}^{\alpha}(\mu_s - \omega) \right) (X^{-1})^{\bar{\alpha}\bar{\beta}}_{ij} \begin{pmatrix} J^{\beta}{}_{j}(\mu_s + \omega) \\ -\bar{J}^{\beta}{}_{j}(\mu_s - \omega) \end{pmatrix} \right]
\end{aligned} \tag{5.15}
$$

where the A matrices come from the the J-terms, see (5.11). The prefactor $-i$ comes from the following consideration. To bring (5.13) exactly into the form of (5.14), there is a factor i too much and the sign of the X matrix term is wrong. Since J and $\bar{J}$ are arbitrary Grassmann variables we can put $J, \bar{J} \to iJ, i\bar{J}$ and also put $X \to -iX$. The right side of (5.14) has an exponent of $\bar{J} X^{-1} J$ so all together this gives a prefactor of $\frac{i^2}{-i} = \frac{1}{i} = -i$.

At this point we can take the derivatives of the generating functional to finally calculate the Green's functions of the system. We have defined Nambu-spinors for strictly non-negative energies and have to differentiate differently depending on the sign of the energy for which the Green's function is determined. For positive energies $\omega > 0$ the Green's function is given by

$$G^{\alpha\beta}{}_{ij}(\omega > 0) = -i\langle c^{\alpha}{}_{i}(\mu_s + \omega) c^{\dagger\beta}{}_{j}(\mu_s + \omega)\rangle = -i\frac{\delta^2 Z[J]}{\delta \bar{J}^{\bar{\alpha}}{}_{i}(\mu_s + \omega)\delta J^{\bar{\beta}}{}_{j}(\mu_s + \omega)} \tag{5.16}$$

$$= -i\delta_{\bar{J}^{\bar{\alpha}}{}_{i+}}\delta_{J^{\bar{\beta}}{}_{j+}} \mathrm{e}^{-i\bar{J}^{\bar{\alpha}}{}_{i+}(X^{-1})^{\alpha\beta 11}_{ij} J^{\bar{\beta}}{}_{j+}} = -i\delta_{\bar{J}^{\bar{\alpha}}{}_{i+}}\delta_{J^{\bar{\beta}}{}_{j+}}(1 - i\bar{J}^{\bar{\alpha}}{}_{i+}(X^{-1})^{\alpha\beta 11}_{ij} J^{\bar{\beta}}{}_{j+})$$

$$= i(-i)\delta_{\bar{J}^{\bar{\alpha}}{}_{i+}}(\bar{J}^{\bar{\alpha}}{}_{i+}(X^{-1})^{\alpha\beta 11}_{ij}) = (X^{-1})^{\alpha\beta 11}_{ij}$$

where we have used the shorthand notation J_+ for $J(\mu_s + \omega)$ and made use of two properties of the Grassmann variables J. For the exponential function with Grassmann arguments it is $\exp(J) = 1 + J$ using the $J^2 = 0$ property and a minus sign in the last line was gained from anti-commuting the J and $\bar{J}$ since derivatives act on the leftmost Grassmann variable in our convention. Similarly the Green's function for negative energies $\omega < 0$ (with shorthand notation $J_- = J(\mu_s - |\omega|)$, absolute value since we considered strictly positive ω for the preceding calculation, but for $\omega < 0$ it is $+\omega = -|\omega|$) must then be given by

$$G^{\alpha\beta}{}_{ij}(\omega < 0) = -i\langle c^{\alpha}{}_{i}(\mu_s - |\omega|) c^{\dagger\beta}{}_{j}(\mu_s - |\omega|)\rangle = -i\delta_{\bar{J}^{\bar{\alpha}}{}_{i-}}\delta_{J^{\bar{\beta}}{}_{j-}}(1 - iJ^{\bar{\beta}}{}_{j-}(X^{-1})^{\beta\alpha 22}_{ji} J^{\bar{\alpha}}{}_{i-}) \tag{5.17}$$

$$= -i(-i)\delta_{\bar{J}^{\bar{\alpha}}{}_{i-}}(X^{-1})^{\beta\alpha 22}_{ji}\bar{J}^{\bar{\alpha}}{}_{i-} = -(X^{-1})^{\beta\alpha 22}_{ji},$$

so the difference is a relative sign and a transpose both in Keldysh and in site space.

To review the final result, the Green's functions can be directly gained from the matrix X in the following way. According to (5.12), the retarded component of X (for simplicity shown for the concrete example of a system with $N = 3$ sites) is given by

$$X^{21} = \begin{pmatrix} \omega_+ - \Sigma^{21}_{11}(\mu_s + |\omega|) & t & 0 & 0 & \Delta^* & 0 \\ t^* & \omega_+ & t & -\Delta^* & 0 & \Delta^* \\ 0 & t^* & \omega_+ - \Sigma^{21}_{33}(\mu_s + |\omega|) & 0 & -\Delta^* & 0 \\ 0 & -\Delta & 0 & \omega_- + \Sigma^{12}_{11}(\mu_s - |\omega|) & -t & 0 \\ \Delta & 0 & -\Delta & -t^* & \omega_- & -t \\ 0 & \Delta & 0 & 0 & -t & \omega_- + \Sigma^{12}_{33}(\mu_s - |\omega|) \end{pmatrix}$$

with the shorthand notation $\omega_+ = |\omega| + \mu_s + \epsilon_i$ and $\omega_- = |\omega| - \mu_s - \epsilon_i$. Then for positive energies from (5.16) we have

$$G^{21}{}_{ij}(\omega > 0) = (X^{-1})^{2111}_{ij}, \tag{5.18}$$

which means we have to invert the matrix X, then pick the 11 Nambu component which is the upper left NxN block of X for this example and can then pick the ij component of it.

For negative energies it is

$$G^{21}{}_{ij}(\omega < 0) = -(X^{-1})^{1222}_{ji} = -\overline{(X^{-1})}^{2122}_{ij}, \tag{5.19}$$

where we switched from the advanced Keldysh component of X^{-1} to the retarded one by using that the conjugate transpose of the advanced component equals the retarded one. This can be seen in (5.12); the only term that differs between retarded and advanced component is the self-energy term for which this is true. So in fact, we need to calculate the same inverse as for the positive energy case, take the complex conjugate and finally take the lower right NxN block of the matrix according to the Nambu indices 22 to pick element ij from.

Now that we have calculated the Green's function of a superconducting system with normal leads, the diagonal of the spectral function or local density of states (which are equivalent for lattice distance set to $a = 1$) $\rho_i(\omega)$ can be calculated as the imaginary part of the diagonal elements of the Green's function as in (2.12), which gives

$$\rho_i(\omega) = -\frac{1}{\pi}\mathrm{Im}(G^{21}{}_{ii}). \tag{5.20}$$

5.3 Derivation of the Conductance Formula

Next we are interested in the transport properties of the system, so we have to calculate the currents and from there can get to the conductance.

It is not at all clear that the formula (2.26) that was used for conductance in chapter 2 is still applicable in this case, in particular when we consider that the new additional superconducting term (5.1) explicitly breaks charge conservation by allowing electron pairs to be created or annihilated. This models the ground state of the superconductor which spontaneously breaks the charge conservation.

There must first be a non-equilibrium configuration, for example a voltage difference, for a current to appear in this physical system, so the current is an inherently non-equilibrium property of the system. Nevertheless, a lot of physics can be done in purely equilibrium considerations thanks to linear response theory and the Kubo-formula [Datta, 1995]. Linear response theory assumes that for small perturbations the system gives a linear answer - for our case this would be the linear conductance as an answer to an infinitesimal voltage. The Kubo-formula is then a tool that allows access to this non-equilibrium effect without leaving an equilibrium model and should work fine for our system.

We will again take the more general approach and use the non-equilibrium method of Keldysh formalism though, as this avoids having to use the Kubo-formula and gives us easy access to the differential conductance, which is the answer of the system to an infinitesimal voltage perturbation on top of a finite voltage difference. So we will now use the Keldysh formalism to calculate a current formula for our doubled system, following the derivation of the (Meir-Wingreen-)current formula for a non superconducting system [Meir and Wingreen, 1992].

Let us first recall the Hamiltonian of our considered system once more. All together it is given by

$$H = \sum_{i\in\{L,C,R\}} \epsilon_i\, c_i^\dagger c_i + \sum_{i\in\{L,C,R\}} (t c_i^\dagger c_{i+1} + t^* c_{i+1}^\dagger c_i) + \sum_{i\in\{C\}} \left[\Delta_i c_i c_{i+1} + \Delta_i^* c_{i+1}^\dagger c_i^\dagger\right]. \tag{5.21}$$

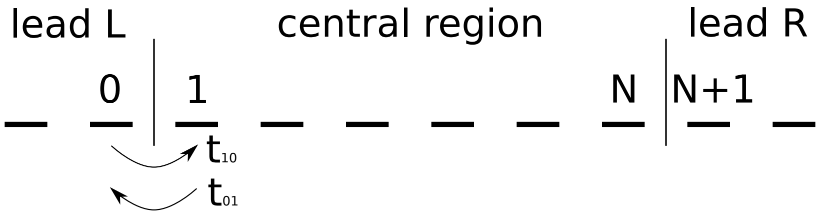

Figure 5.2: The two leads L and R are connected to the first and last site of the central region.

Note that the leads have not been projected out yet here so the first two sums include the lead but the superconducting term in the end only has support in the central region as we consider our leads to be normal metals.

We want to find an expression for the current that goes from the left lead to the right lead (see figure 5.2). This will be given by the change of the electron number in the left lead multiplied by the elemental charge e. So we have

$$J(t) = -e\langle \dot{n}_L(t)\rangle = -\frac{ie}{\hbar}\langle [H(t), n_L(t)]\rangle \tag{5.22}$$

where we have used the Heisenberg equation of motion which says that in the Heisenberg picture for a not explicitly time dependent operator n_L it is $\dot{n}_L(t) = \frac{i}{\hbar}[H(t), n_L(t)]$. Of course n_L is just the sum of the electrons on all the sites of the lead, so it is

$$n_L = \sum_{i\in\text{lead L}} c_i^\dagger c_i \tag{5.23}$$

and we have to recognize the terms in n_L and H for which their commutator does not disappear.

The first term in H consists of particle number operators on the sites just like n_L, so those terms clearly commute and do not contribute. The superconducting term in H only has support in the central region but all operators in n_L live in the left lead, so those terms commute as well. This only leaves the hopping terms in H to give a contribution. Let us first consider the terms for hopping to the left (see figure 5.2). Then it is

$$\begin{aligned}
&[\sum_{i\in\text{all}} t_{ii+1} c_i^\dagger c_{i+1}, \sum_{j\in L} c_j^\dagger c_j] = \sum_{\substack{i\in L\\ j\in\{i,i+1\}}} t_{ii+1}[c_i^\dagger c_{i+1}, c_j^\dagger c_j] + \sum_{\text{all other } i,j} t_{ii+1} \underbrace{[c_i^\dagger c_{i+1}, c_j^\dagger c_j]}_{=0\,\text{since}\, j\neq i,i+1} \\
&= \sum_{i\in L\setminus\{0\}} t_{ii+1}\Big(\underbrace{c_i^\dagger c_{i+1} c_i^\dagger c_i}_{=0} - c_i^\dagger \underbrace{c_i c_i^\dagger}_{1-c_i^\dagger c_i} c_{i+1} + c_i^\dagger \underbrace{c_{i+1} c_{i+1}^\dagger}_{1-c_{i+1}^\dagger c_{i+1}} c_{i+1} - \underbrace{c_{i+1}^\dagger c_{i+1} c_i^\dagger c_{i+1}}_{=0} \Big) \\
&+ t_{01}\Big(\underbrace{c_0^\dagger c_1 c_0^\dagger c_0}_{=0} - c_0^\dagger \underbrace{c_0 c_0^\dagger}_{1-c_0^\dagger c_0} c_1 \Big) = \sum_{i\in L\setminus\{0\}} t_{ii+1}(-c_i^\dagger c_{i+1} + c_i^\dagger c_{i+1}) - t_{01} c_0^\dagger c_1 \\
&= -t_{01} c_0^\dagger c_1.
\end{aligned} \tag{5.24}$$

The analogous calculation for the right hopping terms gives a similar result so that we can finally write the current as

$$J = -\frac{ie}{\hbar}\langle[H(t), n_L(t)]\rangle = -\frac{ie}{\hbar}\left(t^{--}{}_{01}\langle c^{-}{}_{1}(t)c^{\dagger+}{}_{0}(t)\rangle - t^{--}{}_{10}\langle c^{-}{}_{0}(t)c^{\dagger+}{}_{1}(t)\rangle\right). \tag{5.25}$$

In the last step the operators have been put onto Keldysh contours and the colored notation from the previous section has been introduced again where $+$,$-$,a,b (1,2,α,β) stand for contour (Keldysh) indices and 0,1 are sites. Since there is no superconducting term present this time we can write these terms as time dependent operators on Keldysh contours without problems, unlike the last section where the superconducting term had a peculiar energy dependence and hence a nontrivial time dependence as well. Using the definition of the full Green's function of [Jakobs, 2009] $G(t,t')^{ab}{}_{ij} = (-i)\langle T_c\, c^{a}{}_{i}(t)c^{\dagger b}{}_{j}(t')\rangle$ we can then write

$$J = \frac{e}{\hbar}(t^{--}{}_{10}G^{-+}{}_{01}(0,0) - t^{--}{}_{01}G^{-+}{}_{10}(0,0)) \tag{5.26}$$

where we have used that our system is time invariant, so we can just calculate the current for $t = 0$.

Next we need to Fourier-transform to energy space. We can use that

$$G(0,0) = \frac{1}{(2\pi)^2}\int \mathrm{d}\omega \mathrm{d}\omega'\, \underbrace{e^{-i\omega 0}e^{i\omega' 0}}_{1} G(\omega,\omega') \tag{5.27}$$

with a (here irrelevant) different sign in the second exponent because this corresponds to the $c^\dagger$ in the definition of G which should be the adjoint of c, so its Fourier transform gets a sign from complex conjugating. We will further use that

$$\begin{aligned} G(\omega,\omega') &= \int \mathrm{d}t\mathrm{d}t' e^{i\omega t}e^{-i\omega' t'}\underbrace{G(t,t')}_{=G(t-t')} \overset{\tau=t'}{\underset{\delta t=t-t'}{=}} \int \mathrm{d}\tau \mathrm{d}(\delta t)e^{i\omega(\tau+\delta t)}e^{-i\omega'\tau}G(\delta t) \\ &= \underbrace{\int \mathrm{d}\tau e^{i(\omega-\omega')\tau}}_{2\pi\delta(\omega-\omega')}\int \mathrm{d}(\delta t)e^{i\omega\delta t}G(\delta t) = 2\pi\delta(\omega-\omega')G(\omega) \end{aligned} \tag{5.28}$$

to get

$$G(0,0) = \frac{1}{(2\pi)^2}\int \mathrm{d}\omega\mathrm{d}\omega' 2\pi\delta(\omega-\omega')G(\omega) = \frac{1}{2\pi}\int \mathrm{d}\omega G(\omega). \tag{5.29}$$

Now we can write the current (5.26) as

$$J = -\frac{e}{h}\int_{-\infty}^{\infty}\mathrm{d}\omega\left(t^{--}{}_{10}G^{-+}{}_{01}(\omega) - t^{--}{}_{01}G^{-+}{}_{10}(\omega)\right) \tag{5.30}$$

with the factor $\frac{1}{2\pi}$ canceled with the bar in $\hbar$.

The next step is to make use of Dyson equations to only have Green's functions left that purely have site indices either in the center or in a lead. Denote the pure lead Green's function (i.e. the propagator of electrons in an isolated lead that is not coupled to the central region) as g. Now we have the Dyson equations

$$G^{-+}{}_{10} = G^{-a}{}_{11} t^{aa}{}_{10} g^{a+}{}_{00} \tag{5.31}$$

$$G^{-+}{}_{01} = g^{-a}{}_{00} t^{aa}{}_{01} G^{a+}{}_{11} \tag{5.32}$$

which correspond to an electron in the lead propagating in the lead (g term), then necessarily hopping into the central region at some point (t term) followed by a propagation with the full propagator of the central region (G term) which of course may contain further hopping into the leads and back. The reverse case of this gives the the second term. Putting this into 5.30 gives

$$J = \frac{e}{h}\int \mathrm{d}\omega \left(t^{--}{}_{10} g^{-a}{}_{00}(\omega) t^{aa}{}_{01} G^{a+}{}_{11}(\omega) - t^{--}{}_{01} G^{-a}{}_{11}(\omega) t^{aa}{}_{10} g^{a+}{}_{00}(\omega)\right). \tag{5.33}$$

The Keldysh rotation to get to the more convenient Keldysh basis has already been introduced in the last section. Let $t := t^{--} = -t^{++}$ where the additional minus sign comes from the integration direction on the + contour being the other way around and t being a term that comes from the Hamiltonian. We then see that $t^{\alpha\beta} = (R^{-1})^{\alpha a} t^{ab} R^{b\beta} = \begin{pmatrix} 0 & t \\ t & 0 \end{pmatrix}$, so t only has terms that mix Keldysh components. But there are also terms with $-+$ components in contour space. For an arbitrary term B from a Hamiltonian, by performing the Keldysh rotation the expression of this component in terms of Keldysh indices can quickly be checked to be $B^{-+} = \frac{1}{2}(B^{22} - B^{21} + B^{12})$. Both of the summands in (5.33) have this contour structure, so we have

$$\begin{aligned} J =& \frac{e}{h}\int \mathrm{d}\omega \frac{1}{2}\Big(t^{21}{}_{10} g^{12}{}_{00} t^{21}{}_{01} G^{12}{}_{11} - t^{21}{}_{10} g^{12}{}_{00} t^{21}{}_{01} \overbrace{G^{11}{}_{11}}^{0} + t^{12}{}_{10} g^{2\alpha}{}_{00} t^{\alpha\bar{\alpha}}{}_{01} G^{\bar{\alpha}2}{}_{11} \\ & - t^{21}{}_{01} G^{12}{}_{11} t^{21}{}_{10} g^{12}{}_{00} + t^{21}{}_{01} G^{12}{}_{11} t^{21}{}_{10} \underbrace{g^{11}{}_{00}}_{0} - t^{12}{}_{01} G^{2\alpha}{}_{11} t^{\alpha\bar{\alpha}}{}_{10} g^{\bar{\alpha}2}{}_{00}\Big). \end{aligned} \tag{5.34}$$

The outermost Keldysh indices are given by the Keldysh rotation while the inner ones were deduced where possible using that t must mix Keldysh indices and that 11 components of Green's functions in Keldysh space disappear.

Since the leads are assumed to be in equilibrium, the isolated lead Green's function g will follow a fluctuation dissipation theorem stating that $g^{22}{}_{00} = (1 - 2n_F^L)(g^{21}{}_{00} - g^{12}{}_{00})$ with n_F^L being the temperature and chemical potential dependent Fermi-distribution for the left lead. Using this and the remark above that $t_{ij} = t^{12}{}_{ij} = t^{21}{}_{ij}$ we can rewrite 5.34 to

$$J = \frac{e}{2h}\int \mathrm{d}\omega t_{10}(g^{21}{}_{00} - g^{12}{}_{00}) t_{01}\left(G^{22}{}_{11} + (1 - 2n_F^L)\left(G^{12}{}_{11} - G^{21}{}_{11}\right)\right). \tag{5.35}$$

At this point it is convenient to introduce a hybridization function (or coupling function) for the left lead as

$$\Gamma^L(\omega) = i t_{10}(g^{21}{}_{00}(\omega) - g^{12}{}_{00}(\omega)) t_{01}. \tag{5.36}$$

This is also often seen as a matrix in the space of central sites which has this expression as the Γ^L_{11} entry, since that is the site in the central region that the left lead is coupled to, and is 0 in every other entry. Γ^R is the equivalent expression for the right lead which is then a matrix with only the Γ^R_{NN} entry not zero. Making use of this definition we get

$$J = -\frac{ie}{2h}\int \mathrm{d}\omega \Gamma^L_{11}(G^{22}{}_{11} + (1-2n^L_F)\left(G^{12}{}_{11} - G^{21}{}_{11}\right)\right). \tag{5.37}$$

We keep this result in mind for the moment and proceed by formulating a Dyson equation, this time for the full propagator inside the central region, which will allow us to replace the Keldysh component G^{22} in (5.37) with retarded (G^{21}) and advanced (G^{12}) components, since we have already found a formula to calculate those in the last section. The Dyson equation reads

$$G^{\alpha\beta}{}_{11} = (g^c)^{\alpha\beta}{}_{11} + (g^c)^{\alpha\gamma}{}_{1i}\Sigma^{\gamma\delta}{}_{ij}G^{\delta\beta}{}_{j1} \tag{5.38}$$

with g^c being the Green's function of the isolated central region. The Keldysh component of g^c has the function of a regularization in a finite isolated system and can therefore be ignored when a self-energy with finite imaginary part is present.

This Dyson equation can be solved for G and by block matrix inversion we get

$$G^{12}{}_{ij} = \left((g^c)^{12} - \Sigma^{21}\right)^{-1}_{ij}, \quad G^{21}{}_{ij} = \left((g^c)^{21} - \Sigma^{12}\right)^{-1}_{ij} \tag{5.39}$$

$$G^{22}{}_{ij} = G^{21}{}_{ik}\Sigma^{11}{}_{kl}G^{12}{}_{lj} = -i(1-2n^L_F)G^{21}{}_{ik}\Gamma^L_{kl}G^{12}{}_{lj} - i(1-2n^R_F)G^{21}{}_{ik}\Gamma^R_{kl}G^{12}{}_{lj} \tag{5.40}$$

and putting together the two equations in 5.39 we additionally have

$$\begin{aligned} G^{21} - G^{12} &= G^{21}((G^{12})^{-1} - (G^{21})^{-1})G^{12} = G^{21}((\underbrace{\Sigma^{12}}_{t^{12}g^{21}t^{12}}) - (\underbrace{\Sigma^{21}}_{t^{21}g^{12}t^{21}}))G^{12} \\ &= -iG^{21}(\Gamma^L + \Gamma^R)G^{12}. \end{aligned} \tag{5.41}$$

Finally putting all these into the current formula 5.37 we get the final result

$$\begin{aligned} J = &-\frac{ie}{2h}\int \mathrm{d}\omega\Gamma^L_{11}(-i(1-2n^L_F)G^{21}{}_{11}\Gamma^L_{11}G^{12}{}_{11} - i(1-2n^R_F)G^{21}{}_{1N}\Gamma^R_{NN}G^{12}{}_{N1} \\ &+ (1-2n^L_F)\left(iG^{21}{}_{11}\Gamma^L_{11}G^{12}{}_{11} + iG^{21}{}_{1N}\Gamma^R_{NN}G^{12}{}_{N1}\right) \\ =&\frac{e}{2h}\int \mathrm{d}\omega\Gamma^L_{11}\left((1-2n^L_F)G^{21}{}_{1N}\Gamma^R_{NN}G^{12}{}_{N1} - (1-2n^R_F)G^{21}{}_{1N}\Gamma^R_{NN}G^{12}{}_{N1}\right) \\ =&\frac{e}{h}\int \mathrm{d}\omega\left(n^R_F(\omega) - n^L_F(\omega)\right)\Gamma^L_{11}(\omega)G^{21}{}_{1N}(\omega)\Gamma^R_{NN}(\omega)G^{12}{}_{N1}(\omega) \\ =&\frac{e}{h}\int \mathrm{d}\omega\left(n^R_F - n^L_F\right)\mathrm{Tr}[\Gamma^L G^{21}\Gamma^R G^{12}] \end{aligned} \tag{5.42}$$

which is the Meir-Wingreen formula again. So we now know that we can trust this current formula even for the superconducting system as Δ has the same Keldysh-structure as t (see

[Larkin and Ovchinnikov, 1977]) and Δ does not have to be treated as a contribution to the self-energy.

The conductance G^c is defined as the change of the current under an infinitesimal change of the (possibly large) bias voltage V_b between the two leads:

$$G^c = \frac{\partial J}{\partial V_\mathrm{b}}. \tag{5.43}$$

To be exact, the bias voltage is defined as the difference of the chemical potentials μ_R, μ_L of the two leads (which have a chemical potential in the first place because they are assumed to be in equilibrium) and we have $eV_\mathrm{b} = \mu_R - \mu_L$. We can choose to make either one or both of the lead chemical potentials change with V_bias to give them this difference and we get slightly different results corresponding to slightly different ways to measure this quantity in experiments. The calculation is similar either way, so for now we choose both of them to change, away from an average potential μ_0, and define $\mu_R = \mu_0 + e\frac{V_\mathrm{b}}{2}$ and $\mu_L = \mu_0 - e\frac{V_\mathrm{b}}{2}$.

From our result (5.42), we get

$$G^c = \frac{e}{h}\int \mathrm{d}\omega\ \partial_{V_\mathrm{b}}\Big(\frac{1}{e^{\beta(\omega-\mu_R)}+1} - \frac{1}{e^{\beta(\omega-\mu_L)}+1}\Big)\underbrace{\Gamma^L_{11}(\omega)G^{21}{}_{1N}(\omega)\Gamma^R_{NN}(\omega)G^{12}{}_{N1}(\omega)}_{=:\bar{T}(\omega)} \tag{5.44}$$

where $\beta = 1/T$ corresponds to the temperature of the system. So it might look like we can use our model for a system at arbitrary temperature, but we have actually already made a low temperature assumption when we looked in more detail at the mean field approach that leads to the Kitaev model in the first place in (5.3). The assumption (5.4) that the interaction happens to electrons at exactly the chemical potential is of course false for finite temperature. So although these formulas are still a good approximation for low temperatures, they have to be used carefully - to properly take finite temperatures into account we would have to integrate over temperature broadened energy intervals around μ_s and try to adjust the rest of the calculation accordingly.

Luckily, as discussed in the last chapter, the temperature is the smallest energy scale involved for the experiments we hope to describe, so it is a valid approximation to set $T = 0$ and hence $\beta = \infty$ in the following. For $T = 0$ the Fermi distribution becomes a step function at the chemical potential. This simplifies (5.44) significantly to

$$\begin{aligned}
G^c =& \frac{e}{h}\int \mathrm{d}\omega\ \partial_{V_\mathrm{b}}\Big((\theta(-\omega+\mu_0+eV_\mathrm{b}/2) - \theta(-\omega+\mu_0-eV_\mathrm{b}/2)\Big)\bar{T}(\omega)\\
=& \frac{e}{h}\int \mathrm{d}\omega\Big((\frac{e}{2}\delta(-\omega+\mu_0+eV_\mathrm{b}/2) - \Big(-\frac{e}{2}\Big)\,\delta(-\omega+\mu_0-eV_\mathrm{b}/2)\Big)\bar{T}(\omega)\\
=& \frac{e^2}{2h}\left[\bar{T}(\mu_0+eV_\mathrm{b}/2) + \bar{T}(\mu_0-eV_\mathrm{b}/2)\right]\\
=& \frac{e^2}{2h}\Bigg[\Gamma^L(\mu_0+e\frac{V_\mathrm{b}}{2})\Gamma^R(\mu_0+e\frac{V_\mathrm{b}}{2})\Big|G^{21}{}_{1N}(\mu_0+e\frac{V_\mathrm{b}}{2})\Big|^2\\
&+\Gamma^L(\mu_0-e\frac{V_\mathrm{b}}{2})\Gamma^R(\mu_0-e\frac{V_\mathrm{b}}{2})\Big|G^{21}{}_{1N}(\mu_0-e\frac{V_\mathrm{b}}{2})\Big|^2\Bigg].
\end{aligned} \tag{5.45}$$

which is a rather standard conductance formula [Datta, 1995]. So in summary, to calculate the conductance through the system with formula (5.45), the Γ^L and Γ^R are given according to (5.36), while the Green's functions have to be calculated from (5.18) and (5.19) for positive and negative energies respectively.

With this we now have the tools at hand to start looking at concrete setups of wires with superconducting areas in the central region and arbitrary potential barriers that can be used to model quantum point contacts. We have access to the electron states in the system by looking at the LDoS / spectral function with (5.20) and we can look at the transport properties by calculating the differential conductance (or, if we want, linear conductance by setting $V_\mathrm{b} = 0$) with (5.45).

First we will use this in the following chapter 6, discussing a system with a potential barrier inside a superconducting gapped region. We will look at the localized states and in particular Majorana states that appear at the border of the superconducting gap and inside the gapped region due to the potential barrier. Then, in chapter 7, we have a look at the differential conductance of a system with a quantum point contact outside a superconducting region. This approximates the setups of several recent experiments ([Das et al., 2012] [Mourik et al., 2012]) and we will try to see how much of their reported zero-bias structure in the differential conductance can be reproduced by our simple model.

Chapter 6

Appearance of Majorana Fermions in the Model

Before we try to use our new tools from the last chapter to describe a system that tries to imitate the experimental setups (see chapter 7), let us first use this chapter to get a better intuition for what happens in the superconducting regions of the wire. In particular, we will have a quick look at the bare wire with only a superconducting region but no barrier, first without and then with leads attached (section 6.1).

Following that, we turn on an additional potential barrier inside the gapped region and examine the appearing new localized states (section 6.2). In particular it can be seen how such an external potential, which would just correspond to a gate in an experiment, allows controlled creation and manipulation of MFs. This could be used to exploit the non-Abelian exchange statistics that was mentioned earlier to realize quantum computation. To finally see what is meant by that and appreciate this point, we will have a brief review of non-Abelian statistics in section 6.3.

6.1 The Quantum Wire with Superconducting Region

We now finally use our results from chapter 5 on a wire with a superconducting region. As was mentioned in chapter 4, the superconducting term creates a gap in the density of states since the creation of a Cooper pair is more favorable in this region. Furthermore, in an isolated pieces of superconducting wire in the topological phase, Majorana fermions appear, which are exponentially localized states at the first and last site. These can clearly be seen in the two strong peaks at zero energy in figure 6.1 for the case of a finite topological superconducting wire with no leads. Simply from diagonalizing the Hamiltonian matrix H at this point, we can look at the discrete energy spectrum (left plot in figure 6.2) to single out the two zero-energy Majorana modes (right plot in figure 6.2), and then plot the corresponding eigenvectors (figure 6.3). In the logarithmic plot we see that the wave-functions of the Majorana fermions are indeed exponentially localized at the first and last site, as it was predicted in [Kitaev, 2000]. From the finite distance of the localized

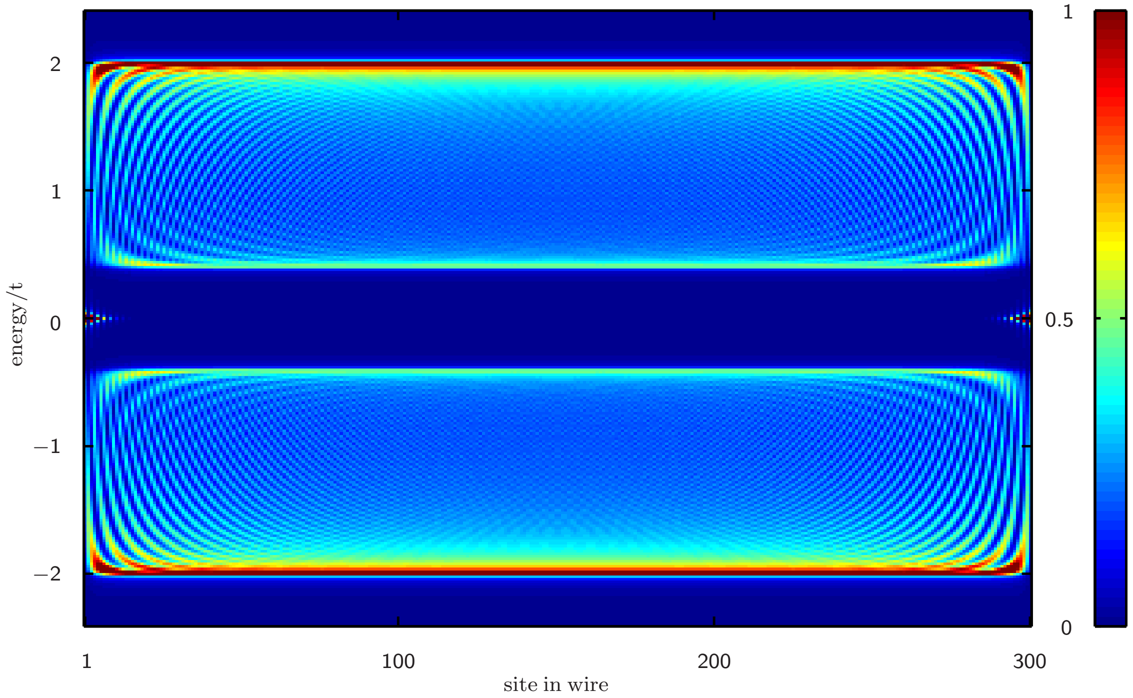

Figure 6.1: The LDoS (color scale) of a finite wire consisting only of a superconducting region with no leads attached to it, plotted over the site (x-axis) and energy (y-axis). $N = 300$ sites, $\Delta = 0.4$ SC gap width, $\epsilon = 4/N$.

states we expect a slight energy shift away from zero-energy by hybridization (section 4.2), but this shift drops exponentially with their distance and turns out to be smaller than the computational accuracy for distance bigger than about 200 sites already. Such an isolated wire is illustrative for the appearance of MF modes, but ultimately we will be interested in the experimental situation with leads attached to the system to measure conductance. This data would show signatures of appearing Majorana modes and make them accessible to experiments.

Adding the leads in the way that was worked out in the previous chapter, we get an LDoS that lacks the signature of strongly localized MFs. Instead the MFs have now spread out into the leads. We can illustrate this by taking a finite system with some lead sites connected to each site of the superconducting region. The eigenvectors belonging to the MF now show a spread out amplitude along the wire parts in the right diagram of figure 6.4. In case of true infinite leads the MFs would spread out into the whole lead and the local amplitude goes to zero.

With our formula (5.45) we can calculate the differential conductance through this system with

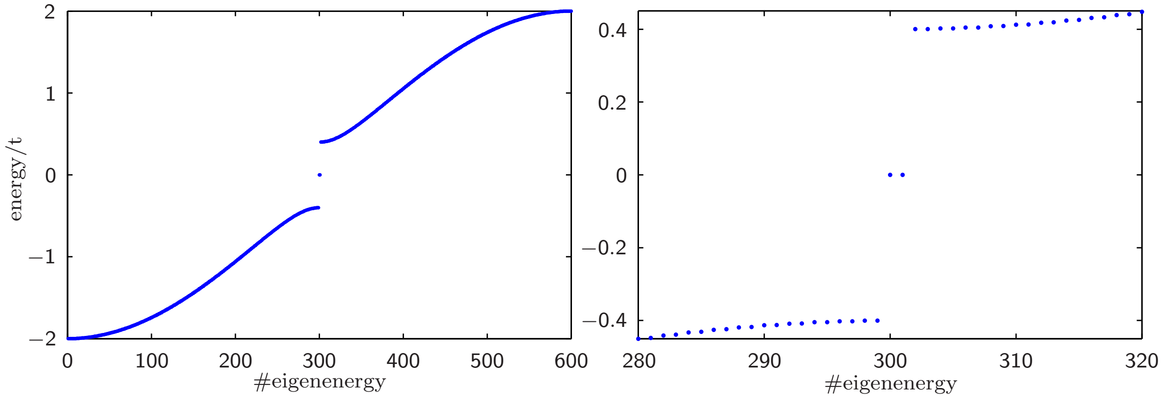

Figure 6.2: The discrete spectrum of the finite wire, gained by diagonalizing the Hamiltonian. The left plot shows the whole spectrum of eigenenergies sorted by size from smallest to biggest. The right plot is zoomed in to the eigenenergies close to zero-energy. There are two zero-energy modes visible in the right plot (#300 and #301). $N = 300$ sites, $\Delta = 0.4$ SC gap.

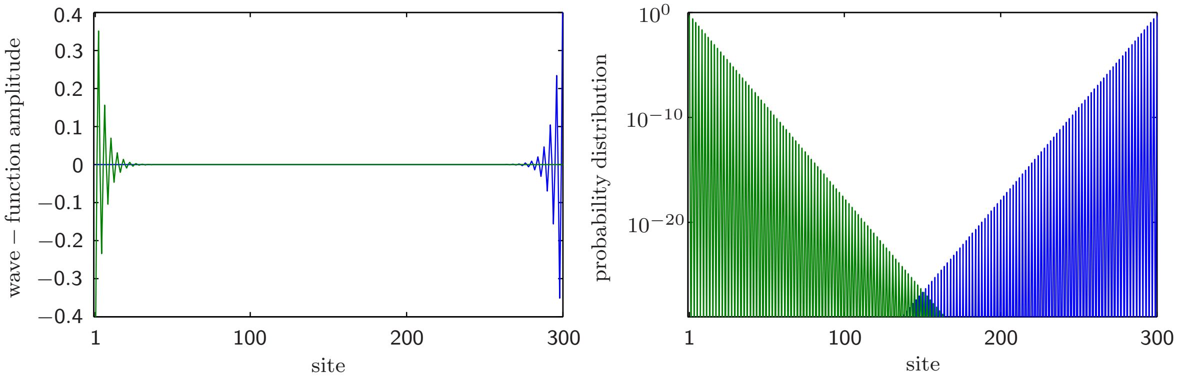

Figure 6.3: Plot of the eigenvectors corresponding to the eigenenergies #300 (blue) and #301 (green) from figure 6.2.
Left side: The amplitude of the wave-functions, which are given by the entries of the eigenvectors.
Right side: Logarithmic plot of the squared absolute values of the amplitudes, giving the probability distribution of the state and indeed showing a perfect exponential localization at the first and last site.

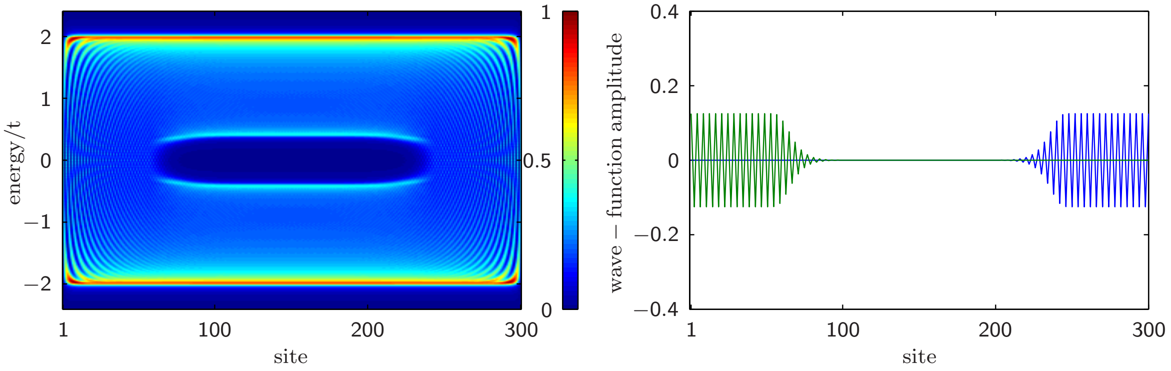

Figure 6.4: In the situation of a finite number of lead-sites added to the superconducting region with a smooth onset of the SC term (LDoS for this situation shown in the left plot, $N = 300$ sites, $d = 200$ sites SC region, $\Delta = 0.4$), there are still zero-energy modes in the energy spectrum, but the amplitude of the eigenvectors belonging to these zero-energy Majorana modes (one in blue, one in green) is now spread into the lead sites (right plot).

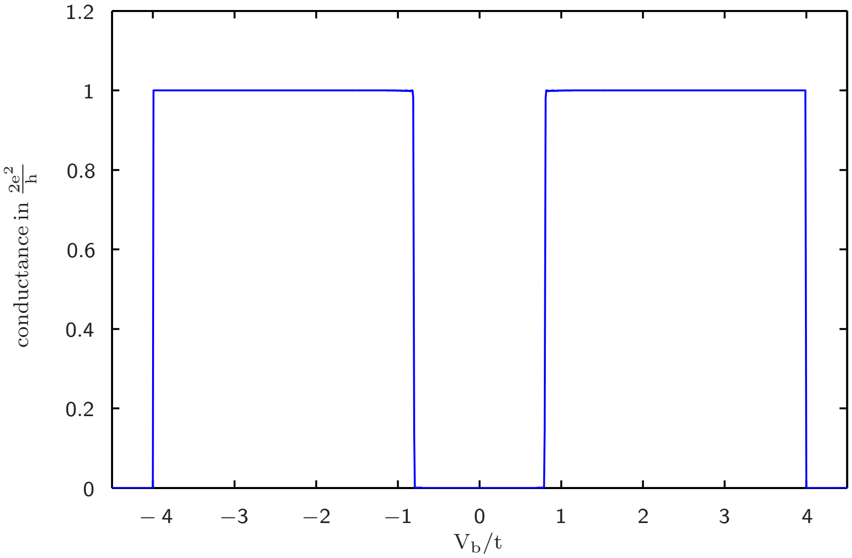

Figure 6.5: Differential conductance through a superconducting region with $N = 300$ sites connected to a semi-infinite lead on each border. The x-axis shows the finite potential difference, the y-axis the conductance, i.e. the current answer of the system to a small voltage perturbation at this offset.

leads. In the resulting figure 6.5 we see that for bias voltages between -0.8 and 0.8 no conductance takes place, since the chemical potentials in both the leads hit the superconducting gap. For bigger bias voltages, the electrons can pass through the unaffected band outside the gap, before the width of the band is reached at -4 and 4. But the result in figure 6.5 shows that the spread out and no longer localized MFs are not able to cause a zero-bias peak. To make this signature of the existence of Majorana modes visible to us we need to localize at least one of the MF modes again, even in the presence of infinite leads which are necessary to make sense of conductance. We will discuss a setup in chapter 7 that achieves this with an additional potential barrier in some distance from the superconducting region.

But before we concern ourselves with the experimental verification of the MFs, let us in the following section explore our model a bit further to get more insight in the behavior of MFs and how they can be used in the possible future application as topological quantum computers (section 6.3).

6.2 Localized States at the Potential Barrier inside the Gap

We now turn on a potential barrier inside the gapped region. The barrier height is chosen to be $f = 2.2$ and hence above the chemical potential, so as described in chapter 4, we expect a new pair of Majorana fermions to appear at these boundaries between the topological and trivial phase of the superconductor. This can be seen in figure 6.6 along with many other localized states inside the gap. We know those are localized states since they are invisible in the LDoS plot without a finite ϵ term (right side of figure 6.6), so they do not get a finite lifetime from the presence of the leads and hence can not escape.

To understand where these localized states inside the gap in 6.6 come from, we again rewrite our Kitaev model Hamiltonian

$$H = \sum_{j=1}^{N} \epsilon_j c_j^\dagger c_j + \sum_{j=1}^{N-1} \left(t c_{j+1}^\dagger c_j + t c_j^\dagger c_{j+1} + \Delta c_{j+1} c_j + \Delta^* c_j^\dagger c_{j+1}^\dagger \right) \tag{6.1}$$

in terms of the Majorana fermions d_{2j} and d_{2j+1} by defining

$$\begin{aligned} c_j &= \frac{1}{2}(d_{2j} + i d_{2j+1}) \\ c_j^\dagger &= \frac{1}{2}(d_{2j} - i d_{2j+1}) \end{aligned} \tag{6.2}$$

as Kitaev already did in his original paper [Kitaev, 2000]. The Majorana fermions can be seen as “half fermions” with the remarkable property of being their own antiparticle, i.e. $d_{2j} = d_{2j}^\dagger$. We put these definitions into the Hamiltonian and note that the fermionic commutation relations apply to the Majorana fermion operators, such that four of the terms vanish. Assuming that Δ is real, we

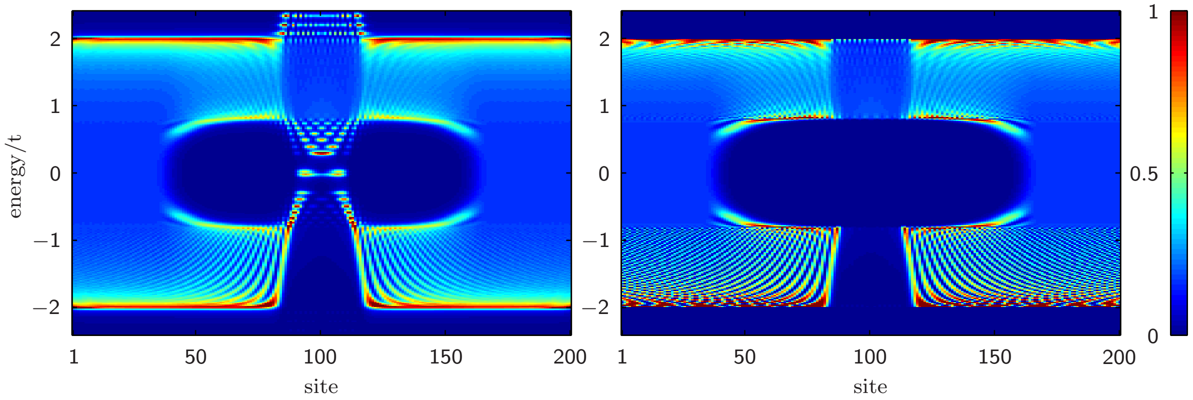

Figure 6.6: The LDoS of a wire with a potential barrier of height $f = 2.2$ inside the gapped region. Central region with $N = 200$ sites connected to a lead on either side. $\Delta = 0.8$.
Left plot: Artificial imaginary term $\epsilon = 4/N$ to make the many localized states inside the gapped region visible.
Right plot: Comparative plot with $\epsilon = 0$ to appreciate that the new states we see are localized states - they are not visible, so they do not get a finite lifetime from the presence of the leads.

are left with

$$\begin{aligned} H =& \frac{1}{4}\sum_{j=1}^{N}\left[\epsilon_j\left(d_{2j}^2 + d_{2j+1}^2\right) + i\epsilon_j\left(d_{2j}d_{2j+1} - d_{2j+1}d_{2j}\right)\right] \\ &+ \frac{1}{4}\sum_{j=1}^{N-1}\left[2i(\Delta+t)d_{2j+2}d_{2j+1} + 2i(\Delta-t)d_{2j+3}d_{2j}\right]. \end{aligned} \tag{6.3}$$

We use that $d_{2j}^2 = 1$ (see (6.12)), so that the first term is just a constant in the Hamiltonian which can be left out. Since we are only interested in the qualitative source of these localized states, we can constrain ourselves to the case $\Delta = t$ in which the last term disappears too.

So we only have

$$H = \frac{i}{2}\sum_{j=1}^{N}\epsilon_j d_{2j}d_{2j+1} + \frac{i}{2}\sum_{j=1}^{N-1}\underbrace{(\Delta+t)}_{2t}d_{2j+2}d_{2j+1}. \tag{6.4}$$

Next we want to put the half-fermions back together, but shifted by one, such that two Majorana fermions coming from neighboring sites get combined together as sketched in figure 6.7. So define

$$\begin{aligned} \tilde{c}_j &= \frac{1}{2}(d_{2j} + id_{2j-1}) \\ \tilde{c}_j^\dagger &= \frac{1}{2}(d_{2j} - id_{2j-1}). \end{aligned} \tag{6.5}$$

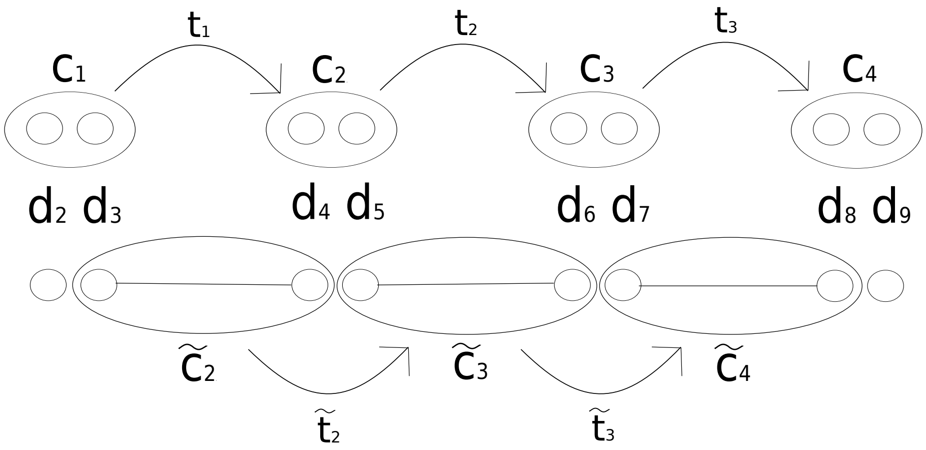

Figure 6.7: Sketch of the rewriting of the Hamiltonian 6.1 into 6.7. The electron creation operators c (top) get divided into two Majorana fermions d (middle) which then get recombined into fermionic operators $\tilde{c}$ (bottom) describing quasi-particle living at neighboring sites. t and $\tilde{t}$ are the hopping amplitudes of the original and the new sites.

Of course these new creation and annihilation operators do not describe electrons on lattice sites anymore, but some different quasi-particles excitations. Expressing those through the Majorana fermions gives

$$\begin{aligned} d_{2j-1} &= i\tilde{c}_j^\dagger - i\tilde{c}_j \\ d_{2j} &= \tilde{c}_j^\dagger + \tilde{c}_j \end{aligned} \tag{6.6}$$

and putting these into 6.4 finally leads to

$$\begin{aligned} H = &-\frac{1}{2}\left(\sum_{j=2}^{N-1}\left[\epsilon_j\tilde{c}_j^\dagger\tilde{c}_{j+1}^\dagger + \epsilon_j\tilde{c}_j\tilde{c}_{j+1}^\dagger - \epsilon_j\tilde{c}_j^\dagger\tilde{c}_{j+1} - \epsilon_j\tilde{c}_j\tilde{c}_{j+1}\right]\right. \\ &\left.+\sum_{j=1}^{N-1}2t\left[\underbrace{\tilde{c}_{j+1}^\dagger\tilde{c}_{j+1}^\dagger}_{0} + \tilde{c}_{j+1}\tilde{c}_{j+1}^\dagger - \tilde{c}_{j+1}^\dagger\tilde{c}_{j+1} - \underbrace{\tilde{c}_{j+1}\tilde{c}_{j+1}}_{0}\right]\right) \\ = &\sum_{j=1}^{N-1}\underbrace{2t}_{\tilde{\epsilon}_{j+1}}\tilde{c}_{j+1}^\dagger\tilde{c}_{j+1} + \sum_{j=2}^{N-1}\underbrace{\frac{\epsilon_j}{2}}_{\tilde{t}_j}\left(\tilde{c}_{j+1}^\dagger\tilde{c}_j + \tilde{c}_j^\dagger\tilde{c}_{j+1}\right) + \sum_{j=2}^{N-1}\frac{\epsilon_j}{2}\left(\tilde{c}_{j+1}^\dagger\tilde{c}_j^\dagger + \tilde{c}_j\tilde{c}_{j+1}\right). \end{aligned} \tag{6.7}$$

In this representation of the Hamiltonian, the hopping amplitude and the ϵ_j, which contains chemical potential and barrier potential, have changed places! We can now realize this new Hamiltonian in a matrix form and calculate the LDoS from it. As we can see in figure (6.8), these new quasi-particles

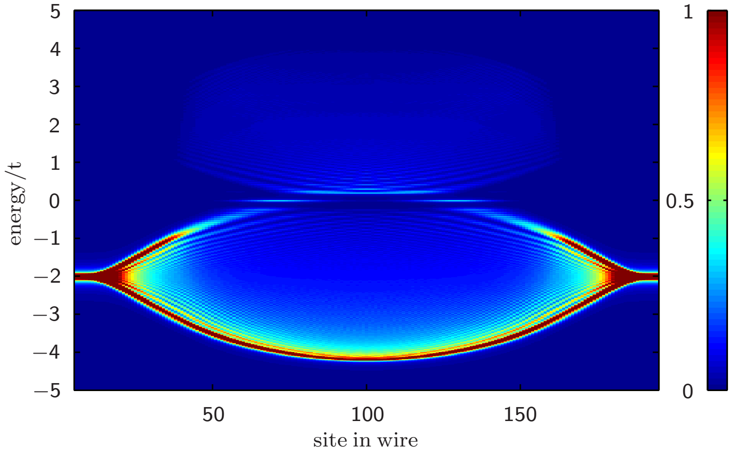

Figure 6.8: The LDoS of the quasi-particles described by $\tilde{c}^\dagger$ and $\tilde{c}$ in the rewritten Hamiltonian (6.7). It is $N = 200$ with a SC gap between the 30. and 170. site. $f = 2.2$, $t = 1.0$, $\Delta = 1.0$.

have a very different band shape and can only appear in the region where the normal LDoS showed a gap.

We have now understood the origin of these localized states. Apart from the possible Majorana State that might be among them, these states are not connecting to the leads and hence not important for the conductance, which is the main measurement quantity in today's MF experiments. So instead, we will now concentrate on the Majorana states again.

6.3 Non-Abelian Exchange Statistics

As we have seen in the previous section, we can turn additional MFs in the topological superconductor on and off simply by adding a potential barrier, for example with a tunable gate. In the same way, moving this barrier moves the MF along with it - which could be realized by putting a whole "keyboard" ([Alicea et al., 2010]) of tunable gates along the wire. This is particularly interesting when we consider the maybe most unusual property of Majorana fermions that we have not yet talked about - their non-Abelian exchange statistics. The meaning is quickly explained. As is well known, states consisting of bosonic (fermionic) particles gain a prefactor of $+1(-1)$ under exchange of two particles. This can be generalized to so called (Abelian-)anyons, which are defined by their property of gaining a different complex phase factor under particle exchange. We will see in this section that the Majorana fermions go a step further: They not only give a complex phase under exchange, but can change the (ground-)state of the system entirely, depending on the order of the exchanges. Such particles are in general called non-Abelian anyons. In this case, the exchanges can change between different superpositions of the 2^l-fold degenerate ground states that result from the presence of $2l$ Majorana fermions in the system, since pairs of MF then make up l fermionic degrees of freedom which can each either be filled or empty.

This could be used to build a topological quantum computer, based solely on exchanging these well-protected Majorana modes with each other to carry out calculations. This systematic exchanging of many Majorana modes with each other is called "braiding". However, the braiding operations correspond to a $\pi/2$ rotation of a single qubit [Leijnse and Flensberg, 2012, section 3.3] and using them alone is limiting in what calculations would be possible, so it has been considered to combine the concept with other qubits or operations (for example [Nayak et al., 2008], [Hassler et al., 2010] and [Leijnse and Flensberg, 2011]) to allow for universal quantum computation.

It is possible to show this non-Abelian anyon behavior analytically from the formalism we have introduced so far. This has been done for the 1D topological superconducting wire case by J. Alicea in detail in the supplementary material to [Alicea et al., 2010].

However, there is a simpler picture for the case of MFs as vortices on the surface of a 2D topological insulator given in [Leijnse and Flensberg, 2012, section 3.2] following the paper [Ivanov, 2001]. Since the basic concept and the implications of the result are true for all realizations of Majorana fermions, we will for simplicity follow the later picture in the following paragraphs as an example of non-Abelian exchange statistics.

First recall from (4.5) how fermionic operators c can be split into two "half-fermion" Majorana operators d:

$$c_i = \frac{1}{2}\left(d_{2i-1} + i d_{2i}\right), \qquad c_i^\dagger = \frac{1}{2}\left(d_{2i-1} - i d_{2i}\right). \tag{6.8}$$

These equations can be inverted to get

$$d_{2i-1} = c_i + c_i^\dagger, \qquad d_{2i} = i(c_i^\dagger - c_i), \tag{6.9}$$

where we have used that the Majorana states fulfill $d_{2i} = d_{2i}^\dagger$ and $d_{2i-1} = d_{2i-1}^\dagger$ since they are their own antiparticle.

At this point we can calculate the commutation relations $\{d_k, d_l\}$ of Majorana fermions by inserting the relations (6.9) and applying the fermionic ones. For example for the case of odd $k = 2i-1$ and odd $l = 2j-1$ it follows

$$\begin{aligned}\{d_k, d_l\} &= \{d_{2i-1}, d_{2j-1}\} = d_{2i-1}d_{2j-1} + d_{2j-1}d_{2i-1} = i(c_i^\dagger - c_i)i(c_j^\dagger - c_j) + i(c_j^\dagger - c_j)i(c_i^\dagger - c_i) \\ &= -(c_i^\dagger c_j^\dagger - c_i^\dagger c_j - c_i c_j^\dagger + c_i c_j) - (\underbrace{c_j^\dagger c_i^\dagger}_{-c_i^\dagger c_j^\dagger} - c_j^\dagger c_i - c_j c_i^\dagger + \underbrace{c_j c_i}_{-c_i c_j}) = \{c_i^\dagger, c_j\} + \{c_j^\dagger, c_i\} = 2\delta_{ij}.\end{aligned} \tag{6.10}$$

The same result for the remaining odd/even cases leads to the general conclusion

$$\{d_k, d_l\} = 2\delta_{kl}. \tag{6.11}$$

The last important relation we need is

$$d_k^2 = 1 \tag{6.12}$$

which follows from (6.11) by simply taking $2 = \{d_k, d_k\} = 2d_k^2$. We now know that Majorana modes do not fulfill a Pauli-principle, since applying the creation operator twice simply is an identity. Furthermore, it does not even make sense to speak of the occupancy of a Majorana mode in the usual way, as the regular counting operator $n_k^{MF} = d_k^\dagger d_k = d_k^2 = 1$ is also the identity. We can make sense of this by remembering that a Majorana mode is just half a degree of freedom - it has to be coupled with another Majorana to be accessible.

We now demonstrate how these modes have non-Abelian statistics in the example of the realization as vortices on the surface of 3D topological insulators (see section 4.2 and 4.4) mostly following the review article [Leijnse and Flensberg, 2012]).

Each vortex corresponds to a winding of the superconducting phase of 2π. We assume the phase to be constant everywhere except on a branch cut from each vortex to a fixed direction, which is a simpler picture that reproduces the rigorous results gained on the level of field theories ([Semenoff, 1988] and [Eliezer and Semenoff, 1992]). The vortices can be moved, for example by magnetic gates, which control where the induced superconductor is in the topological phase. When two vortices are exchanged adiabatically in this way, exactly one of them will cross the branch cut of the other vortex, picking up a phase of half of 2π. This is because the superconducting phase is defined as the phase of cooper pairs consisting of two fermions, while the Majorana fermion in the vortex contains single fermion operators (6.9). A phase shift of π is exactly a sign change, so one of the Majorana modes will change signs while the other does not.

This exchange of two modes d_k and d_l can be described by what is called a "braid operator"

$$B_{kl} = (1 + d_k d_l)\,\frac{1}{\sqrt{2}} \tag{6.13}$$

which acts as $B_{kl} d_k B_{kl}^\dagger = (1 + d_k d_l) d_k (1 + d_l d_k)/2 = (d_k - 2d_l - d_k)/2 = -d_l$ and $B_{kl} d_l B_{kl}^\dagger = d_k$ using (6.11), (6.12).

Let us begin with the case of only two vortices d_1, d_2 that can be combined into one fermionic operator $c_1 = (d_1 + id_2)/2$. We then have two different states of our system: $|0\rangle$ in which the fermionic mode is not occupied and $|1\rangle = c_1^\dagger|0\rangle$. But when we now apply our braiding operator (6.13) to one of the states to exchange the two MFs

$$\begin{aligned} B_{12}|1\rangle &= \frac{1}{\sqrt{2}}(1 + d_1 d_2)(d_1 - id_2)\frac{1}{2}|0\rangle = \frac{1}{2\sqrt{2}}(d_1 - id_2 - d_2 - id_1)|0\rangle \\ &= \frac{1}{\sqrt{2}}(1 - i)\underbrace{\frac{1}{2}(d_1 - id_2)|0\rangle}_{c_1^\dagger|0\rangle} = \frac{1}{\sqrt{2}}(1 - i)|1\rangle, \end{aligned} \tag{6.14}$$

we see that we only gained a complex phase and have not changed the state of the system. This is to be expected though, as the two states correspond to an even and odd number of electrons in the superconductor, which can not be changed by particle exchanges inside it. Changing the electron number by multiples of 2 instead is possible, since the superconducting Hamiltonian allows the creation and annihilation of Cooper-pairs, so let us consider a system with four vortices d_1 to d_4 corresponding to two fermionic operators c_1 and c_3. With $|11\rangle = c_1^\dagger c_3^\dagger |00\rangle$ we have

$$\begin{aligned} B_{23}|00\rangle =& \frac{1}{\sqrt{2}}(1+d_2d_3)|00\rangle = \frac{1}{\sqrt{2}}|00\rangle + \frac{1}{\sqrt{2}}\frac{1}{4} d_2d_3(d_3+id_4)(d_1+id_2)|11\rangle \\ =& \frac{1}{\sqrt{2}}|00\rangle + \frac{1}{4\sqrt{2}}(d_2d_1 + i + \underbrace{id_2d_3d_4d_1}_{-id_1d_2d_3d_4} - d_3d_4)\underbrace{|11\rangle}_{\frac{1}{4}(d_1-id_2)(d_3-id_4)|00\rangle} \\ =& \frac{1}{\sqrt{2}}|00\rangle + \frac{1}{4\sqrt{2}}(i + i - i(-i)^2 - (-i))|11\rangle = \frac{1}{\sqrt{2}}\left[|00\rangle + i|11\rangle\right]. \end{aligned} \tag{6.15}$$

This means that we have changed the state of the system simply by exchanging particles in it. The non-Abelian exchange statistics can also be seen by calculating the commutator

$$[B_{12}, B_{23}] = \frac{1}{2}(1+d_1d_2)(1+d_2d_3) - \frac{1}{2}(1+d_2d_3)(1+d_1d_2) = \frac{1}{2}\underbrace{d_1d_2d_2d_3}_{d_1d_3} - \frac{1}{2}\underbrace{d_2d_3d_1d_2}_{-d_1d_3} = d_1d_3 \neq 0. \tag{6.16}$$

We can finally see non-Abelian anyon behavior for our Majorana states in the example of this particular realization. As mentioned in the beginning, the same can be done for other proposed realizations of MFs - see in particular [Alicea et al., 2010, Suplementary material] for the 1D wire case.

It might seem contradicting that MFs in one-dimensional wires have non-Abelian statistics, when anyons can only exist in two-dimensional systems. This can be explained by the fact that adiabatic exchange of such MFs always requires some kind of network of one dimensional wires to move them past each other while keeping a great distance, making it effectively a 2D system.

Chapter 7

Zero-Bias Peak as Experimental Signature of MFs

We will now use the tools developed in chapter 5 with a system that is modeled to follow the experimental setup of [Mourik et al., 2012] and compare the predictions of our method for the differential conductance with their experimental measurements. To this extend, we will first have a more detailed look at the published experiments in section 7.1 before deciding on the numerical model to use in 7.2 and finally compare the results. We close with a short section 7.3 of review and conclusions and give some outlook on how to proceed and improve upon the work done in this thesis.

7.1 Existing Experimental Results

As was mentioned in chapter 4, there are several recent experimental papers which claim to have found strong indications or proof for the existence of Majorana fermions as quasiparticles. Of those, we are particularly interested in the following two, which make use of the MF realization in one dimensional semiconducting wires that are tuned to behave like topological superconductors by the steps described in 4.2. These setups come closest to the original Kitaev model and are hence best suited to be approximated by and compared to our calculations. In the following, we will have a brief look at these experiments by [Mourik et al., 2012] and [Das et al., 2012] and their results. A third experimental paper, [Deng et al., 2012], also claims to have measured MFs in such a wire, but has a Josephson-junction setup instead of a single superconducting region. Our model might also be able to describe this case, but it is not attempted here.

The main ingredient of the device used in [Mourik et al., 2012] is an indium antimonide (InSb) nanowire connected to one one normal-conducting gold and one superconducting NbTiN contact. This structure is placed over an array of varying gates to manipulate the chemical potential along the wire. In particular, one narrow gate is used to create a potential barrier in the free hanging wire part between the two contacts.

An InSb wire was chosen for both the high spin-orbit-interaction and g-factor of this material. As was explained in section 4.2, the earlier is a requirement to bring the semiconductor wire into the topological superconductor state and the high g-factor leads to a big Zeeman splitting. That is necessary since the Meissner effect in the superconducting region shields that part of the wire from most of the external magnetic field and the remaining field strength must be sufficient to induce the required Zeeman splitting. This can not be solved by making the external field stronger, since the s-wave superconductor used to induce the superconductivity has a critical field strength for which superconductivity is lost.

The result of the differential conductance measurement for varying magnetic fields can be seen in figure 7.1 from [Mourik et al., 2012, figure 2A]. We see vertically shifted plots of the differential conductance over the applied bias voltage for many different external magnetic fields. As an important common feature there are clear peaks around $V = \pm 250 \mu eV$ corresponding to the gap-width. If the absolute bias voltage is smaller, the electrons meet the gapped region which is centered around the same chemical potential that is used for the $V = 0$ bias voltage case. The finite conductance even through the gapped region is attributed to an incompletely formed proximity gap and Andreev localized states. But the important structure for us is the smaller peak at zero-bias voltage appearing for a wide range of magnetic field values. It is claimed that other possible explanations for a zero-bias peak like weak anti-localization, Kondo effect and reflectionless tunneling do not fit their measurements and checks, leaving only localized Majorana states as an explanation.

Possible differences between their setups and what we can describe with our model might be given by the finite temperature and the fact that they admit to not being able to tune the superconductor-covered section of the wire to a single-band regime, making it harder to describe by our single-band model.

A few month later in the work of [Das et al., 2012], the main device consists of a suspended indium arsenide nanowire of around 60nm diameter, suspended by two gold pillars serving as contacts above the substrate on which the structure was grown. The indium arsenide is another material with strong SOI and high Zeeman splitting ([Beenakker, 2012]), making it easier to fulfill the requirements for a topological superconductor (section 4.2). Between the pillars a gate is added, then a superconducting aluminium strip to induce a superconducting region in the wire and finally another gate. While the device is symmetrical with potential barriers and contacts on both side of the induced superconducting region, the differential conductance measurements were made between the right contact and the superconducting contact, again reproducing the situation we had in [Mourik et al., 2012].

The results can be seen in figure (7.2). Again a clear zero-bias peak is visible, embedded in a valley between two much bigger peaks corresponding to the induced superconducting gap. Again other possible explanations are deemed unlikely in favor of the Majorana fermions, so we can conclude that this experiment confirms the prior results of [Mourik et al., 2012] as a similar conductance was found even though a different device design, building method and different materials were used.

A splitting of the zero-bias peak both for high and low external magnetic fields is reported. This can be explained by our discussion in 4.2 that the MF are zero-energy states which get shifted away

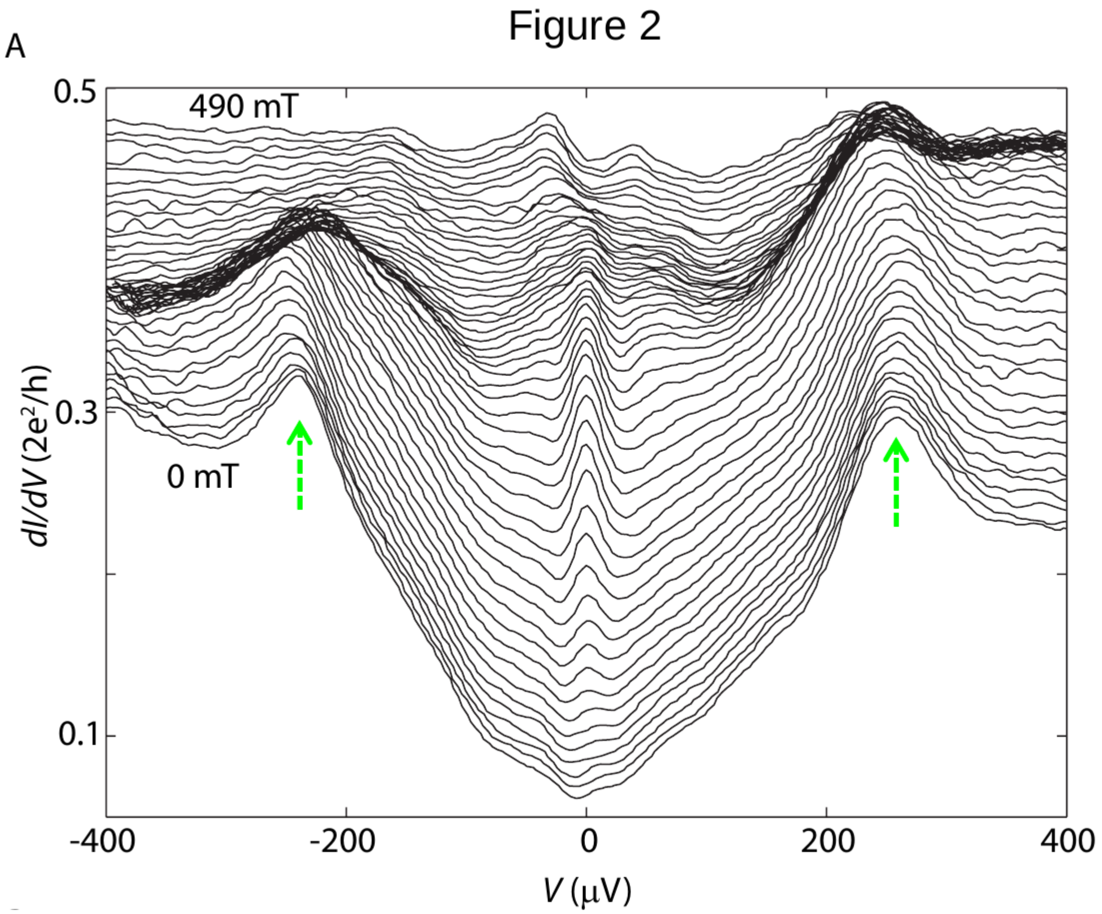

Figure 7.1: This figure from [Mourik et al., 2012] shows the measured differential conductance (y-axis) over the applied bias voltage (x-axis) for different magnetic field strength (vertical shift) at $T = 70mK$. The green arrows point to the conductance peaks from bias voltages high enough for the electrons to pass the gapped region. In between those peaks the valley from the (incompletely) gapped superconducting region is seen. For magnetic field strength between $\sim$ 100mT and $\sim$ 400mT an additional zero-bias peak appears.

from zero by hybridization if the Majorana states overlap. According to [Das et al., 2012], their extension is given by a characteristic length $\xi = \hbar v_F / E_g$ with v_F being the Fermi-velocity and E_g being the smallest gap in the dispersion relation. So for a small gap the extension of the MFs and therefore their overlap gets bigger and splitting of the zero-bias peak appears. We have a small gap either for a magnetic field too weak to induce the Zeeman splitting gap around $p = 0$ or big enough to come close to the critical field of the s-wave superconductor and hence weakening the proximity induced superconductivity in the wire that is responsible for the gap away from $p = 0$ (see figure 4.1 bottom right).

7.2 Comparison of our Calculations with the Experimental Data

Of course the interesting question now is if our model can produce similar results. First we have to decide what exact model parameters we choose to simulate the setups from the experiments. What turned out to work out best is the following, non-symmetric setting. We take the central region, connected to a lead on both ends as usual, and turn on an induced superconducting region on the right side from the lead reaching into the central region. To the left of the SC region, we put an external potential barrier in roughly the same distance as the width of the SC region (the exact distance turns out to be irrelevant). This can be seen on the LDoS plot on the right site of figure 7.3 with a clear barrier in the middle and the gapped region from the SC on the right. A similar experimental setup was used in particular by [Mourik et al., 2012, figure 1C] with a gate on the wire inducing what they call a tunnel barrier to seperate the normal conducting from the induced SC part of the wire.

We expect two Majorana fermions in this setup for our model, one for each end of the superconducting region. The right end is touched by the right lead, so the MF spreads to the whole lead. But the one on the left hand can only spread in a very limited area up to the barrier, so we have localized this Majorana state which makes it accessible for conductance as can be seen in the following conductance measurements.

The experiments of [Mourik et al., 2012] and [Das et al., 2012] needed to include the external magnetic field as an additional parameter and used a wire made of InSb and InAs which has a very high SOI in the first place. This is because, as mentioned earlier in 4.2, a lot of fine-tuning is necessary to get the topological superconductor behavior necessary for Majorana fermions in an experimental setup, while we don't consider spins and magnetic fields in our simplified toy-model and get the MFs without tuning.

In chapter 5 we have determined a formula (5.45) for the differential conductance from the left lead through the barrier and the gapped region to the right lead. With increasing bias voltage, the chemical potentials of the two leads are symmetrically shifted away from the fixed chemical potential of the superconductor that induces the gap, which is exactly at the energy around which the gap is centered. A wide valley of zero-conductance is visible in the differential conductance plots (left side of 7.3), with a width that corresponds to the gap in the density of states. For bias voltages bigger than this gap the electrons on one side have an energy high enough to easily pass

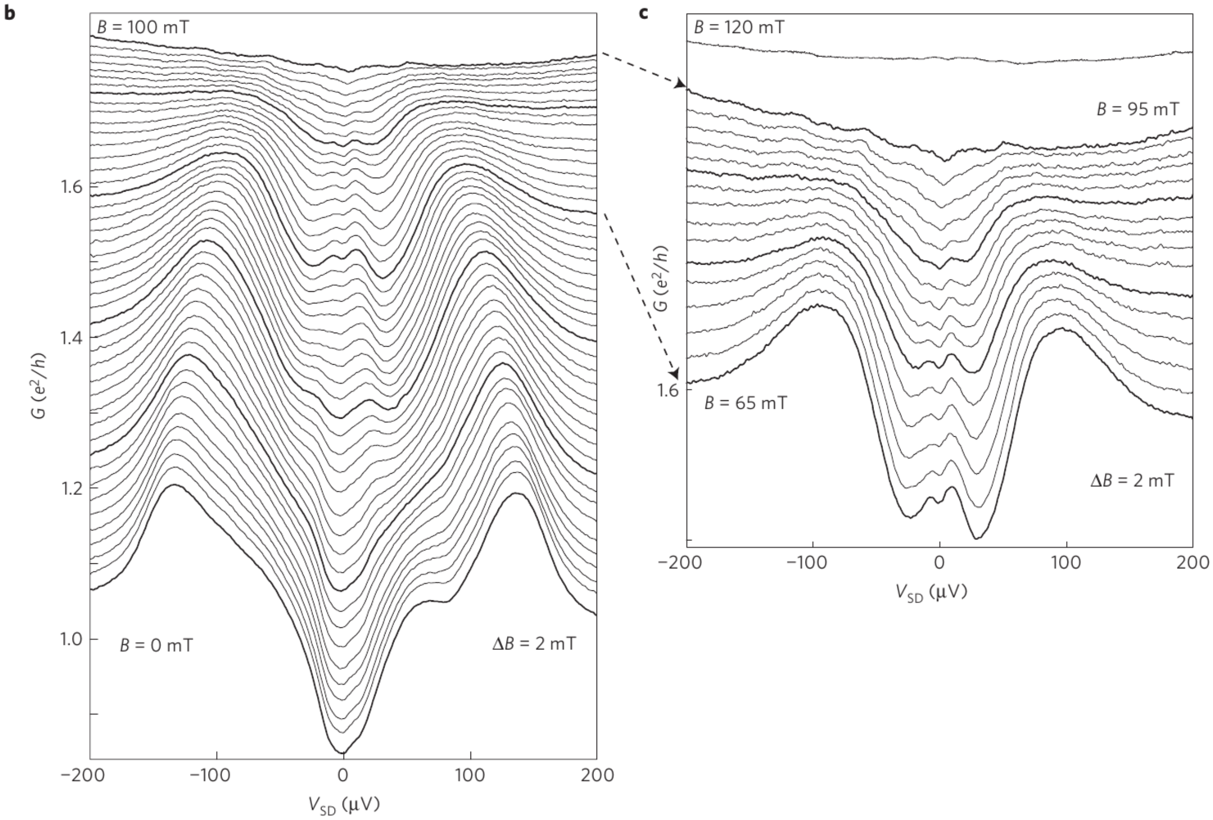

Figure 7.2: Figure from [Das et al., 2012] showing the measured differential conductance (y-axis) over the bias voltage V_{SD} (x-axis) for different external magnetic fields (vertical shift). Again, as in figure 7.1, a zero-bias peak is visible for certain values of magnetic field (see zoomed in diagram c on the right). The peak seems to be slightly split into two peaks around 0.

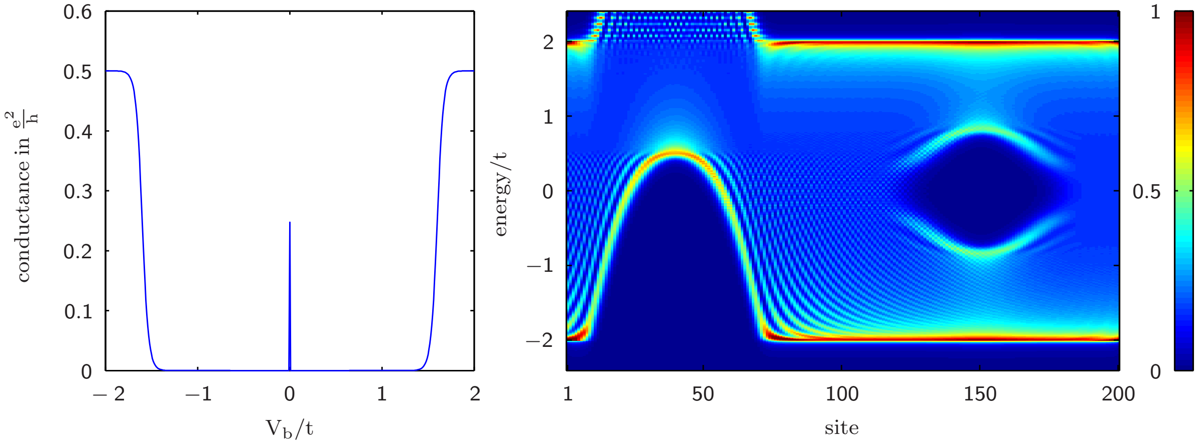

Figure 7.3: Left side: Plot of the differential conductance calculated with the formalism developed in chapter 5 with a clear zero-bias peak at $V_g = 0$. $N = 200$, $f = 2.5$, $\Delta = 0.8$.
Right side: Local density of states in the final setup show the relative size and position of the gapped region and the QPC. The zero-bias peak appears since the Majorana state spreading from the left side of the gapped region is stopped by the barrier and hence gets localized in between.

the barrier and not be affected by the gap, so the conductance outside of this valley is much bigger.

At zero-bias voltage in the center of the valley, a single, sharp peak is visible in figure 7.3. This corresponds to the additional conductance caused by the Majorana fermion state we have localized between barrier and SC region. This is the same kind of zero-bias peak in the middle of a conductance valley as was seen in the measured experimental data in 7.1 ([Mourik et al., 2012, Figure 2A]) and 7.2 ([Das et al., 2012, Figure 4b])! For figure 7.3 a system with $N = 200$ with a potential barrier of height $f = 2.5$ (width 35 sites) and a superconducting gap centered around site 150 (width 40 sites, height $\Delta = 0.8$) is used. The LDoS is also plotted on the right, since it gives a good visualization of the setup.

In the following, we will try to further analyze this peak by changing the parameters of the system. In particular, we want to see how general the appearance of such a peak is for our model. Maybe we can find out particular details that destroy the peak or make it more emphasized. Comparing such predictions with experiment could then further allow one to judge how well this model agrees with the experimental results.

We have many possible parameters available to change our system. The four we will concentrate on are the height and width of both the potential barrier and the gap in the gapped region. Another one that at first glance seems very important is the distance between those two features, but it turns out that the zero-bias peak shows no change for a wide range of distances, as is demonstrated in figure 7.5, which shows that with a very different distance but all other parameters changed, the conductance remains the same. For the remaining four parameters, the striking result is that there is a maximum height of the peak of 0.25 conductance quanta which can be reached almost always by just keeping any three of them constant and tuning the last one. This is demonstrated in the following table 7.1 showing a value of the four relevant parameters and the resulting zero-bias peak height in the last column. All other parameters are chosen as for figure 7.3, so for all these choices the LDoS and the conductance curve (apart from the peak height) look similar to the ones in the plot. For further illustration the dependance of the gap height on the geometric parameters is shown in figure 7.4.

Table 7.1: Influence of the geometric parameters of the QPC barrier and SC gap on the ZBP height.

gap width	gap height	potential width	potential height	zero-bias peak height
40	0.8	35	2.5	0.16
42	0.8	35	2.5	0.24
40	0.83	35	2.5	0.25
40	0.8	35	2.477	0.25
40	0.8	34	2.5	0.25
45	0.6	40	2.4	0.01
53	0.6	40	2.4	0.25
45	0.701	40	2.4	0.25
45	0.6	40	2.329	0.25
45	0.6	33	2.4	0.24

This is limited by the constrains one would expect, if either the barrier or gap are too short or shallow then the remaining electron states begin to be able to tunnel through them with ease and the conductance is no longer governed by the MFs. If on the other hand they get too wide the conductance drops to zero. But for most of the in-between cases, the described easy tuning of only one parameter to get a maximum peak height is possible, with the remaining limitation that the barrier and gap width can only be changed by integer lattice sites and not smoothly in our model. This is a promising result as it makes it nearly impossible for a device that behaves according to the Kitaev model to not show traces of MFs as long as one of those four parameters is accessible for tuning.

A double peak as seen in figure 7.2 can appear when two Majorana fermions are close to each other and hybridize, moving their energies away from zero. This can be shown when we move the potential barrier inside the gapped region, creating two additional normal-to-topological superconductor phase transitions in the gapped region which each carry a localized MF state close to each other (figure 7.6).

Our conductance peaks in the setup of figure 7.3 appear to be sharp delta peaks and show no inner structure, while the zero-bias peaks in the experimental papers have a finite width. We observe that the conductance only happens at exactly the energy of the Majorana modes. This peak could

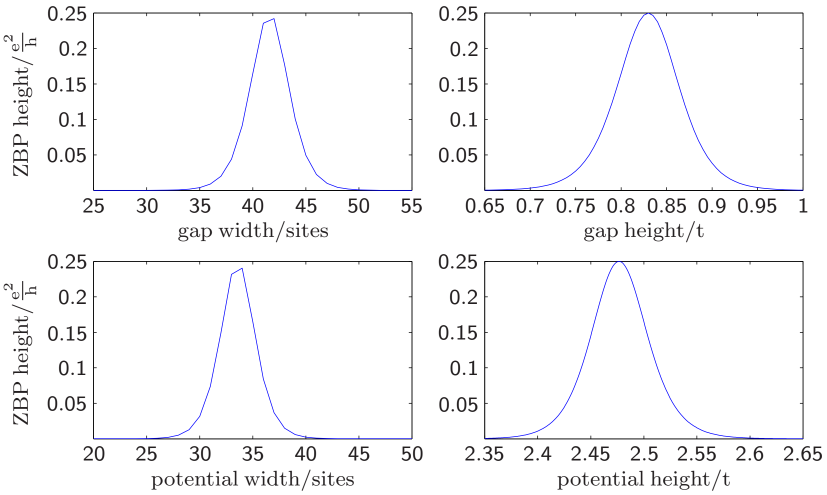

Figure 7.4: Height of the zero-bias peak (y-axis) when one of the geometric parameters is changed (x-axis) while leaving the other three to be constant at gap width 40, gap height $\Delta = 0.8$, potential width 35 and potential height $f = 2.5$. The remaining system parameters are chosen as in figure 7.3.

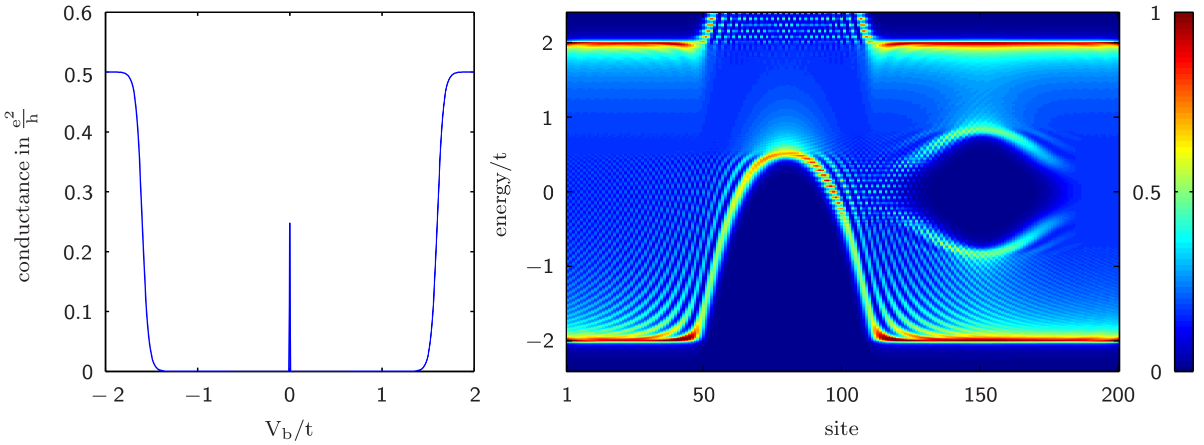

Figure 7.5: Decreasing the distance between the potential barrier and the gapped region by 50 sites compared to figure 7.3 (LDoS plot on the right) while leaving all other system parameters the same does not change the zero-bias peak (conductance plot on the left). It seems to be in general the case that the potential barrier position relative to the gap is not an important parameter in this setup.

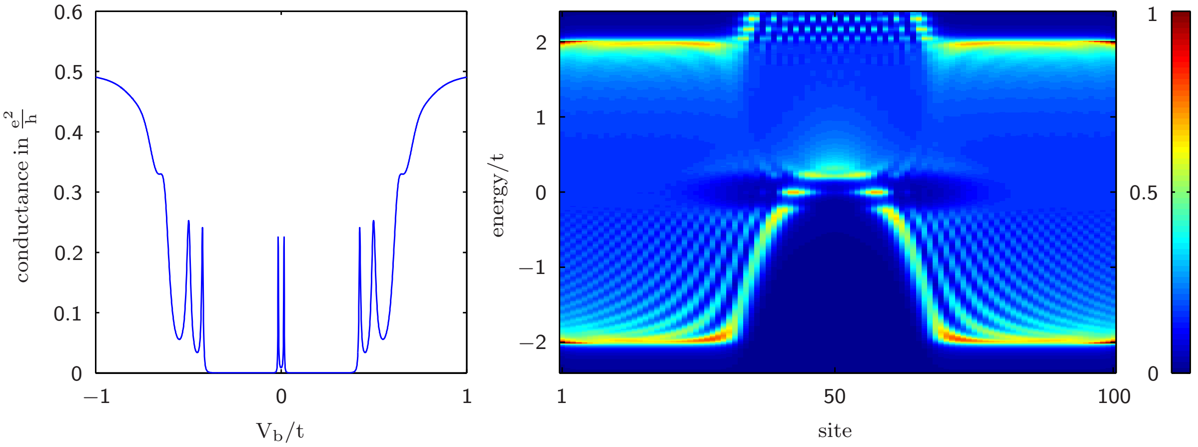

Figure 7.6: Double conductance peak away from zero (left plot) for a setup in which the potential barrier lies inside the gapped region (see LDoS right plot) and the distance between the Majorana states is short enough to allow for considerable hybridization.

be broadened either by a finite temperature or by hybridization between the Majorana fermions, which corresponds to a greater overlap between the Majorana states and hence a finite lifetime. We can observe the later effect when we decrease the gap width from figure 7.3 to only about 30 sites and choose fitting geometrical parameters to again see a peak in figure 7.7. The hybridization moves the Majorana modes away from zero energy by about $6 * 10^{-6}t$, so it is still small, but enough to give the peak a structure when zoomed in to a bias voltage of order $10^{-8}t$ (left side of figure 7.7). As can be seen, the broadening from this effect is rather small. The experimental papers claim their peak shapes to be consistent with the expected temperature broadening (see in particular [Das et al., 2012] figure 6b and discussion as well as [Mourik et al., 2012] figure 3D), so that seems to be the important effect here. As was mentioned in the derivation of our Green's function in chapter 5, we have made a zero-temperature assumption when treating the p-wave superconductor term in (5.4), but for small temperatures it should still be a reasonable approximation. When we turn on a finite temperature, the zero-bias peak does indeed broaden significantly in our model, as can be seen in figure 7.8 with $T = 30mK$ as in [Das et al., 2012].

The model we have developed so far is not limited to describing this particular setup which shows MFs. Another idea that was tried is to connect the second lead not on the right end of the central region, but to let the barrier and gapped region overlap and connect it weakly to the site in which the Majorana fermion is localized. In this case the zero-bias peak will appear as well. A drawback of such setups with the second lead connected not on the border is the "free hanging" sites in the central region, a finite chain only connected at one side. States can enter this region and reflect back, obscuring the results with their superposition which gets even more complicated by a strong odd-even effect that appears - the conductance changes heavily depending on an odd

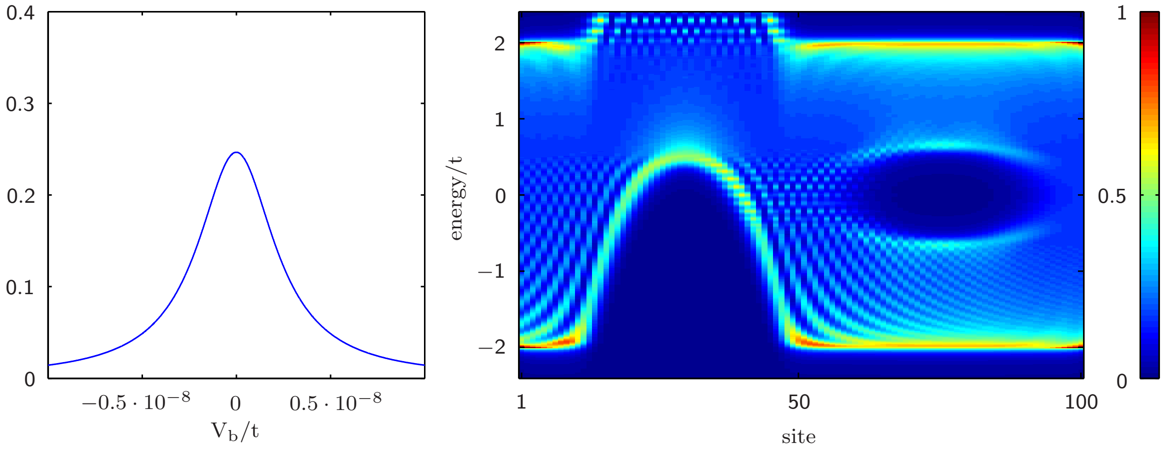

Figure 7.7: The zoomed in conductance peak (left side) of a system with a very short superconducting region (right side) to allow for hybridization between the Majorana modes. Note that the central region size is reduced to $N = 100$ compared to $N = 200$ in figure 7.3. Parameters: gap width 30 sites, gap height $\Delta = 0.6$, barrier height $f = 2.45$, barrier width 20 sites.

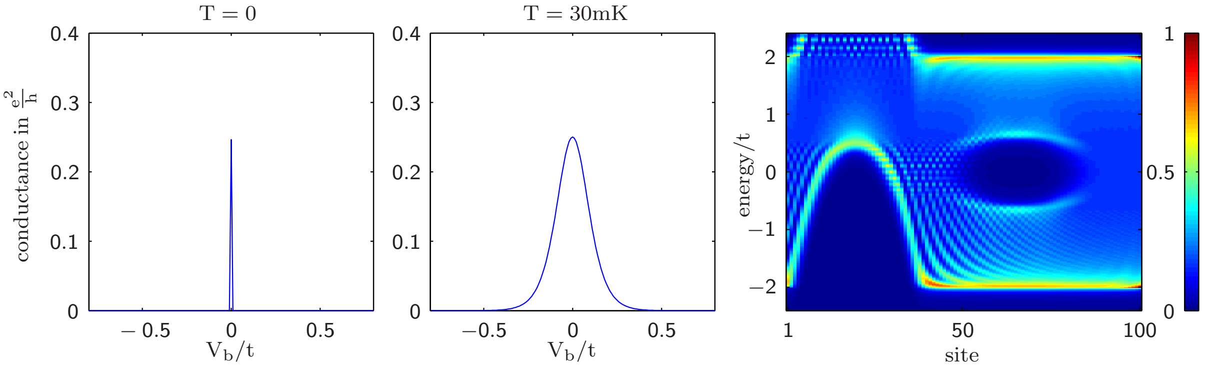

Figure 7.8: Comparison of the zero-bias peak of a system at $T = 0$ with only broadening from hybridization (left plot) with the same system at $T = 30mK$ (middle plot). For orientation, the LDoS is plotted on the right plot. Central region $N = 100$ sites, gap width 30 sites, gap height $\Delta = 0.6$, barrier height $f = 2.45$, barrier width 20 sites

or even number of sites in said “free hanging” region.

7.3 Conclusion and Outlook

We have begun by reviewing a tight binding model that allows for a system with explicit geometry in form of quantum point contacts, first for spinless systems (chapter 2) and then temporarily extended to spin-full systems in chapter 3. Besides the review of known results, we have in particular included higher-order terms of the spin-orbit interaction in this thesis in section 3.6 and examined how and why their effect is negligible compared to the lowest order terms that are usually considered.

The idea of Majorana fermions and the Kitaev model (chapter 4) as well as their special non-Abelian exchange behavior (section 6.3) was reviewed. We introduced our ansatz of a p-wave superconducting region to our model, giving us an extended Kitaev model which allows for explicit geometric structures. To gain the Green’s functions and ultimately the differential conductance through such a system, the Keldysh formalism was employed in chapter 5. Transitions between a p-wave superconductor in topological phase and a normal conductor lead to the zero-energy modes expected from the Kitaev model (compare figure 6.1 with no normal conducting leads and figure 6.4 with leads), but we observe that these zero-energy modes must be localized to contribute to the conductance in form of a zero-bias peak (compare figure 6.5 and 7.3). In particular in a setup that follows the experiments with a QPC next to the superconducting region, we get a conductance that shows the features of the experiments: a wide conductance valley with a single peak at zero-bias (compare experiment figure 7.1 and our model figure 7.3). Unlike the temperature broadened peak in the experimental data, the zero-bias peak from our model has a width of exactly one data-point, since we consider the zero temperature case and the only other effect that could widen this peak is the hybridization of the two localized zero-energy states, which turns out to be very small and comparable to the calculation precision unless the width of the gapped region is chosen to be very short (figure 7.7). But we can use our model at least as an approximation for low temperatures and then indeed see a broadening similar to the experimental data in figure 7.8.

Unexpectedly, we observed that the height of this peak strongly depends on the geometry of the QPC in the following way. For a chosen width and height of the QPC barrier, the size of the superconducting gap in form of its width and height has to be tuned accordingly (or the other way around) to get a peak of the full height of $0.25\frac{e^2}{h}$. Generally, a bigger QPC barrier requires a bigger gapped region for the system to develop the conductance peak (see table in section 7.2) and away from those optimal parameters the conductance quickly drops.

Just like the experimental results, our model also requires careful fine tuning for the zero-bias peak to appear. Although we do not understand the unexpectedly strong geometry dependence of the zero-bias peak, its appearance in our geometry including Kitaev model of the experimental setup is consistent with MFs being a correct interpretation of the experimental results.

The obvious next step for future calculations is to combine our considerations in chapter 3 with our following calculations in chapter 5. The former of those introduced wires with a spin degree of freedom while the later told us how to deal with a Hamiltonian containing superconducting terms.

Together that allows us to make sense of an s-wave superconducting term

$$H_{\text{s-wave SC}} = \sum_j \left(\Delta c_{j\uparrow} c_{j\downarrow} + \Delta^* c^\dagger_{j\uparrow} c^\dagger_{j\downarrow} \right) \tag{7.1}$$

which creates and destroys cooper pairs of electrons on the same site. So far we have only been able to explicitly consider a p-wave superconducting term, since two electrons on the same site were forbidden by Pauli exclusion principle.

Instead of arguing that an experimental setup following the outline in 4.2 should effectively behave according to the Kitaev model, we could instead explicitly model the kind of wire that was used in experiments (section 7.1) including the spin-orbit effects and external magnetic fields. This would mean retracing the Green's function and conductance formula calculation in chapter 5 with explicit spin indices, making sure that all the steps are still valid. In the end we would gain a new matrix we have to invert in formula (5.16) and (5.17). On top of that, we have so far always used the rather crude approximation of independent electrons. Works on QPC indicate that the interactions seem to have a big influence on the conductance shape (for example [Bauer et al., 2013]), so including them into our model would be a natural extension. The basic idea for interactions would be to use a method like functional renormalization group to capture their effect in an additional self-energy matrix that has to be included when calculating the Green's function.

All together, this would allow us to have a better understanding of and allow better predictions about the fine tuning that was necessary in the experiments to get into a topological superconductor phase containing Majorana fermions. It might then even be possible to compare the differential conductance results not only qualitatively as we did in the previous section 7.2 but even quantitatively.

List of Figures

Bibliography

[Alicea, 2010] Alicea, J. (2010). Majorana fermions in a tunable semiconductor device. *Physical Review B.*

[Alicea, 2012] Alicea, J. (2012). New directions in the pursuit of majorana fermions in solid state systems. *Rep. Prog. Phys.*

[Alicea et al., 2010] Alicea, J., Oreg, Y., Refael, G., von Oppen, F., and Fisher, M. P. A. (2010). Non-abelian statistics and topological quantum information processing in 1d wire networks. *nature physics.*

[Altland and Simons, 2010] Altland, A. and Simons, B. (2010). *Condensed Matter Field Theory - Second Edition.* Cambridge University Press.

[Bauer, 2008] Bauer, F. (2008). *0.7 Anomaly of Quantum Point Contacts - Treatment of Interaction with functional Renormalization Group.* PhD thesis, Ludwig Maximilians University.

[Bauer et al., 2013] Bauer, F., Heyder, J., Schubert, E., Borowsky, D., Taubert, D., Bruognolo, B., Schuh, D., Wegscheider, W., von Delft, J., and Ludwig, S. (2013). Microscopic origin of the 0.7-anomaly in quantum point contacts. *nature.*

[Beenakker, 2012] Beenakker, C. W. J. (2012). Search for majorana fermions in superconductors. *Annual Review of Condensed Matter Physics.*

[Birkholz, 2008] Birkholz, J. (2008). *Spin-orbit interaction in quantum dots and quantum wires of correlated electrons - A way to spintronics?* PhD thesis, Georg-August-Universität zu Göttingen.

[Bychkov and Rashba, 1984] Bychkov, Y. and Rashba, E. (1984). Oscillatory effects and the magnetic susceptibility of carriers in inversion layers. *Journal of Physics C: Solid State Physics.*

[Büttiker, 1990] Büttiker, M. (1990). Quantized transmission of a saddle-point constriction. *Physical Review B.*

[Cowan et al., 1956] Cowan, C., Reines, F., Harrison, F., Kruse, H., and McGuire, A. (1956). Detection of the free neutrino: a confirmation. *A. Science.*

[Das et al., 2012] Das, A., Ronen, Y., Most, Y., Oreg, Y., Heiblum, M., and Shtrikman, H. (2012). Zero-bias peaks and splitting in an al–inas nanowire topological superconductor as a signature of majorana fermions. *nature physics*.

[Datta, 1995] Datta, S. (1995). *Electronic Transport in Mesoscopic Systems*. Cambridge University Press.

[Deng et al., 2012] Deng, M., Yu, C. L., Huang, G. Y., Larsson, M., Caroff, P., and Xu, H. (2012). Anomalous zero-bias conductance peak in a nb−insb nanowire−nb hybrid device. *Nano Letters*.

[Dirac, 1928] Dirac, P. A. M. (1928). The quantum theory of the electron. *Proceedings of the Royal Society A: Mathematical, Physical and Engineering Sciences*.

[Dresselhaus, 1955] Dresselhaus, G. (1955). Spin-orbit coupling effects in zinc blende structures. *Physical Review*.

[Egger and Flensberg, 2012] Egger, R. and Flensberg, K. (2012). Emerging dirac and majorana fermions for carbon nanotubes with proximity-induced pairing and spiral magnetic field. *Physical Review B*.

[Eliezer and Semenoff, 1992] Eliezer, D. and Semenoff, G. W. (1992). Intersections forms and the geometry of lattice chern-simons theory. *Phys. Lett. B*.

[Fu and Kane, 2008] Fu, L. and Kane, C. L. (2008). Superconducting proximity effect and majorana fermions on the surface of a topological insulator. *Physical Review Letters*.

[Fu and Kane, 2009] Fu, L. and Kane, C. L. (2009). Josephson current and noise at a superconductor/quantum-spin-hall-insulator/superconductor junction. *Physical Review B*.

[Goulko et al., 2014] Goulko, O., Bauer, F., Heyder, J., and von Delft, J. (2014). The effect of spin-orbit interactions on the 0.7-anomaly in quantum point contacts. *arXiv:1408.0746 [cond-mat.mes-hall]*.

[Hassler et al., 2010] Hassler, F., Akhmerov, A. R., Hou, C.-Y., and Beenakker, C. W. J. (2010). Anyonic interferometry without anyons: how a flux qubit can read out a topological qubit. *New Journal of Pysics*.

[Ivanov, 2001] Ivanov, D. A. (2001). Non-abelian statistics of half-quantum vortices in p-wave superconductors. *Physical Review Letters*.

[Jakobs, 2009] Jakobs, S. (2009). *Functional renormalization group studies of quantum transport through mesoscopic systems*. PhD thesis, RWTH Aachen.

[Kamenev, 2001] Kamenev, A. (2001). *Field Theory of Non-Equilibrium Systems*. Cambridge University Press.

[Karrasch, 2006] Karrasch, C. (2006). Transport through correlated quantum dots - a functional renormalization group approach.

[Keldysh, 1965] Keldysh, L. V. (1965). Diagram technique for nonequilibrium processes. *Soviet Physics JETP.*

[Kitaev, 2000] Kitaev, A. Y. (2000). Unpaired majorana fermions in quantum wires. *Physics-Uspekhi.*

[Larkin and Ovchinnikov, 1977] Larkin, A. I. and Ovchinnikov, Y. N. (1977). Nonlinear effects during the motion of vortices in superconductors. *Soviet Physics JETP.*

[Leijnse and Flensberg, 2011] Leijnse, M. and Flensberg, K. (2011). Quantum information transfer between topological and spin qubit systems. *Physical Review Letters.*

[Leijnse and Flensberg, 2012] Leijnse, M. and Flensberg, K. (2012). Introduction to topological superconductivity and majorana fermions.

[Lutchyn et al.,] Lutchyn, R. M., Sau, J. D., and Sarma, S. D. Majorana fermions and a topological phase transition in semiconductor-superconductor heterostructures.

[Majorana, 1937] Majorana, E. (1937). Teoria simmetrica dell'elettrone e del positrone.

[Meir et al., 2002] Meir, Y., Hirose, K., and Wingreen, N. S. (2002). Kondo model for the 0.7 anomaly in transport through a quantum point contact. *Phys. Rev. Lett.*

[Meir and Wingreen, 1992] Meir, Y. and Wingreen, N. S. (1992). Landauer formula for the current through an interacting electron region.

[Mourik et al., 2012] Mourik, V., Zuo, K., Frolov, S. M., Plissard, S. R., Bakkers, E. P. A. M., and Kouwenhoven, L. P. (2012). Signatures of majorana fermions in hybrid superconductor-semiconductor nanowire devices. *Science.*

[Nayak et al., 2008] Nayak, C., Simon, S. H., Stern, A., Freedman, M., and Sarma, S. D. (2008). Non-abelian anyons and topological quantum computation. *Rev. Mod. Phys.*

[Negele and Orland, 1988] Negele, J. W. and Orland, H. (1988). *Quantum Many-Particle Systems.* Westview Press.

[Oreg et al., 2010] Oreg, Y., Rafael, G., and von Oppen, F. (2010). Helical liquids and majorana bound states in quantum wires. *Physical Review Letters.*

[Reilly et al., 2002] Reilly, D. J., Buehler, T. M., O'Brien, J. L., Hamilton, A. R., Dzurak, A. S., Clark, R. G., Kane, B. E., Pfeiffer, L. N., and West, K. W. (2002). Density-dependent spin polarization in ultra-low-disorder quantum wires. *Physical Review Letters.*

[Rickayzen, 1980] Rickayzen, G. (1980). *Green's Functions and Condensed Matter*. Academic Press.

[Rokhinson et al., 2012] Rokhinson, L. P., Liu, X., and Furdyna, J. K. (2012). Observation of the fractional a.c. josephson effect and the signature of majorana particles. *nature physics*.

[Sarma et al., 2006] Sarma, S. D., Nayak, C., and Tewari, S. (2006). Proposal to stabilize and detect half-quantum vortices in strontium ruthenate thin films: Non-abelian braiding statistics of vortices in a px+ipy superconductor. *Physial Review B*.

[Sau et al., 2010] Sau, J., Lutchyn, R. M., Tewarl, S., and Sarma, S. D. (2010). Generic new platform for topological quantum computation using semiconductor heterostructures. *Physical Review Letters*.

[Sau and Sarma, 2012] Sau, J. D. and Sarma, S. D. (2012). Realizing a robust practical majorana chain in a quantum-dot-superconductor linear array. *Nature communications*.

[Semenoff, 1988] Semenoff, G. W. (1988). Canonical quantum field theory with exotic states. *Physical Review Letters*.

[Tewari et al., 2007] Tewari, S., Sarma, S. D., Nayak, C., Zhang, C., and Zoller, P. (2007). Quantum computation using vortices and majorana zero modes of a $p_x + ip_y$ superfluid of fermionic cold atoms. *Physical Review Letters*.

[van Wees et al., 1988] van Wees, B. J., van Houten, H., Beenakker, C. W. J., Williamson, J. G., Kouwenhoven, L. P., van der Marel, D., and Foxon, C. T. (1988). Quantized conductance of point contacts in a two-dimensional electron gas. *Physical Review Letters*.

[Weinberg, 2000] Weinberg, S. (2000). *The Quantum Theory of Fields III Supersymmetry*. Cambridge University Press.

[Wilczek, 2009] Wilczek, F. (2009). Majorana returns. *Nature Physics*.

[Williams et al., 2012] Williams, J. R., Bestwick, A. J., Gallagher, P., Hong, S. S., Cui, Y., Bleich, A. S., Analytis, J. G., Fisher, I. R., and Goldhaber-Gordon, D. (2012). Unconventional josephson effect in hybrid superconductor-topological insulator devices. *Physical Review Letters*.

[Winkler, 2003] Winkler, R. (2003). *Spin-Orbit Coupling Effects in Two-Dimensional Electron and Hole Systems*. Springer.

Acknowledgements

First of all, I want to thank Jan von Delft for finding this very interesting and rich topic and giving me the opportunity to write this thesis in his group. I learned a lot during my year here and had an overall great experience and as much support as i could hope for.

I especially want to thank Dennis Schimmel for our countless hours of fruitful discussions of various details of superconductors, Majorana fermions, the interpretation of my results and lots of other physics. His immense (and very quantum-field-theoretical) knowledge about every topic i possibly had questions about and the patience in his explanations was a fantastic help during this year.

Further thanks goes to Florian Bauer and Jan Heyder, which were a great help in the initial familiarization with the description of quantum point contacts and are both exceptional and enthusiastic teachers of physics.

The other master students Lukas Weidinger, Nils-Oliver Linden, Dimitri "Dimer" Pimenov as well as Johannes Hausschild all helped me with various discussions over the year and I thank them, also for our countless fun conversations over lunch and for making it a pleasure to spend time in the office.

Last but not least, i want to thank my family for their support and for making it possible for me to follow this study.

Statement of Authorship

Herewith, I certify that this thesis has been composed by myself and describes my own work unless otherwise acknowledged in the text. I created all figures on my own unless explicitly stated otherwise. Parts that are direct quotes or paraphrases are identified as such.

Munich, November 19, 2014 in Munich

(Kevin Jägering)